Dynamic Reconstruction and Multivariable Control for Force-Actuated, Thin Facesheet Adaptive Optics

Simon C. O. Grocott and David W. Miller

May 1997 SERC#3-97

(Under the sponsorship of NASA)

This report is based on the unaltered thesis of Simon C. O. Grocott submitted to the Department of Aeronautics and Astronautics in partial fulfillment of the requirements for the degree of Doctor of Philosophy at the Massachusetts Institute of Technology.

Abstract

The Multiple Mirror Telescope (MMT) under development at the University of Arizona takes a new approach in adaptive optics placing a large (0.65 m) force-actuated, thin facesheet deformable mirror at the secondary of an astronomical telescope, thus reducing the effects of emissivity which are important in IR astronomy. However, The large size of the mirror and low stiffness actuators used drive the natural frequencies of the mirror down into the bandwidth of the atmospheric distortion.

Conventional adaptive optics takes a quasi-static approach to controlling the deformable mirror. However, flexibility within the control bandwidth calls for a new approach to adaptive optics. Dynamic influence functions are used to characterize the influence of each actuator on the surface of the deformable mirror. A linearized model of atmospheric distortion is combined with dynamic influence functions to produce a dynamic reconstructor. This dynamic reconstructor is recognized as an optimal control problem.

Solving the optimal control problem for a system with hundreds of actuators and sensors is formidable. Exploiting the circularly symmetric geometry of the mirror, and a suitable model of atmospheric distortion, the control problem is divided into a number of smaller decoupled control problems using circulant matrix theory .

A hierarchic control scheme which seeks to emulate the quasi-static control approach that is generally used in adaptive optics is compared to the proposed dynamic reconstruction technique. Although dynamic reconstruction requires somewhat more computational power to implement, it achieves better performance with less power usage, and is less sensitive than the hierarchic technique.

Acknowledgments

This work was supported by NASA Marshall Space Flight Center Grant No. NAG8-1291 with James Bilbrow as the technical monitor and Sharon-Leah Brown as the MIT contract administrator; and by NASA Langley Research Center Grant No. NAG1-1717 with Keith W. Belvin as technical monitor and Sharon-Leah Brown as the MIT contract administrator.

In addition, supporting work was supported by the NASA In-Step and CSI Offices, with Mr. Gregory Stover and Dr. Jerry Newsom as contract monitors, under contract NAS1-19622.

Contents

List of Figures

List of Tables

Chapter 1

Introduction

1.1 Motivation

Traditionally, adaptive optics systems use a small thin deformable mirror with piezoelectric or magnetostrictive actuators located at a tertiary or quaternary location in the optical train to compensate for atmospheric distortion. The Multiple Mirror Telescope (MMT) under development at the University of Arizona is taking a new approach to atmospheric compensation. To minimize emissivity effects for infrared astronomy the new approach seeks to place the deformable element at the secondary location in the optical train.

The MMT is shown schematically in Figure 1-1, taken from Ref. [1]. A 4W laser tuned to resonate with the sodium layer in the atmosphere is used to produce an artificial guide star high in the atmosphere. The light from this guide star is used to measure the wavefront distortion caused by turbulence in the atmosphere. Incoming light from both the artificial guide star and from science objects enters the aperture of the telescope, and is reflected from the 6.5 m primary mirror. It is then reflected from an adaptive secondary mirror and focused on the detectors. Just prior to the detector is a dichroic beamsplitter which sends light from the artificial guide star which is in the visible range to a wavefront sensor while the science light in the infrared passes through to the detectors. The wavefront sensor measures the slope of the wavefront across a number of smaller subapertures. The wavefront computer

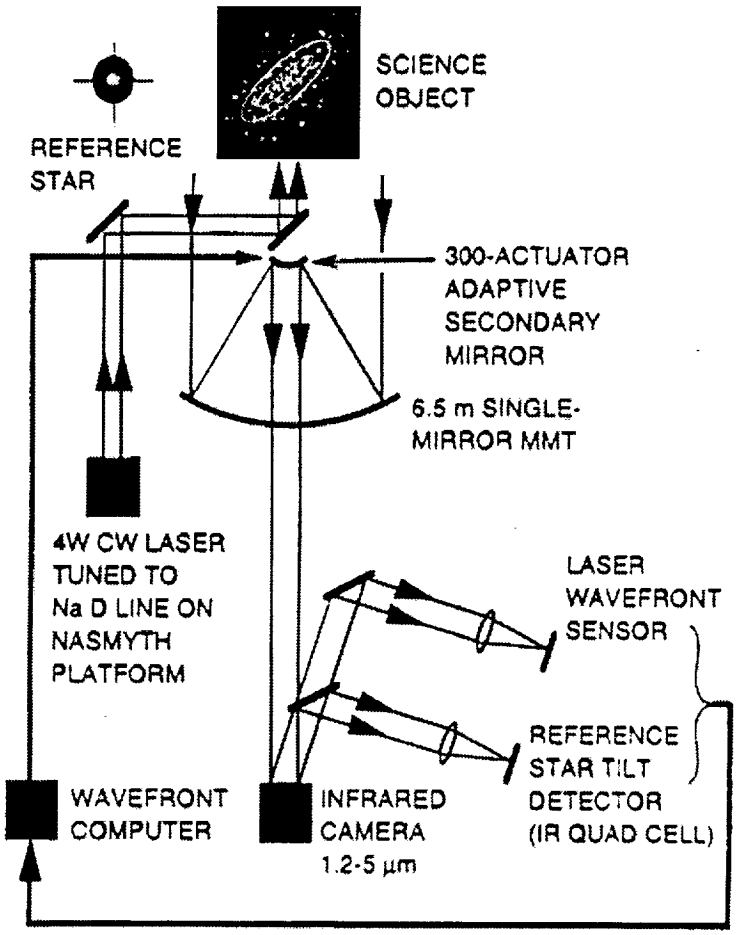

Figure 1-1: Schematic diagram of the Multiple Mirror Telescope (MMT).

calculates commands to send to actuators on the adaptive secondary mirror. These actuators then reshape the mirror so as to cancel measured wavefront error.

This new approach has clear benefits in terms of the signal to noise ratio obtained when light is bounced from fewer emitting surfaces. However, it poses some technical challenges as well. Where deformable mirrors are usually small and actuated by stiff piezoelectric or magnetostrictive actuators, the proposed deformable mirror is necessarily large. The 6.5 m primary mirror for the MMT requires a 0.65 m secondary. Furthermore, the correction of global tilt at the secondary mirror requires relatively large displacements of the mirror. Electro-magnetic voice coil actuators are planned to provide the actuation necessary to deform the mirror. The combination of large mirror size and low stiffness force actuation result in a considerably more flexible mirror than

usual. This extra flexibility results in a large number of flexible vibrational modes of the mirror within the bandwidth necessary to correct for atmospheric distortion across the large 6.5 m aperture. It is the need to control these dynamic modes that motivates the work in this thesis.

1.2 Previous Work

Many approaches to controlling adaptive optics have been taken. This section outlines three basic approaches which specifically address different issues of the problem. In all three cases, the control contains a reconstructor which provides estimates of the wavefront displacement. The objective of the control is then to have the mirror track the estimated wavefront displacement, thus cancelling the wavefront error in the system.

1.2.1 Classical Control with a Reconstructor

The standard approach for controlling the mirror is to assume that the problem is quasi-static. Wavefront sensors are measured. The measurements pass to a reconstructor (any of the reconstructors from Chapter 2). The reconstructor outputs position commands for the actuators on the mirror. The commanded positions minimize an estimate of the wavefront displacement error. Following the reconstructor is a classical PID control loop, often solely integral feedback [2]. This classical control loop acts to servo the actuators so that the mirror follows the commanded positions that are output from the reconstructor.

Figure 1-2 shows a block diagram representation for this control system. The difference between the distorted atmosphere, y_w, and the distorted mirror, y_m, surface is measured by the wavefront sensor, y_{wf}. The reconstructor, R, reconstructs the atmospheric distortion from these measurements, and determines the mirror position commands y_c which best counteract the distortion. The controller K then creates control commands u which servo the system G so that the mirror position y_m tracks y_c. The system G is assumed to be quasi-static, modelling only the time delay associated

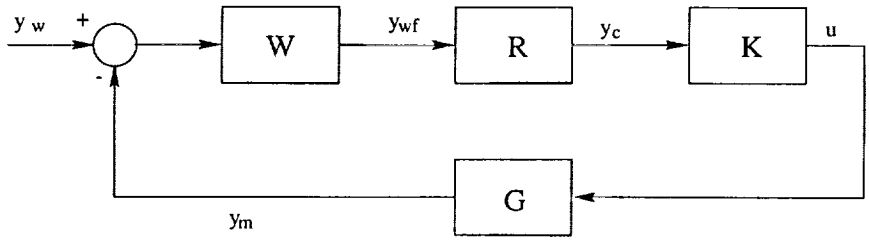

Figure 1-2: Block diagram for standard control approach.

with the measurement rate and the DC gain of the actuators [3]. The controller K is usually diagonal consisting of identical components. That is, one SISO PID controller is designed and it is implemented in all the servo loops.

The benefits of this type of control are that it breaks the problem into two complementary parts. The reconstructor provides an estimate of the wavefront and commands to conjugate it, and the servo control follows the commands. This can be a very effective control when the dynamics of the mirror can be ignored. This usually happens when high impedance actuators, such as piezoelectric stacks or magnetostrictives, are used. The high impedance of the actuator raises the natural frequencies of the deformable mirror so that the problem is quasi-static in the frequency range of interest. Because reconstruction is handled independently, this approach also allows more sophisticated reconstruction schemes [4, 5, 6].

A similar tack is taken by Gully *et al.* [7] who use integral feedback, but use an Extended Kalman Filter (EKF) [8, 9] to estimate errors in the registration of the wavefront matrix. That is, misalignment of the subapertures of a Shack-Hartmann wavefront sensor which cause errors in the Reconstructor are adaptively corrected. This again is an approach that allows for more sophistication in the Reconstructor, but ignores flexible dynamics.

When low impedance force actuators, rather than high impedance position actuators, are used the natural frequencies of the deformable mirror drop significantly and a quasi-static model of the dynamics can be insufficient.

1.2.2 Modern Control with a Reconstructor

Again using high impedance position actuators, Huang *et al.* [3] use modern multivariable control techniques to address the high degree of coupling in multi-actuator adaptive optics systems. In their approach, the dynamics of the deformable mirror and wavefront sensors are modelled as constant gains with time delays associated with the latency in measurements. A Reconstructor is incorporated in the feedback loop as in Figure 1-2. However, the compensator K is designed using $\mathcal{H}_\infty$ control techniques and permits feedback between all actuators and sensors unlike the previous approach.

Essentially this control is similar to Gully *et al.* [7], in that it addresses the coupling of actuators and sensors. Rather than estimating the coupling through the Reconstructor matrix online as in Gully *et al.* [7], Huang *et al.* [3] create a measurement model with an existing Reconstructor that incorporates all the coupling amongst actuators and wavefront sensors. They then design diagonal PID controllers and fully coupled $\mathcal{H}_\infty$ controllers to provide good multivariable tracking.

This approach is a step beyond simply using PID control, as the authors show. However, once again the models used assume that the flexible dynamics of the mirror are insignificant in the frequency range of interest to their problem. The flexible dynamics are important in our problem.

1.2.3 Current Force-Actuated Control Scheme

The current control approach planned for use in the MMT seeks to have as much commonality with the standard quasi-static integral control approach of Section 1.2.1 as possible. Biasi and Gallieni [10] propose a multi-rate control system with an inner control loop operating at a sample rate ten times faster than the outer reconstructor loop. The inner loop uses a set of gap sensors which measure the displacement of the deformable mirror relative to the backplate at each of the actuator locations.

A block diagram showing the elements of this control approach is shown in Figure 1-3. The outer loop consists of the Reconstructor and integral control exactly as would be designed for the quasi-static system in Section 1.2.1.

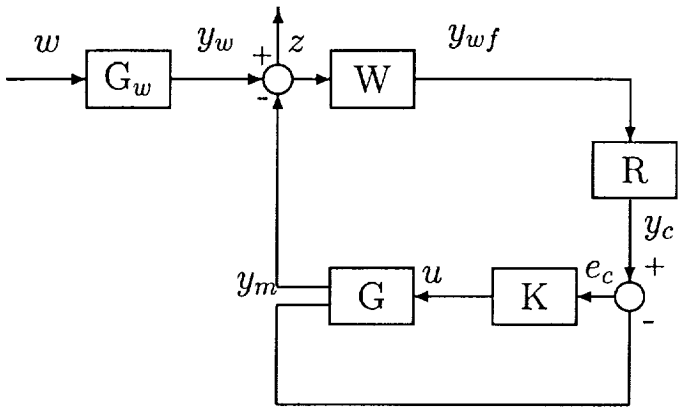

Figure 1-3: Block diagram for hierarchic control approach.

The inner control loop seeks to servo the deformable mirror so that it follows the commands generated by the outer loop integral control. The model used to design the control consists of a single resonant second order pole. The approach taken by Biasi and Gallieni is to select a set of PID control gains using this single mode model that positions the closed loop poles as those of a Bessel filter [11]. The Bessel filter acts as a constant time delay within its bandwidth, and thus the hope is to assign the closed loop poles so that the closed inner loop servo controller acts as a pure delay within the bandwidth that is required for the integral control.

The SISO controller that is designed using this approach is then repeated for each of the collocated actuator and gap sensor pairs on the mirror. There are several problems that can result from this. The first problem is ignoring all of the high frequency dynamics. Using a single mode model is inappropriate for a system that has over 20 modes up to 1 kHz as can be seen in Table 4.3. The second problem is that simply repeatedly applying a SISO controller, even a well designed SISO controller, to a large number of highly coupled input and output pairs can easily destabilize the system. It would take a considerable number of iterations on the SISO single mode design to find appropriate PID gains that would stabilize the mirror when applied at multiple input output pairs. The third problem is that identical SISO controllers are

unable to balance the singular values of the system leading to a wide range of control effectiveness on various modes. Some "directions" of input will be tracked well, while others will not. This need to balance the tracking singular values was what led Huang *et al.* [3] to use a multivariable control technique for even the quasi-static dynamic system. Finally, significant interaction can occur between inner and outer control loops unless the inner loop has a very high bandwidth. Limits on the bandwidth of the inner loop arise because of phase lag and the high modal density of the system. In Section 5.2.2 these potential problems are shown in more detail.

1.3 Thesis Statement

The objective of this thesis is to develop a control approach for adaptive optics that takes account of structural flexibility and its effect on wavefront measurement and is practical to solve and to implement in real time. The proposed approach differs from this previous work in adaptive optics in that it directly incorporates a dynamic model of both atmospheric distortion and the structural dynamics of the deformable mirror into a control design model to yield global multivariable controllers. The global control can be viewed as an extension of the reconstruction process used in this previous work from a quasi-static to a dynamic framework. Hence, the approach is termed dynamic reconstruction.

1.4 Thesis Outline

Chapter 2 provides an overview of the process by which wavefront measurements are converted to commands to the adaptive secondary mirror. This process is known as Reconstruction because in the process, an estimate of the wavefront is reconstructed from a series of sensor measurements. The process of measuring the wavefront distortion is discussed first. This is followed by the process of estimating the wavefront from these measurements. The final step in the process is determining the commands that must be sent to the actuators in order to correct for the wavefront distortion.

When the deformable mirror used to correct the wavefront distortion is very flexible, having dynamics within the bandwidth that is required for control, these standard reconstruction approaches are very limited. The concept of a dynamic reconstructor is introduced as a reconstructor that takes into account dynamics of both the atmosphere and the deformable mirror, and produces optimal control signals for wavefront conjugation.

Chapter 3 introduces the concept of circulant matrices and systems. These are systems which exhibit a degree of circular symmetry that allows them to be divided into a number of smaller independent systems. There are particular benefits for control systems that can be split into smaller problems. The smaller problems are faster to solve and implement, and better conditioned. The process of modelling systems that are circulant follows.

Chapter 4 discusses the specific details of modelling the system required to design control for the adaptive secondary mirror. A finite element model of the mirror itself is presented. The section on structural modelling is followed by a detailed look at how to model the various actuators and sensors that are used for controlling the mirror. This includes a discussion of the modelling of temporally averaged sensors. Finally, a model of expected atmospheric distortion is presented. The combination of these processes comprises the system modelling.

Chapter 5 begins with a discussion of several possible new adaptive optics control approaches which use two different kinds of control architecture. A small sample problem is presented by which the new dynamic reconstruction process is compared with competing approaches. The chapter ends with the presentation of simulations of the dynamic reconstruction process on the full scale model of the adaptive secondary that was produced in Chapter 4.

Finally, Chapter 6 presents a summary of the thesis followed by a listing of the contributions of this thesis and recommendations for researchers who will carry on this work.

Chapter 2

Reconstruction

Control of adaptive optics systems generally breaks into two parts which are related to the actuation and the sensing of incoming wavefronts. The first step is to reconstruct a distorted wavefront from measurements of incoming light. The second step is to have a deformable mirror mimic the shape of the distorted wavefront so that the distortion in the wavefront, after it is reflected from the deformable mirror, has been reduced.

Figure 2-1 shows the process known as phase conjugation by which wavefront aberrations are corrected. In Figure 2-1(a), an aberrated wavefront, shown here simply as a pulse discontinuity, approaches the deformable mirror. The necessary conjugation shape has been determined and the mirror has adjusted. In Figure 2-1(b), the wavefront first contacts the surface of the mirror and is reflected. The main bulk of the wavefront has hit the mirror, but the aberrated section, which is delayed, has not yet contacted the mirror surface. Just as the reflected wavefront reaches the delayed portion of the wavefront, the delayed wavefront is reflected from the deformed mirror. This is shown in Figure 2-1(c). This reflection of the aberrated portion of the wavefront occurs just at the right time for the delayed wavefront to rejoin the remainder of the wavefront, and in Figure 2-1(d) the corrected wavefront travels away from the deformable mirror towards the focal plane for imaging. Note that because of the reflection, the wavefront travels twice over the path shown. To correct wavefront aberrations, therefore, the deformable mirror needs only to deform

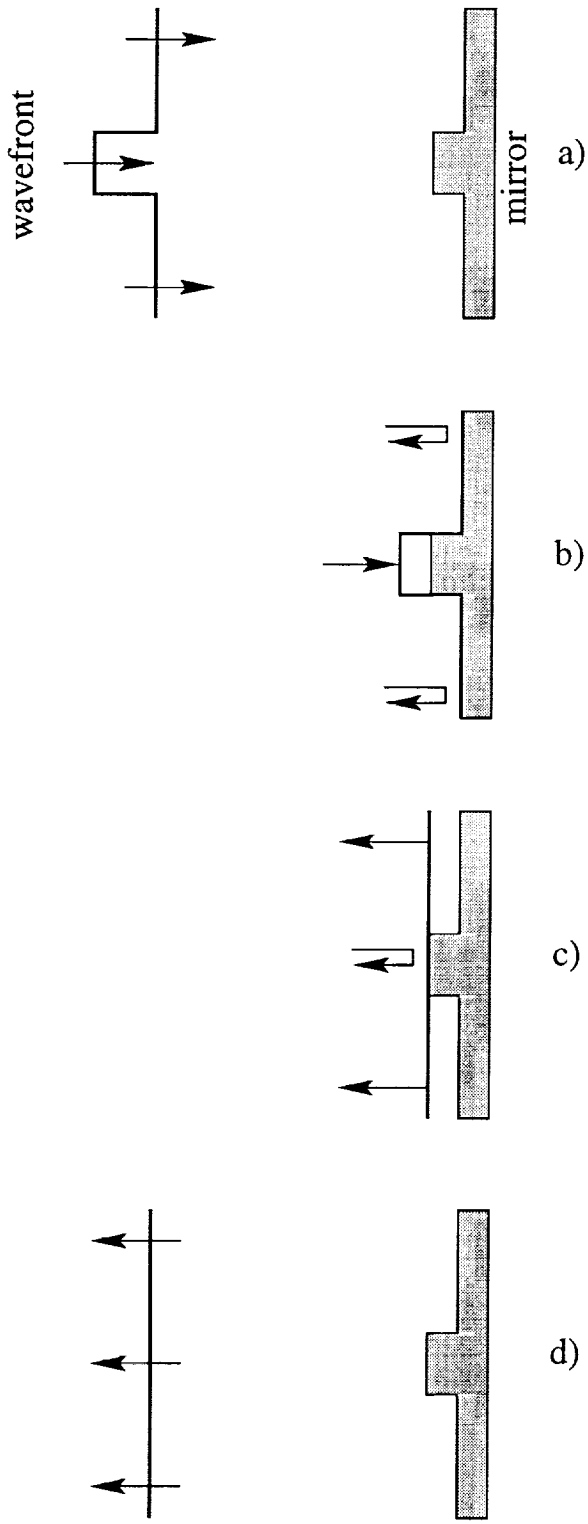

Figure 2-1: The process of wavefront conjugation.

by half the magnitude of the aberration. This illustrates the process by which the deformable mirror corrects for wavefront aberration. However, the aberration is not constant with time. The aberrations change significantly with time as discussed in Section 4.2. This changing aberration requires the shape of the MMT mirror to change with a bandwidth on the order of 100 Hz.

2.1 Measuring the Wavefront

In order to correct for any distortion in an incoming wavefront, first the distortion must be measured. There are many different ways to measure an incoming wavefront [12]. The information that is most often provided by wavefront sensors is the slope of the wavefront [13] at a location on the mirror, or more precisely the average slope across an area called the subaperture. In this thesis we concentrate on a wavefront sensor known as a Shack-Hartmann sensor [12] which is to be used on the MMT [1].

A Shack-Hartmann sensor is shown in Figure 2-2. The sensor consists of an array of small lenses known as a lenslet array. The lenslet array divides the aperture of the telescope into a number of smaller subapertures. The light gathered by each of these subapertures strikes the appropriate lens in the lenslet array and is focused onto a detector. The detector is a quadcell, a 2×2 pixel grid, of a CCD camera. Figure 2-3 shows the image of the subaperture formed on the quadcell. Clearly no image can be resolved from such a coarse detector. All that is required is to measure the centroid of the beam relative to the center of the quadcell. The centroid is calculated through a weighted average of the intensities measured in each of the four pixels. The location of the centroid is proportional to the average slope of the wavefront in the subaperture. The centroid is found in two dimensions, labeled x and y. Thus, each lenslet provides wavefront slope measurements for a given subaperture in two directions.

Clearly then, the number of lenslets determines the spatial resolution to which an incoming wavefront can be measured. From the slope measurements of the wave-

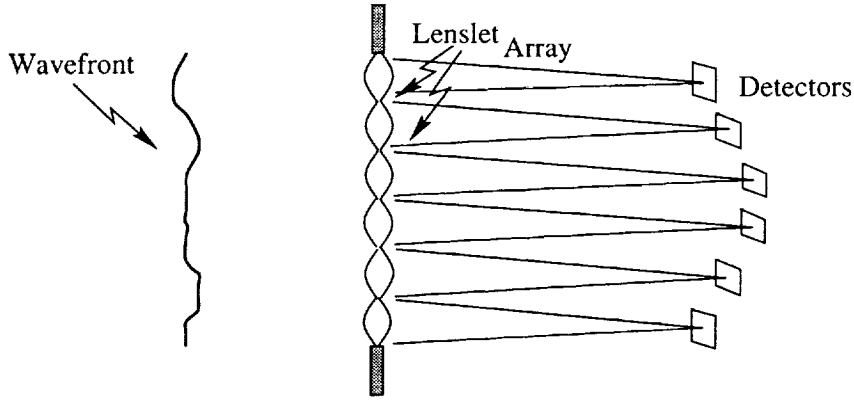

Figure 2-2: Shack-Hartmann sensor.

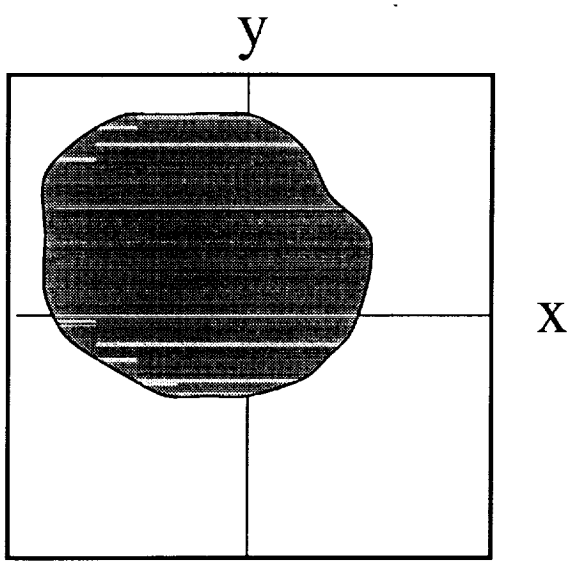

Figure 2-3: Quad-cell array.

front sensor, a picture of the wavefront can be constructed. Such a process is called reconstruction.

2.2 Reconstructing the Wavefront

Many simple reconstruction problems consider a square grid of points at which the phase of the wavefront, or the difference in displacement between an aberrated and unaberrated wavefront normalized by the wavelength of the light, is to be estimated. Aligned with the grid points are subapertures for wavefront sensor measurements.

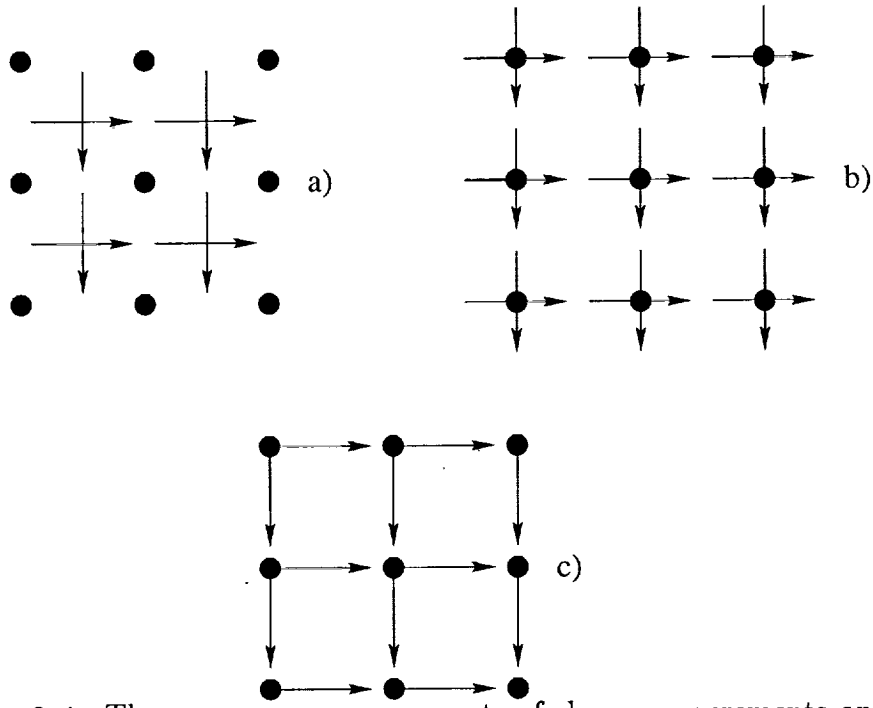

Figure 2-4: Three common arrangements of slope measurements and wavefront phase evaluation points. The points represent locations at which the wavefront phase is to be estimated. The arrows represent slope measurements at the center of a set of subapertures, and point in the direction which is assigned to positive slope.

Figure 2-4 shows three common arrangements of the slope measurements and the phase estimation grid points. Figure 2-4(a) shows the Fried [14] arrangement in which the phase is to be estimated at the corners of the wavefront sensor subapertures. Figure 2-4(b) shows the Hudgin [15] arrangement in which the slopes are measured along a line between adjacent gridpoints. Figure 2-4(c) shows the Southwell [16] arrangement in which the phase evaluation gridpoints are located at the center of the wavefront sensor subaperture.

In all three cases, the relation between the slope of the wavefront y and the phase at the gridpoints ϕ is

$$y = W\phi. \tag{2.1}$$

The matrix W is the wavefront matrix. For example, with the Fried arrangement,

$$y_{xij} = \frac{1}{2}(\phi_{ij} + \phi_{i+1,j}) - \frac{1}{2}(\phi_{i,j+1} + \phi_{i+1,j+1}) \tag{2.2}$$

$$y_{yij} = \frac{1}{2}(\phi_{i,j} + \phi_{i,j+1}) - \frac{1}{2}(\phi_{i+1,j} + \phi_{i+1,j+1}). \tag{2.3}$$

where i and j represent the row and column on the grid of points, respectively, and y_x and y_y represent the slopes of the wavefront in the x and y directions, respectively. Thus the matrix W is composed of terms that are $0, \frac{1}{2}$, or $-\frac{1}{2}$.

The simplest estimate of the phase results from solving Equation 2.1 for ϕ. If there are the same number of measurements as gridpoints, the solution is simply

$$\phi = W^{-1}y = Z_r y, \tag{2.4}$$

where Z_r is the reconstruction matrix. However, usually more wavefront measurements are available so that the problem is over-determined, and the unweighted least squares estimate of the phase $\hat{\phi}$ is

$$\hat{\phi} = (W^T W)^{-1} W^T y = Z_r y \tag{2.5}$$

This is the solution that is presented by all three authors.

However, the measurements y_{wf} of the wavefront slope y are corrupted by sensor noise so that

$$y_{\text{wf}} = W\phi + \xi, \tag{2.6}$$

where ξ is a white noise process with covariance Ξ. Furthermore, the phase of the wavefront at different points on the grid is correlated

$$Q = \mathbb{E}(\phi\phi^T). \tag{2.7}$$

This correlation provides useful information about the wavefront that can be readily exploited. The optimal linear least squares estimate under these conditions [17, 13] is

$$\hat{\phi} = QW^T(WQW^T + \Xi)^{-1} y_{\text{wf}} = Z_r y_{\text{wf}}. \tag{2.8}$$

A model for the correlation of the wavefront phase is discussed in Section 4.2.

2.3 Correcting the Wavefront

Having produced an estimate of the wavefront phase, the next step is conjugation. For segmented mirrors [13, 12] this is a relatively simple task. Corresponding to each

gridpoint of phase calculation from reconstruction there is an associated segment of the deformable mirror. Each segment can be actuated independently in piston to shorten or lengthen the optical pathlength for this segment of the mirror. More sophisticated segmented mirrors that actuate in piston, tip and tilt exist as well. However, these are not relevant for the work considered herein. To conjugate the wavefront, each segment is simply positioned to counteract the estimated phase at the calculated locations in the manner shown in Figure 2-1. However, segmented mirrors can encounter discontinuities of multiples of the wavelength of light that make them useful for applications involving lasers or monochromatic light sources but limit their usefulness for astronomical observations.

This process is considerably more complicated for continuous mirrors because it is very difficult to actuate at each gridpoint independently. Each actuator has an influence on the entire surface of the deformable mirror. Proper conjugation then requires consideration of the effect that each actuator has at each of the grid points, and more accurately, the effect between grid points as well. The so-called "influence function" for an actuator must be characterized.

Assuming that all deformations in the deformable mirror are small, the influence of any number of actuators adds linearly so that the vector of displacements, y_m, at locations on the mirror is related to the inputs to the actuators, u, by

$$y_m = Fu. \tag{2.9}$$

The influence matrix F determines the amount that any point on the surface of the mirror moves in response to all of the actuator inputs. The displacement required to conjugate the phase error ϕ is determined by the wavelength of the light λ,

$$y_m = \frac{\lambda}{2\pi}\phi. \tag{2.10}$$

From reconstructing the wavefront, an estimate of the phase error ϕ is known, and the required actuator inputs can be determined by solving Equation 2.9. If the number of actuators and the number of phase estimates are equal, the actuator commands can be simply determined by

$$u = F^{-1}\frac{\lambda}{2\pi}\hat{\phi} = S\hat{\phi}, \tag{2.11}$$

where S is the influence correction matrix. However, if more, or fewer actuators than phase estimates are available, a pseudoinverse must be used. Then

$$u = \left(F^T F\right)^{-1} F^T \frac{\lambda}{2\pi} \hat{\phi} = S\hat{\phi}, \tag{2.12}$$

or

$$u = F^T \left(F F^T\right)^{-1} \frac{\lambda}{2\pi} \hat{\phi} = S\hat{\phi}. \tag{2.13}$$

respectively.

Deformable mirrors that are supported and actuated by high impedance piezoelectric or magnetostrictive actuators have relatively narrow influence functions. That is, the influence of a particular actuator has little effect beyond adjacent actuators. Low impedance force actuation results in broader influence functions. Let us look at an example.

Consider for a moment a line of actuators far from any edges of a mirror. Figure 2-5 shows the static influence function for an actuator on a one-dimensional structure, with a number of different actuator types. If the actuators are rigid, and command displacement perfectly, then the influence function for a single actuator looks similar to a sinc function (the solid line in the figure). The displacement of the mirror at the actuator locations is zero except at the location of the commanded actuator where it is one. The actuators, however, do not restrict the slope of the mirror, so that some influence is exerted beyond the adjacent actuator. The influence function is independent of the stiffness of the mirror, though the mirror stiffness determines the magnitude of the restraining forces which are applied by each actuator. The influence function while having a sinc-like shape rolls off more quickly than a sinc function so that at distances more than three actuators away, the influence of the driven actuator is negligible.

Actuators are not perfectly rigid, however, so some displacement is encountered at the actuators which were commanded no displacement. The stiffer the actuator, the more focused the influence function is around the commanded actuator, and the closer the response is to the sinc-like rigid actuator influence function. This can be

then stiff actuators can add sufficient stiffness to the system to raise the natural frequencies of the mirror beyond the range of importance to the problem. In this case a quasi-static approximation for the influence functions can again be sufficient. However, when force actuators are used on a flexible mirror, the natural frequencies of the mirror are determine by the dimensions of the mirror, not by the inter-actuator spacing. Thus the natural frequencies for this type of structure are much lower, with a smaller quasi-static region.

Figure 2-6 shows the frequency response of a collocated actuator and sensor pair on a model of the MMT secondary mirror. The modelling of this mirror which provides this frequency response is discussed in Chapter 4. The frequency response has been calibrated so that the DC gain is one. It can be seen that for this actuator, the quasi-static region in which the frequency response is fairly constant extends only to about 2 Hz. Beyond 2 Hz the response is increasingly dominated by resonant behavior of the mirror. That is, it depends on the structural dynamics. Therefore, the shape of the influence functions shown in Figure 2-5 will vary dramatically with frequency as shown in Figure 2-6. Any reconstruction which attempts to reshape the mirror at a rate faster than about 2 Hz will have to tackle the problem of dynamic influence functions.

2.5 Dynamic Reconstruction

Incorporating the dynamic influence functions, and possibly a dynamic model of the atmospheric distortion, into the reconstruction process results in a procedure that will be called "dynamic reconstruction." The dynamics of the mirror are an important factor to consider because wavefront sensors do not measure the atmosphere directly, but rather the difference in phase between the atmosphere and the optical surfaces of the telescope. These optical surfaces are all rigid except for the deformable mirror. Therefore, the wavefront sensor measures the difference in phase of the atmosphere and the deformable mirror. If there is no distortion in the atmosphere, but the

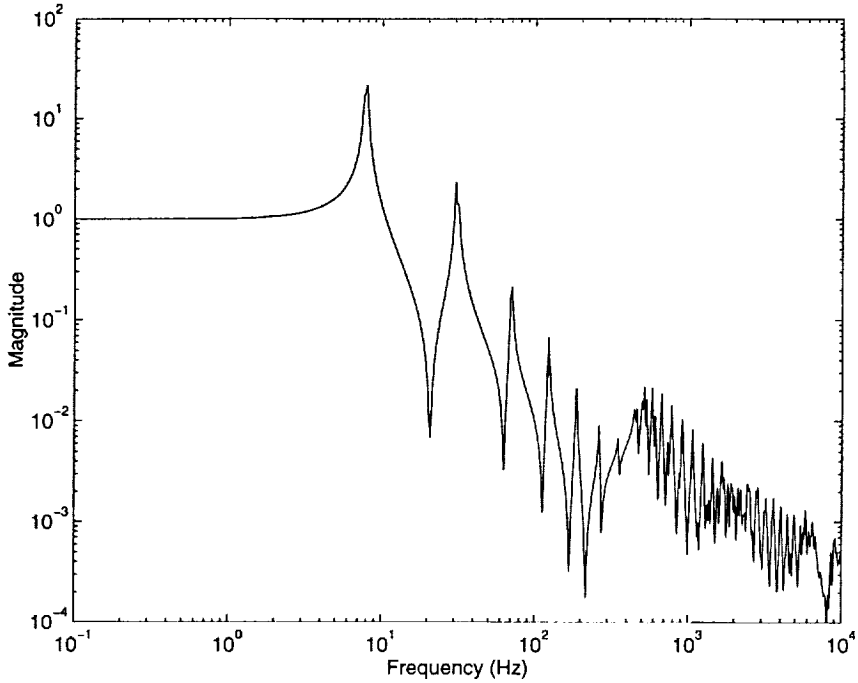

Figure 2-6: Dynamic influence function at actuator location.

deformable mirror is vibrating, for example, the wavefront sensor will register a phase difference.

To begin the process of estimating the phase distortion of the atmosphere, let us introduce a dynamic model of the atmosphere. In state space this will be represented as

$$\dot{\phi} = A_w\phi + B_w w \tag{2.16}$$

$$y_w = C_w\phi, \tag{2.17}$$

where the vector ϕ represents the states of the model which are the phase of the wavefront at a number of locations across the telescope aperture, w is a vector white noise input of unit intensity, and y_w is an output of the model. Note that with $C_w = I$ the outputs of the model are the phase of the wavefront itself. The model is derived more fully in Section 4.2, but the form of the model is introduced here so that the form of the reconstructor can be presented. Note that the covariance of the wavefront

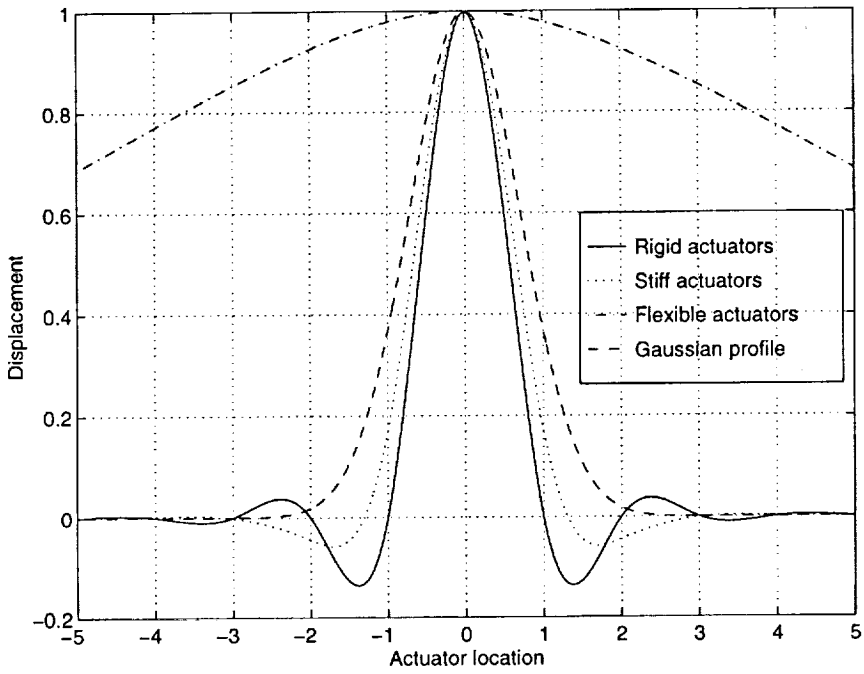

Figure 2-5: Influence functions on a one-dimensional structure.

seen from the dotted line in Figure 2-5 which shows the influence function for stiff but not rigid actuators.

A Gaussian influence function is commonly used [18, 4] as a simple approximation which does not depend on a detailed stiffness model of the mirror. The Gaussian influence function assumes a Gaussian distribution with standard deviation equal to the distance to the adjacent actuator

$$F(x) = exp\left(-\frac{\mid x - x_0 \mid^2}{\delta^2}\right) \tag{2.14}$$

where x_0 is the location of the actuator, and δ is the separation between actuators. In accordance with the Gaussian distribution, the influence of the commanded actuator drops to 37% at one standard deviation, 2% at two standard deviations and is negligible beyond this distance. The influence function for stiff but not rigid actuators similarly is negligible beyond two standard deviations.

The influence function is quite different, however, for flexible actuators. Because little restoring force is exerted by each actuator, displacing the commanded actuator

by one unit displaces nearly the whole structure. Thus the influence function is much broader than for stiff actuators. This is the situation that is encountered in the MMT. The electro-magnetic actuators have zero DC stiffness and thus the influence function is very broad, limited only by the boundary conditions of the mirror.

2.4 The Reconstructor

The reconstruction matrix Z_r provides an estimate of the wavefront phase, $\hat{\phi}$, from the wavefront sensor measurements y_{wf}. The influence correction matrix provides actuator inputs which minimize the error in a given mirror shape. Combined, these provide a set of actuator commands from the wavefront sensor measurements that reduce the wavefront error after reflection from the mirror.

$$u = S\hat{\phi} = SZ_r y_{\text{wf}} = Ry_{\text{wf}}, \tag{2.15}$$

where R is the reconstructor for the system. However, this is not an optimal reconstructor because the least squares problems were solved separately. Wallner [19] has addressed this issue and solved the optimization simultaneously to obtain an optimal reconstructor.

There is one key step that is still missing however. The assumption to this point has been that the influence function, which reflects the influence of the actuators across the mirror, is static. This is not the case. For all systems, the influence function is in fact dynamic, varying as a function of frequency. For systems with very stiff actuators, the frequency range over which the actuator response is nearly static can be large. In this case a quasi-static approximation for the actuator influence function is sufficient. These stiff actuators can be thought of as displacement actuators. The input impedance is sufficiently high that when commanded, these actuators apply a set displacement. However, low stiffness actuators are characterized as force-actuating. That is the input impedance is low enough that these actuators impart forces not displacements to a structure.

This difference between force-actuated and displacement-actuated structures has further importance. When the structure is flexible, such as a deformable mirror,

phase, Q in Equation 2.7, satisfies the Lyapunov equation

$$A_w Q + Q A_w^T + B_w B_w^T = 0. \tag{2.18}$$

Similarly, the dynamics of the deformable mirror, later derived in Section 4.1, are represented in state space as

$$\dot{x}_m = A_m x_m + B_m u \tag{2.19}$$

$$y_m = C_m x_m + D_m u, \tag{2.20}$$

where x_m are the states of the structural dynamics of the mirror, u are the actuator commands and y_m is a vector that represents the displacement of the mirror from nominal at a number of different locations scaled such that the displacement is in the units of the wavefront phase.

The wavefront sensor measures the difference of the mirror displacement y and the wavefront phase y_w, not the phase itself, so the measurement equation, Equation 2.6, becomes,

$$y_{\text{wf}} = W(y_w - y_m) + \xi, \tag{2.21}$$

where ξ is a white noise process with intensity Ξ representing measurement noise, and W, from Equation 2.6, represents the conversion from slope measurements to wavefront phase. Finally, the objective of any control is to minimize the wavefront error across the entire mirror. So the performance variable for the system is defined as

$$z = y_w - y_m. \tag{2.22}$$

Combining these two models, yields the combined system dynamics

$$\dot{x} = Ax + Bu + Lw \tag{2.23}$$

$$z = C_z x + D_{zu} u \tag{2.24}$$

$$y_{\text{wf}} = Cx + Du + \xi \tag{2.25}$$

with

$$x = \begin{bmatrix} \phi \\ x_m \end{bmatrix} \quad A = \begin{bmatrix} A_w & 0 \\ 0 & A_m \end{bmatrix}, \quad B = \begin{bmatrix} 0 \\ B_m \end{bmatrix}, \quad L = \begin{bmatrix} B_w \\ 0 \end{bmatrix}, \tag{2.26}$$

$$C_z = \begin{bmatrix} C_w & -C_m \end{bmatrix}, \quad D_{zu} = D_m, \tag{2.27}$$

$$C = \begin{bmatrix} WC_w & -WC_m \end{bmatrix}, \quad \text{and} \quad D = WD_m. \tag{2.28}$$

The performance objective is to minimize the root mean square (RMS) wavefront error (z) subject to the atmospheric disturbance (w) and the sensor noise (ξ). It would also be advantageous to minimize the use of controls so we are lead directly into a Linear Quadratic Gaussian (LQG) [20] framework for control. Defining the performance objective as

$$J = \mathbb{E}\left\{ z^T z + \rho u^T u \right\} \tag{2.29}$$

the optimal control is given by the compensator represented by

$$\dot{\hat{x}} = (A - BK - FC + FDK)\,\hat{x} + F y_{\text{wf}} \tag{2.30}$$

$$u = K\hat{x} \tag{2.31}$$

where

$$K = -\frac{1}{\rho} B^T P \tag{2.32}$$

$$F = QC^T \Xi^{-1}, \tag{2.33}$$

and P and Q are the symmetric positive semi-definite solutions of the following Riccati equations

$$0 = PA + A^T P + C_z^T C_z - \frac{1}{\rho} PBB^T P \tag{2.34}$$

$$0 = AQ + QA^T + LL^T - QC^T \Xi^{-1} CQ. \tag{2.35}$$

The connection between this LQG control problem and the reconstructor of the previous sections can be seen by splitting the control into its component parts, estimator and regulator. By the separation principle [20], the LQG controller can be split into an optimal estimator and an optimal regulator.

The goal of the estimator is to estimate the phase of the wavefront and the states of the structural model. The optimal linear least squares estimator, the Kalman Filter[20], for this system is given by the dynamic system

$$\dot{\hat{x}} = A\hat{x} + Bu + F(y_{\text{wf}} - C\hat{x} - Du) \tag{2.36}$$

where $\hat{x}$ is the estimate of the states, *i.e.,* the wavefront phase estimates and structural state estimates. This estimator provides the dynamic and continuous time equivalent of Equation 2.8.

Given a perfect measure of all the states of the system, the goal of the regulator is to minimize the performance objective, Equation 2.29. And the result is simply the full state feedback

$$u = -\frac{1}{\rho} B^T P x. \tag{2.37}$$

This is the dynamic analogue of the inversion of the static influence function given in Equations 2.11-2.13. The combination of optimal regulator and estimator results from applying the full state feedback gains K to the estimates of the states $\hat{x}$ since the states themselves are not available for feedback. This is intuitively what was done in the static case, and by the separation principle it is optimal in the dynamic case.

Thus it can be seen that solving the LQG problem for this system is the dynamic equivalent of the two step process of reconstructing the wavefront and inverting the static influence function. Hence it is "dynamic reconstruction." Having expressed the reconstruction process as an optimal control problem, it is now possible to generalize and use any of a wide variety of modern state space control techniques to control the mirror. This process will be discussed further in Chapter 5.

Chapter 3

Circulant Systems

Adaptive optics systems typically have a large number of actuators for providing shape control of a deformable mirror. The number of sensors to measure the distortion of the atmosphere is also very large. Dealing with such a large number of inputs and outputs in an optimal control problem can be very difficult. When actuator and sensor dynamics are included, the number of states of a system increases in proportion to the number of inputs and outputs. This increase in dimension results in very large Riccati equations which may be poorly conditioned and take a large amount of computation to solve. Furthermore, feeding information from every sensor to every actuator through a compensator requires a large amount of real-time computation. But, adaptive optics systems also tend to exhibit a high degree of symmetry. Because mirrors are general circular, the symmetry is circular in nature. It is possible to exploit this symmetry to make the control problems that must be solved, smaller; and reduce the number of floating point operations required to implement the resulting controller in real time. Symmetry is exploited through the use of circulant matrix theory.

3.1 Circulant Matrices

A circulant matrix [21, 22, 23] is a square $N \times N$ matrix characterized by the fact that every row (or column) has the same elements, except that the elements in subsequent rows (columns) are rotated one position to the right (down), with the last column

(row) mapping back to the first on rotation. The general form is shown in the matrix

$$A = \begin{bmatrix} a_0 & a_{N-1} & a_{N-2} & \cdots & a_1 \\ a_1 & a_0 & a_{N-1} & & a_2 \\ a_2 & a_1 & a_0 & & a_3 \\ \vdots & & & \ddots & \vdots \\ a_{N-1} & a_{N-2} & a_{N-3} & \cdots & a_0 \end{bmatrix}. \tag{3.1}$$

A useful property of a circulant matrix is that its eigenvectors are known, and need not be calculated. The circulant matrix in Equation 3.1 has eigenvectors v_i, for $i = 0, \ldots, N-1$, which form the eigenvector matrix

$$V = \begin{bmatrix} v_0 & v_1 & \cdots & v_{N-1} \end{bmatrix} = \frac{1}{\sqrt{N}} \begin{bmatrix} 1 & 1 & 1 & \cdots & 1 \\ 1 & \omega_N & \omega_N^2 & \cdots & \omega_N^{(N-1)} \\ 1 & \omega_N^2 & \omega_N^4 & \cdots & \omega_N^{2(N-1)} \\ \vdots & & & \ddots & \vdots \\ 1 & \omega_N^{(N-1)} & \omega_N^{2(N-1)} & \cdots & \omega_N^{(N-1)(N-1)} \end{bmatrix} \tag{3.2}$$

where,

$$\omega_N = e^{j\frac{2\pi}{N}}, \tag{3.3}$$

such that the matrix Λ, where

$$\Lambda = V^{-1}AV, \tag{3.4}$$

is the diagonal eigenvalue matrix. The eigenvector matrix V can be written simply as

$$(V_{ij}) = \frac{1}{\sqrt{N}}\omega_N^{(i-1)(j-1)}, \tag{3.5}$$

where V_{ij} denotes the ij^{th} element of the matrix V. The matrix V is symmetric since

$$V_{ij} = V_{ji}. \tag{3.6}$$

Furthermore, because

$$(V^{-1})_{ij} = \frac{1}{\sqrt{N}}\omega_N^{-(i-1)(j-1)} = \frac{1}{\sqrt{N}}(\omega_N^*)^{(i-1)(j-1)}, \tag{3.7}$$

where $()^*$ indicates the complex conjugate, and V^{-1} is symmetric, V is a unitary matrix *i.e.*,

$$V^{-1} = V^H \tag{3.8}$$

where $()^H$ denotes the Hermitian, or complex conjugate transpose. Therefore the eigenvalue matrix can be found from

$$\Lambda = V^H A V. \tag{3.9}$$

However, there is an easier way to calculate the eigenvalue matrix by recognizing that the circulant matrix A is a matrix operator that represents a circular convolution. Consider the relation $y = Ax$ written out fully as

$$\begin{bmatrix} y_0 \\ y_1 \\ y_2 \\ \vdots \\ y_{N-1} \end{bmatrix} = \begin{bmatrix} a_0 & a_{N-1} & a_{N-2} & \cdots & a_1 \\ a_1 & a_0 & a_{N-1} & & a_2 \\ a_2 & a_1 & a_0 & & a_3 \\ \vdots & & & \ddots & \vdots \\ a_{N-1} & a_{N-2} & a_{N-3} & \cdots & a_0 \end{bmatrix} \begin{bmatrix} x_0 \\ x_1 \\ x_2 \\ \vdots \\ x_{N-1} \end{bmatrix}. \tag{3.10}$$

The relationship between individual terms in x and y can be written more succinctly as

$$y_k = \sum_{i=0}^{N-1} a_i x_{(k-i) \bmod N}, \tag{3.11}$$

where $l \bmod m$ denotes the integer $n \in \{0, \ldots, m-1\}$ such that $l+n$ is divisible by m. This relation is a circular convolution. The convolution operation can be transformed to multiplication through a discrete Fourier transform leading to

$$\overline{y}_k = \sum_{i=0}^{N-1} y_i e^{-\jmath \frac{2\pi i k}{N}} = \sum_{i=0}^{N-1} y_i \omega_N^{-ik} \tag{3.12}$$

$$\overline{a}_k = \sum_{i=0}^{N-1} a_i e^{-\jmath \frac{2\pi i k}{N}} = \sum_{i=0}^{N-1} a_i \omega_N^{-ik} \tag{3.13}$$

$$\overline{x}_k = \sum_{i=0}^{N-1} x_i e^{-\jmath \frac{2\pi i k}{N}} = \sum_{i=0}^{N-1} x_i \omega_N^{-ik} \tag{3.14}$$

so that

$$\overline{y}_k = \overline{a}_k \overline{x}_k \tag{3.15}$$

for $k = 0, 1, \ldots, N-1$, which are a set of decoupled scalar equations. If x and y are temporal variables, then $\overline{y}$ and $\overline{x}$ are in the temporal frequency domain with frequency variable k. If x and y are spatial variables, then $\overline{y}$ and $\overline{x}$ are in the spatial frequency domain. In this work, these are spatial variables because they generally represent positions around a deformable mirror, and a spatial frequency interpretation will be used.

The discrete Fourier transform can be represented in matrix form by the matrix V^H which is called the Fourier matrix[21] scaled by $\sqrt{N}$. Thus,

$$\overline{y} = \sqrt{N} V^H y \tag{3.16}$$

$$\overline{x} = \sqrt{N} V^H x \tag{3.17}$$

$$\overline{y} = \sqrt{N} V^H A x = V^H A V \overline{x} = \Lambda \overline{x} = \overline{A} \overline{x} \tag{3.18}$$

The matrix $\overline{A} = \text{diag}[\overline{a}_k]$ equals the eigenvalue matrix of A, Λ, and thus it can be seen that the eigenvalues of A are the discrete Fourier transform of $\{a_i\}$, where $\{a_i\}$ denotes the sequence $a_0, a_1, \ldots, a_{N-1}$.

The discrete Fourier transform of $\{a_i\}$ is in general complex, thus the matrix $\overline{A}$ is complex. But because $\{a_i\}$ is a real-valued sequence,

$$\overline{a}_k = \overline{a}^*_{N-k}, \tag{3.19}$$

the diagonal matrix $\overline{A}$ can be converted to a block diagonal but real-valued form $\overline{A}_R$. Also note from Equations 3.2 and 3.5 that eigenvectors v_k and v_{N-k} are complex conjugates.

The columns of V can be reordered so that conjugate pairs of eigenvectors are adjacent through postmultiplication by a unitary permutation matrix P. Each submatrix of conjugate pairs can be multiplied by another unitary matrix

$$U_2 = \frac{1}{\sqrt{2}} \begin{bmatrix} 1 & -\jmath \\ 1 & \jmath \end{bmatrix} \tag{3.20}$$

to form a real-valued matrix.

$$\begin{bmatrix} v_k & v_{N-k} \end{bmatrix} U_2 = \begin{bmatrix} \sqrt{2}\text{Re}\,(v_k) & \sqrt{2}\text{Im}\,(v_k) \end{bmatrix}. \tag{3.21}$$

Combining these steps results in the matrix

$$T = VPU \tag{3.22}$$

where U is a block diagonal matrix composed of elements that are either 1 or U_2 corresponding to real and complex pairs of eigenvalues in V. The resulting matrix T is once again unitary so that

$$T^{-1} = U^{-1}P^{-1}V^{-1} = U^H P^H V^H = T^H. \tag{3.23}$$

But T is a real-valued matrix so that

$$T^H = T^T = T^{-1}. \tag{3.24}$$

The matrix T can be formed directly because all the eigenvectors are known *a priori*,

$$T = \begin{cases} \left[\begin{array}{ccccccc} v_0 & \sqrt{2}\mathrm{Re}\left(v_1\right) & \sqrt{2}\mathrm{Im}\left(v_1\right) & \cdots & \sqrt{2}\mathrm{Re}\left(v_{\frac{N}{2}-1}\right) & \sqrt{2}\mathrm{Im}\left(v_{\frac{N}{2}-1}\right) & v_{\frac{N}{2}} \end{array} \right] & \text{if N even} \\ \left[\begin{array}{ccccccc} v_0 & \sqrt{2}\mathrm{Re}\left(v_1\right) & \sqrt{2}\mathrm{Im}\left(v_1\right) & \cdots & \sqrt{2}\mathrm{Re}\left(v_{\frac{N-1}{2}}\right) & \sqrt{2}\mathrm{Im}\left(v_{\frac{N-1}{2}}\right) \end{array} \right] & \text{if N odd} \end{cases} \tag{3.25}$$

where

$$\left(\mathrm{Re}\left(v_i\right)\right)_k = \frac{1}{\sqrt{N}} \cos \frac{2\pi i(k-1)}{N} \tag{3.26}$$

$$\left(\mathrm{Im}\left(v_i\right)\right)_k = \frac{1}{\sqrt{N}} \sin \frac{2\pi i(k-1)}{N}. \tag{3.27}$$

Using this matrix T in place of the eigenvector matrix V yields the block diagonal real-valued matrix

$$\overline{A}_R = T^T A T = \begin{bmatrix} \overline{a}_0 & 0 & 0 & 0 & 0 & \cdots & 0 \\ 0 & \mathrm{Re}\left(\overline{a}_1\right) & \mathrm{Im}\left(\overline{a}_1\right) & 0 & 0 & & 0 \\ 0 & -\mathrm{Im}\left(\overline{a}_1\right) & \mathrm{Re}\left(\overline{a}_1\right) & 0 & 0 & & 0 \\ 0 & 0 & 0 & \mathrm{Re}\left(\overline{a}_2\right) & \mathrm{Im}\left(\overline{a}_2\right) & & 0 \\ 0 & 0 & 0 & -\mathrm{Im}\left(\overline{a}_2\right) & \mathrm{Re}\left(\overline{a}_2\right) & & 0 \\ \vdots & & & & & \ddots & \\ 0 & 0 & 0 & 0 & 0 & & \overline{a}_{\frac{N}{2}} \end{bmatrix} \tag{3.28}$$

shown here assuming N is even. The last row and column would not be present if N were odd. The matrix $\overline{A}_R$ consists of two scalar blocks and $(\frac{N}{2}-1)$, 2×2 blocks if N is even, and one scalar block and $(\frac{N-1}{2}$, 2×2 blocks if N is odd.

The number of real eigenvalues and eigenvectors for A depends on whether N is even or odd. If N is even there are two, and therefore there are two smaller blocks in $\overline{A}_R$, otherwise there is only one. To understand why this is so, observe that the eigenvector v_i composed of elements

$$(v_i)_k = \frac{1}{\sqrt{N}}\cos\frac{2\pi(k-1)i}{N} + \frac{j}{\sqrt{N}}\sin\frac{2\pi(k-1)i}{N}, \tag{3.29}$$

is real when

$$\sin\frac{2\pi(k-1)i}{N} = 0 \quad \forall k, \tag{3.30}$$

which occurs only when $i=0$ or $i=\frac{N}{2}$. If N is odd then $\frac{N}{2}$ is not an integer, and there is only one real-valued eigenvector. Another way to view this is to plot ω_N^{ki} as in Figure 3-1 which shows ω_N^{ki} plotted for $N=16$. There are only N distinct values for ω_N^{ki} which is a periodic function. For a given i, the terms in the eigenvector v_i can be found by starting at the 'x' for which $\omega_N^{ki}=1$ moving counterclockwise around the unit circle by i steps, $N-1$ times. In doing this, complex values for the eigenvector occur unless you never move, $i=0$, or you move half way round the circle with each step, $i=\frac{N}{2}$. Thus, only if N is divisible by two can one move half way round the circle with each step, and there is only one real block if N is not divisible by two.

3.2 Block Circulant Matrices

A block circulant matrix is an $Nl\times Nm$ matrix in which $l\times m$ matrices $A_0,\ldots,A_{N-1}$ replace the scalars in the circulant matrix A in Equation 3.1 to yield the matrix

$$A = \begin{bmatrix} A_0 & A_{N-1} & A_{N-2} & \cdots & A_1 \\ A_1 & A_0 & A_{N-1} & & A_2 \\ A_2 & A_1 & A_0 & & A_3 \\ \vdots & & & \ddots & \\ A_{N-1} & A_{N-2} & A_{N-3} & & A_0 \end{bmatrix}. \tag{3.31}$$

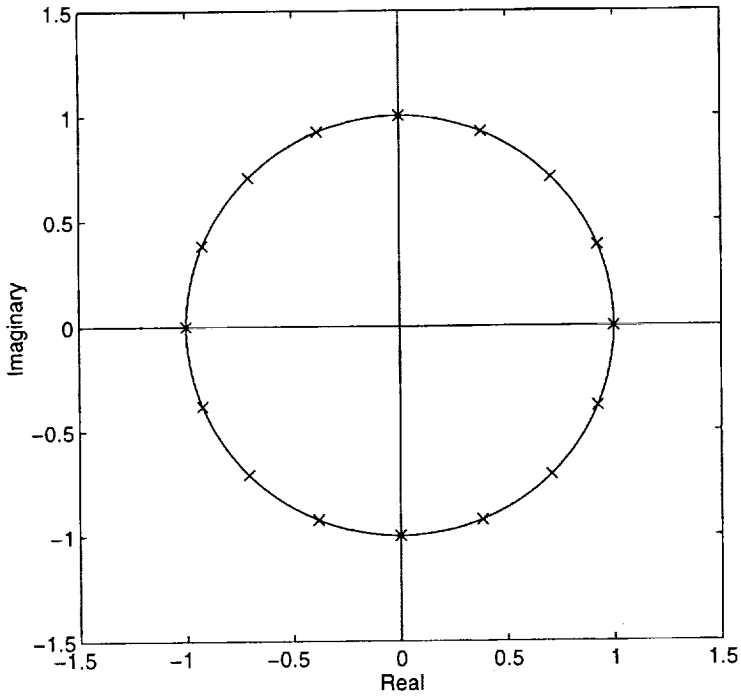

Figure 3-1: Values of $\omega_N^{ki} = e^{j\frac{2\pi ki}{N}}$ for $N = 16$, $k = 0, \ldots, 15$, $i = 0, \ldots, 15$ lie on unit circle in complex conjugate pairs except $ki = 0$ and $ki = 8$ which are real.

The eigenvectors of block circulant matrices are not known *a priori* as they are for circulant matrices. However, the matrix V and discrete Fourier transform are still relevant. The utility of the circulant form in Section 3.1 is that the matrix A can be easily diagonalized. *Block* circulant matrices can be easily *block* diagonalized in a similar manner. The matrix

$$V_m = V \otimes I_m \tag{3.32}$$

where I_m is the $m \times m$ Identity matrix and $\otimes$ is the Kronecker product, can be used to block diagonalize the block circulant matrix A in the same manner as V diagonalizes the circulant matrix A.

$$\overline{A} = V_l^H A V_m = \begin{bmatrix} \overline{A}_0 & 0 & 0 & \cdots & 0 \\ 0 & \overline{A}_1 & 0 & & \\ 0 & 0 & \overline{A}_2 & & \\ \vdots & & & \ddots & \\ 0 & & & & \overline{A}_{N-1} \end{bmatrix} \tag{3.33}$$

where

$$\overline{A}_k = \sum_{i=0}^{N-1} A_i e^{-\jmath \frac{2\pi ik}{N}} = \sum_{i=0}^{N-1} A_i \omega_N^{-ik}. \tag{3.34}$$

Note that $\{\overline{A}\}$ is the discrete Fourier transform of $\{A\}$ on an element by element basis in the matrix.

$\overline{A}$ is again complex in general, but a real-valued block diagonal matrix can be formed by using the transformation

$$T_m = T \otimes I_m. \tag{3.35}$$

The resulting real-valued transformed matrix is

$$\overline{A}_R = T_l^T A T_m = \begin{bmatrix} \overline{A}_0 & 0 & 0 & 0 & 0 & \cdots & 0 \\ 0 & \mathrm{Re}\left(\overline{A}_1\right) & \mathrm{Im}\left(\overline{A}_1\right) & 0 & 0 & & 0 \\ 0 & -\mathrm{Im}\left(\overline{A}_1\right) & \mathrm{Re}\left(\overline{A}_1\right) & 0 & 0 & & 0 \\ 0 & 0 & 0 & \mathrm{Re}\left(\overline{A}_2\right) & \mathrm{Im}\left(\overline{A}_2\right) & & 0 \\ 0 & 0 & 0 & -\mathrm{Im}\left(\overline{A}_2\right) & \mathrm{Re}\left(\overline{A}_2\right) & & 0 \\ \vdots & & & & & \ddots & \\ 0 & 0 & 0 & 0 & 0 & & \overline{A}_{\frac{N}{2}} \end{bmatrix} \tag{3.36}$$

shown here assuming N is even. The matrix $\overline{A}_R$ consists of two $l \times m$ blocks and $(\frac{N}{2} - 1)$, $2l \times 2m$ blocks if N is even, and one $l \times m$ block and $(\frac{N-1}{2})$, $2l \times 2m$ blocks if N is odd.

3.3 Circulant Systems

A standard input output system can be represented in state space as:

$$\begin{aligned} \dot{x} &= Ax + B_w w + B_u u \\ z &= C_z x + D_{zw} w + D_{zu} u \\ y &= C_y x + D_{yw} w + D_{yu} u\,, \end{aligned} \tag{3.37}$$

where $x \in \mathbb{R}^{n_x}$ represents the states of the system, $w \in \mathbb{R}^{n_w}$ is a set of disturbances, $u \in \mathbb{R}^{n_u}$ are control inputs, $z \in \mathbb{R}^{n_z}$ are performance variables, $y \in \mathbb{R}^{n_y}$ are measurements used for feedback, and n_x, n_w, n_u, n_z, and n_y are the number of states,

disturbances, control inputs, performance variables and feedback measurements in the system, respectively.

For a system to be block circulant, all the matrices in Equation 3.37- A, B_w, B_u, C_z, C_y, D_{zw}, D_{zu}, D_{yw}, and D_{yu}- must be block circulant. Furthermore, the number of circulant blocks N in each matrix must be the same. Under these circumstances, the system can be decoupled into N smaller systems with complex-valued matrices, or floor($\frac{N}{2}+1$) systems with real-valued matrices, where floor() indicates rounding down to the nearest integer. The decoupled system dynamics are obtained by using the transformations

$$\overline{x} = V_{\frac{n_x}{N}}^H x \tag{3.38}$$

$$\overline{y} = V_{\frac{n_y}{N}}^H y \tag{3.39}$$

$$\overline{z} = V_{\frac{n_z}{N}}^H z \tag{3.40}$$

$$\overline{w} = V_{\frac{n_w}{N}}^H w \tag{3.41}$$

$$\overline{u} = V_{\frac{n_u}{N}}^H u \tag{3.42}$$

where the scale factor of $\sqrt{N}$ has been dropped to obtain complex-valued systems, or

$$\overline{x}_R = T_{\frac{n_x}{N}}^T x \tag{3.43}$$

$$\overline{y}_R = T_{\frac{n_y}{N}}^T y \tag{3.44}$$

$$\overline{z}_R = T_{\frac{n_z}{N}}^T z \tag{3.45}$$

$$\overline{w}_R = T_{\frac{n_w}{N}}^T w \tag{3.46}$$

$$\overline{u}_R = T_{\frac{n_u}{N}}^T u \tag{3.47}$$

to obtain real-valued systems. The decoupled dynamics after these transformations are applied are

$$\begin{aligned} \dot{\overline{x}}_i &= \overline{A}_i\overline{x}_i + \overline{B_{w_i}}\overline{w}_i + \overline{B_u}\overline{u}_i \\ \overline{z}_i &= \overline{C_{z_i}}\overline{x}_i + \overline{D_{zw_i}}\overline{w}_i + \overline{D_{zu_i}}\overline{u}_i \\ \overline{y}_i &= \overline{C_{y_i}}\overline{x}_i + \overline{D_{yw_i}}\overline{w}_i + \overline{D_{yu_i}}\overline{u}_i\,, \end{aligned} \tag{3.48}$$

for $i = 0, \ldots, n_b - 1$, where the subscript R has been dropped so that both complex and real blocks can be represented, $n_b = N$ for complex matrices or $n_b = \text{floor}(\frac{N}{2}+1)$

for real-valued matrices. The dimensions of the decoupled systems correspond to the variables n_{hi} where $h = \{x, w, u, z, y\}$. Then $n_{hi} = \frac{n_h}{N}$ for complex blocks and the smaller real blocks, and $n_{hi} = \frac{2n_h}{N}$ for the larger real blocks.

Circulant systems exhibit the property that the transfer function matrix of the system

$$G(s) = \begin{bmatrix} G_{zw}(s) & G_{zu(s)} \\ G_{yw}(s) & G_{yu}(s) \end{bmatrix}, \tag{3.49}$$

consists of circulant blocks $G_{ij}(s)$ where $G_{ij}(s) = C_i(sI - A)^{-1}B_j + D_{ij}$. That is, each of the input/output, input/performance, disturbance/performance, and disturbance/output relationships is circulant.

To interpret what it means for a system to be circulant, consider Figure 3-2. In this figure, a system is represented which consists of four subsystems ($n_b = 4$). The interaction between each of the subsystems, A_i for $i = 1, 2, 3$, including the self interaction, A_0, is represented by arrows connecting the subsystems. Two characteristics make this system circulant. First, all of the subsystems are identical. They have the same self dynamics A_0. Second, the interaction between a particular subsystem and the remaining subsystems is exactly the same for all of the subsystems. Another way to view this is that there is an arbitrariness about the origin of the system. The system looks exactly the same under the current ordering of subsystems, as it would if all the subsystems were shifted circularly so that subsystem 0 becomes subsystem 1, subsystem 1 becomes subsystem 2, and so on. It is this rotational symmetry which results in the circular convolution of Equation 3.11 and distinguishes this as a circulant system.

This decoupling of the system dynamics into smaller systems is precisely the advantage that can be derived by exploiting circulance. In the control of finite dimensional systems, Lyapunov and Riccati-type equations very often arise for the calculation of properties such as performance and optimal feedback gains. The computation required for solving these equations goes as $O(n_x^3)$. It would be advantageous if these equations also decoupled along with the system dynamics.

To show that these equations do decouple, a few preliminaries are required. In

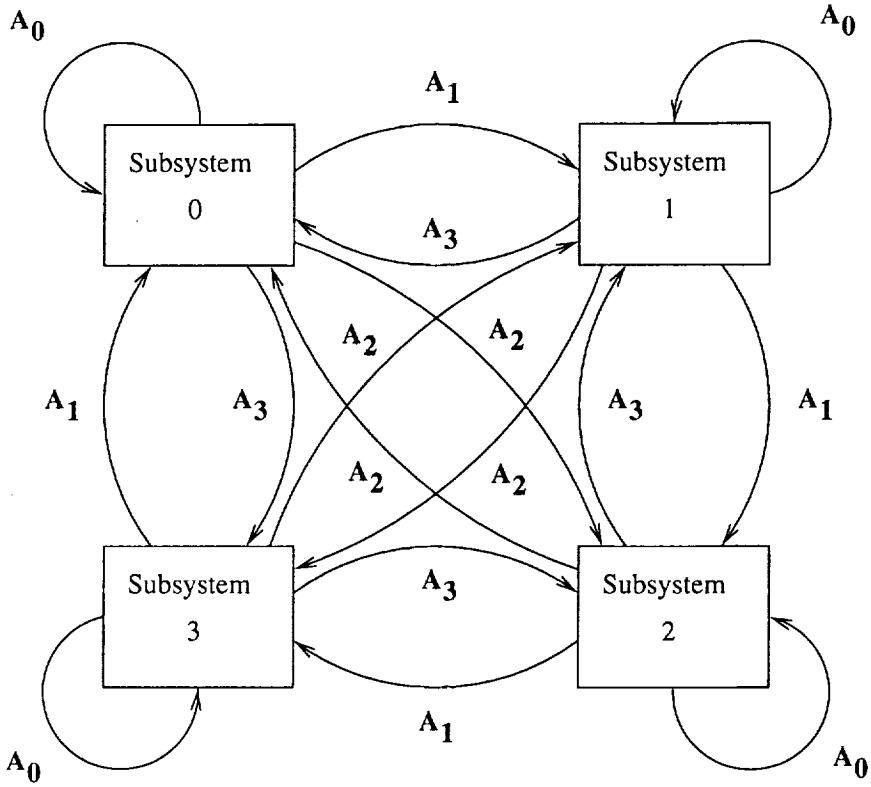

Figure 3-2: The dynamics of a circulant system consisting of 4 identical subsystems with identical interaction shown schematically.

Ref. [22] it is noted that $\overline{A^T} = \overline{A}^H$. $\overline{A^T}_R$ is composed of blocks of the form (Equation 3.28)

$$\begin{bmatrix} \mathrm{Re}\left(\overline{A^T}_i\right) & \mathrm{Im}\left(\overline{A^T}_i\right) \\ -\mathrm{Im}\left(\overline{A^T}_i\right) & \mathrm{Re}\left(\overline{A^T}_i\right) \end{bmatrix} = \begin{bmatrix} \mathrm{Re}\left(\overline{A}_i^H\right) & \mathrm{Im}\left(\overline{A}_i^H\right) \\ -\mathrm{Im}\left(\overline{A}_i^H\right) & \mathrm{Re}\left(\overline{A}_i^H\right) \end{bmatrix} \tag{3.50}$$

$$= \begin{bmatrix} \mathrm{Re}\left(\overline{A}_i^T\right) & -\mathrm{Im}\left(\overline{A}_i^T\right) \\ \mathrm{Im}\left(\overline{A}_i^T\right) & \mathrm{Re}\left(\overline{A}_i^T\right) \end{bmatrix} \tag{3.51}$$

$$= \begin{bmatrix} \mathrm{Re}\left(\overline{A}_i\right) & \mathrm{Im}\left(\overline{A}_i\right) \\ -\mathrm{Im}\left(\overline{A}_i\right) & \mathrm{Re}\left(\overline{A}_i\right) \end{bmatrix}^T \tag{3.52}$$

Therefore

$$\overline{A^T}_R = \overline{A}_R{}^T. \tag{3.53}$$

The Lyapunov equation

$$0 = AP + PA^T + BB^T \tag{3.54}$$

can be block diagonalized through the following steps,

$$0 = T_{n_x}^T A P T_{n_x} + T_{n_x}^T P A^T T_{n_x} + T_{n_x}^T B B^T T_{n_x} \tag{3.55}$$

$$0 = T_{n_x}^T A T_{n_x} T_{n_x}^T P T_{n_x} + T_{n_x}^T P T_{n_x} T_{n_x}^T A^T T_{n_x} + T_{n_x}^T B T_{n_u} T_{n_u}^T B^T T_{n_x} \tag{3.56}$$

$$0 = \overline{A}_R \overline{P}_R + \overline{P}_R \overline{A^T}_R + \overline{B}_R \overline{B^T}_R \tag{3.57}$$

$$0 = \overline{A}_R \overline{P}_R + \overline{P}_R \overline{A}_R{}^T + \overline{B}_R \overline{B}_R{}^T \tag{3.58}$$

so that

$$0 = \overline{A}_{iR} \overline{P}_{iR} + \overline{P}_{iR} \overline{A}_{iR}{}^T + \overline{B}_{iR} \overline{B}_{iR}{}^T \tag{3.59}$$

for $i = 1, \ldots, n_b - 1$. Thus the computation required to solve this equation has dropped from $O(n_x^3)$ to roughly $O(\frac{N}{2}(\frac{2n_x}{N})^3)$ plus the cost of transforming to and from the circulant form which is $O((\frac{n_x}{N})^2 N \log_2 N)$ if a fast Fourier transform can be used, *i.e.*, if N is a power of 2.

Similarly Riccati equations such as

$$PA + A^T P + C_z^T C_z - P B_u (D_{yu}^T D_{yu})^{-1} B_u^T P = 0 \tag{3.60}$$

decouple to become

$$\overline{P}_R \overline{A}_R + \overline{A}_R{}^T \overline{P}_R + \overline{C_z}_R{}^T \overline{C_z}_R - \overline{P}_R \overline{B_u}_R (\overline{D_{yu}}_R{}^T \overline{D_{yu}}_R)^{-1} \overline{B_u}_R{}^T \overline{P}_R = 0. \tag{3.61}$$

Henceforth the subscript R will be dropped, and it is assumed that the real-valued transformations are used unless otherwise specified.

The solution of these equations is generally done off-line, so while it is a great benefit that it is faster to compute the solutions by exploiting circulance, it may not have been necessary in order to solve the problem. However, the reduction in dimension of the problem also means that for very large order systems, where the numerics of solving these equations become very poorly conditioned, solving these equations becomes possible.

For implementation of real-time control, computation time is much more important, and for large numbers of actuators and sensors, significant savings can be made. Any linear controller can be put in the form

$$\begin{aligned} \dot{x_c} &= A_c x_c + B_c y \\ u &= C_c x_c + D_c y \,, \end{aligned} \tag{3.62}$$

where $x_c \in \mathbb{R}^{n_c}$ represents the states of the compensator, representing a system in which measurements y drive a dynamic system of gains to create control signals u. Typically full order compensators are generated from optimal control problems so that $n_c = n_x$. However, A_c can always be transformed to a block diagonal form with 2×2 blocks (unless the system has large Jordan blocks). Thus the overall computation required to implement the control is $(2+n_y+n_u)n_c+n_yn_u$ multiplications. A circulant compensator, which results from circulant Riccati equations, requires only about $2(1 + \frac{n_y}{N} + \frac{n_u}{N})n_c + 2\frac{n_yn_u}{N}$ multiplications for the circulant compensator, and $(n_y + n_u)N$ multiplications to transform the inputs and outputs to circulant form, where N is the number of symmetric subsystems into which the problem can be divided. For compensators with only a small number of inputs and outputs (though it should be noted that there must be at least some multiple of N), the computational savings may be small. However for systems in which n_y and n_u are large, the savings can be substantial.

There is a trade-off between computation required for compensator calculations and computation required for the transformation into the decoupled coordinates. Therefore there is an optimum amount of decoupling. Given n_y, n_u, and n_c, it is possible to calculate the N that minimizes the function, $F(N)$, which is the number of floating point multiplications

$$F(N) = 2(1 + \frac{n_y}{N} + \frac{n_u}{N})n_c + 2\frac{n_yn_u}{N} + (n_y + n_u)N. \tag{3.63}$$

To find the minimum number of computations, differentiate $F(N)$ with respect to N and set the derivative to zero.

$$\frac{dF}{dN} = -\frac{2(n_y + n_u)n_c + 2n_yn_u}{N^2} + n_y + n_u = 0 \tag{3.64}$$

$$n_y + n_u = \frac{2(n_y + n_u)n_c + 2n_yn_u}{N^2} \tag{3.65}$$

$$N_{opt} = \sqrt{2\left(n_c + \frac{n_yn_u}{n_y + n_u}\right)}. \tag{3.66}$$

Finally, verify that a minimum is achieved by checking that the second derivative is positive.

$$\frac{d^2F}{dN^2} = \frac{4(n_y + n_u)n_c + 2n_yn_u}{N^3} > 0. \tag{3.67}$$

Unfortunately, N is not a continuous function, but is in fact an integer that is a common factor of n_u, n_y, and n_c. Thus, the optimum is achieved at either the nearest permissible $N < N_{opt}$ or the nearest permissible $N > N_{opt}$. In addition, other constraints in the problem, such as geometric distribution of sensors and actuators, may prevent one from realizing all of the computational savings

3.4 Modelling of Circulant Systems

The continuum dynamics of structures are represented mathematically by partial differential equations (PDEs). However, only under exceptional circumstances can these PDEs be solved analytically. Therefore the dynamics of structures are generally solved through the use of the second order ordinary matrix differential equation (ODE)

$$M\ddot{q} + C_{\mathrm{D}}\dot{q} + Kq = Fu, \tag{3.68}$$

where M is the mass matrix, C_{D} is the damping matrix, K is the stiffness matrix, F is the forcing matrix for the system, q is the vector of degrees of freedom, and u is the input vector. Outputs of interest, y, are generally of the form of some linear combination of states which correspond to the degrees of freedom of the system and their rates.

$$y = S_p q + S_v \dot{q}, \tag{3.69}$$

where S_p selects the position component of the output and S_v selects the velocity component of the output. The matrices for this ODE can be arrived at through many different techniques such as the Finite Element Method[24] or the Rayleigh-Ritz Method[25] just to name a few. However, the ODE only approximates the PDE for the system, and thus the solutions of the ODE are only approximate. It is often difficult to arrive at an analytical measure of damping in continuum dynamics, so modal damping is often assumed. When C_{D} is not known explicitly, to achieve the same damping ratio, ζ, in all modes, the damping matrix C_{D} can be set to

$$C_{\mathrm{D}} = 2\zeta M^{\frac{1}{2}} \left(M^{-\frac{1}{2}} K M^{-\frac{1}{2}} \right)^{\frac{1}{2}} M^{\frac{1}{2}}, \tag{3.70}$$

where $()^{\frac{1}{2}}$, indicates the symmetric matrix square root.

For control systems analysis and synthesis, first order differential equations of the form of Equation 3.37 are typically used. Two methods for converting the second order ODEs to first order ODEs will be presented. The first is called the direct method because it deals directly with the mass, stiffness and damping matrices. This method is most applicable when the number of degrees of freedom in the system is small. The second method is called the modal method, and it uses eigenvalues and eigenvectors of a modal solution to the ODE.

3.4.1 Direct Method

The first step in the direct method is to define the states of the system

$$x = \begin{bmatrix} q \\ \dot{q} \end{bmatrix} \tag{3.71}$$

Combining the disturbances, w, and control inputs, u, and labeling it u', and similarly combining performance z and measurement outputs y together as y', then the system can be represented as

$$\begin{aligned} \dot{x} &= Ax + Bu' \\ y' &= Cx + Du', \end{aligned} \tag{3.72}$$

with

$$A = \begin{bmatrix} 0 & I \\ M^{-1}K & -M^{-1}C_{\text{D}} \end{bmatrix} \tag{3.73}$$

$$B = \begin{bmatrix} 0 \\ M^{-1}F \end{bmatrix} \tag{3.74}$$

$$C = \begin{bmatrix} S_p & S_v \end{bmatrix} \tag{3.75}$$

$$D = 0. \tag{3.76}$$

The number of degrees of freedom in a FEM may be very large, so that a model of this form will be very large. All of these degrees of freedom are not usually necessary, but

are included in a FEM to improve the accuracy of modal frequency and mode shape calculations. Thus an alternative method for deriving the system matrices A, B, C, and D depends only on the results of a modal solution.

3.4.2 Modal Method

A modal model is constructed from the results of the generalized eigenvalue problem

$$[K - \omega^2 M]q = 0. \tag{3.77}$$

Solving for ω^2 yields a diagonal eigenvalue matrix Ω^2 and an eigenvector matrix Φ which can be mass normalized so that

$$\Phi^T M \Phi = I \tag{3.78}$$

$$\Phi^T K \Phi = \Omega^2, \tag{3.79}$$

where the columns of Φ are the eigenvectors ϕ_i. Then through a change of variables

$$q = \Phi\eta \tag{3.80}$$

Equation 3.68 can be transformed to

$$\Phi^T M \Phi\ddot{\eta} + \Phi^T C_{\text{D}} \Phi\dot{\eta} + \Phi^T K \Phi\eta = \Phi^T F u, \tag{3.81}$$

Assuming modal damping, though not necessarily equal damping in each mode

$$\ddot{\eta} + 2Z\Omega\dot{\eta} + \Omega^2\eta = \Phi^T F u, \tag{3.82}$$

where Z is the diagonal matrix of damping ratios. The output variables are similarly transformed so that

$$y' = S_p \Phi\eta + S_v \Phi\dot{\eta}. \tag{3.83}$$

This system can be placed in first order form (Equation 3.72) by considering the new states to be

$$x = \begin{bmatrix} \eta \\ \dot{\eta} \end{bmatrix}. \tag{3.84}$$

Then

$$A = \begin{bmatrix} 0 & I \\ -\Omega^2 & -2Z\Omega \end{bmatrix} \tag{3.85}$$

$$B = \begin{bmatrix} 0 \\ \Phi^T F \end{bmatrix} \tag{3.86}$$

$$C = \begin{bmatrix} S_p\Phi & S_v\Phi \end{bmatrix} \tag{3.87}$$

$$D = 0. \tag{3.88}$$

The advantage of the modal model is that it is easier to reduce the dimension of the model to include only the dynamic modes that are important to the control. Thus if the model has a large number of degrees of freedom in order to get low frequency modes accurately, the high frequency modes can be truncated from the model resulting in an accurate model over a finite bandwidth. Partitioning the eigenvector matrix

$$\Phi = \begin{bmatrix} \Phi_K & \Phi_T \end{bmatrix} \tag{3.89}$$

where $()_K$ indicates terms kept, and $()_T$ indicates terms truncated, then the system matrices become

$$A = \begin{bmatrix} 0 & I \\ -\Omega_K^2 & -2Z_K\Omega_K \end{bmatrix} \tag{3.90}$$

$$B = \begin{bmatrix} 0 \\ \Phi_K^T F \end{bmatrix} \tag{3.91}$$

$$C = \begin{bmatrix} S_p\Phi_K & S_v\Phi_K \end{bmatrix}. \tag{3.92}$$

In order to get the static gain of the system correctly, *i.e.*, to include the static effect of all the truncated modes, a static correction[26] should be applied. This is done by solving for static deformations

$$\Phi_S = K^{-1}F. \tag{3.93}$$

Then the static gain can be corrected by adding the D term

$$D = S_p(\Phi_S - \Phi_K(\Phi_K^T M\Phi_S)). \tag{3.94}$$

3.4.3 Direct Method Applied to Circulant Systems

For structural systems that exhibit circulance, either or both of these methods can be used to derive the model of the system dynamics. To apply the direct method, the degrees of freedom of the system must be arranged so that M, K, C_{D}, F, S_p and S_v are block circulant (Equation 3.31). Then the transformation T can be applied to Eqs. 3.68 and 3.69 to get

$$\overline{M}\ddot{\overline{x}} + \overline{C_{\mathrm{D}}}\dot{\overline{x}} + \overline{K}\overline{x} = \overline{F}\overline{u}, \tag{3.95}$$

and

$$\overline{y} = \overline{S_p}\overline{x} + \overline{S_v}\dot{\overline{x}}. \tag{3.96}$$

Where the second order ODE now decouples into n_b smaller ODEs.

These second order ODEs can be converted to the first order forms as in Section 3.4.1 to obtain n_b decoupled systems represented by matrices

$$A_i = \begin{bmatrix} 0 & I \\ -\overline{M_i}^{-1}\overline{K_i} & -\overline{M_i}^{-1}\overline{C_{\mathrm{D}i}} \end{bmatrix} \tag{3.97}$$

$$B_i = \begin{bmatrix} 0 \\ \overline{M_i}^{-1}\overline{F_i} \end{bmatrix} \tag{3.98}$$

$$C_i = \begin{bmatrix} \overline{S_{p_i}} & \overline{S_{vi}} \end{bmatrix} \tag{3.99}$$

$$D_i = 0 \tag{3.100}$$

for $i = 0, \ldots, n_b - 1$.

As with the fully coupled system equations, the dimension of these system matrices may be excessively large, and a modal approach can be taken.

3.4.4 A Hybrid Method Applied to Circulant Systems

Once the second order ODEs are decoupled, a modal method for converting to first order form as in Section 3.4.2 can be applied to each independently. Then the system matrices for each of the n_b decoupled systems are represented by

$$A_i = \begin{bmatrix} 0 & I \\ -\Omega_i^2 & -2Z_i\Omega_i \end{bmatrix} \tag{3.101}$$

$$B_i = \begin{bmatrix} 0 \\ \Phi_i^T \overline{F}_i \end{bmatrix} \tag{3.102}$$

$$C_i = \begin{bmatrix} \overline{S_{p_i}}\Phi_i & \overline{S_{v_i}}\Phi_i \end{bmatrix} \tag{3.103}$$

$$D_i = 0, \tag{3.104}$$

where Φ_i and Ω_i^2 are the eigenvector and eigenvalue matrices of the i^{th} generalized eigenvalue problem

$$[\overline{K}_i - \omega^2 \overline{M}_i]\overline{x}_i = 0 \tag{3.105}$$

for $i = 0, \ldots, n_b - 1$. Note that in converting to the modal form a state transformation has occurred

$$\begin{bmatrix} \overline{x} \\ \dot{\overline{x}} \end{bmatrix} = \begin{bmatrix} \Phi_i & 0 \\ 0 & \Phi_i \end{bmatrix} \begin{bmatrix} \eta \\ \dot{\eta} \end{bmatrix}. \tag{3.106}$$

This means that the η_is are no longer related by a discrete Fourier transform to the η of the full coupled system. In fact, since both η_i and η represent modal states, the η_is comprise η. There is a very specific ordering however. Because the transformation to the circulant matrices produced independent blocks, it has grouped certain eigenvalues together. These are eigenvalues whose eigenvectors have a spatial frequency corresponding to the frequency of the block. With the modal degrees of freedom in η so arranged, stacking the η_is results in the vector η without any further transformation required.

Thus, the properties of circulant systems have been used to decouple the input/output nature of the problem, but the states have been transformed to modal degrees of freedom. This allows some model reduction to be done independently in the decoupled problems. As in Section 3.4.2, unimportant modes can be truncated so that the system dynamics are now represented by

$$A_i = \begin{bmatrix} 0 & I \\ -\Omega_{i_K}^2 & -2Z_{i_K}\Omega_{i_K} \end{bmatrix} \tag{3.107}$$

$$B_i = \begin{bmatrix} 0 \\ \Phi_{i_K}^T \overline{F}_i \end{bmatrix} \tag{3.108}$$

$$C_i = \begin{bmatrix} \overline{S_p}\Phi_{i_K} & \overline{S_{v_i}}\Phi_{i_K} \end{bmatrix} \tag{3.109}$$

$$D_i = \overline{S_{p_i}}(\Phi_{i\mathrm{S}} - \Phi_{i\mathrm{K}}(\Phi_{i\mathrm{K}}^T \overline{M}_i \Phi_{i\mathrm{S}})), \tag{3.110}$$

where

$$\Phi_{i\mathrm{S}} = \overline{K}_i^{-1} \overline{F}_i. \tag{3.111}$$

Note also that each of the n_b decoupled systems can be truncated to different degrees, thus the number of states in each of the subsystems is not necessarily the same. It is also no longer possible to recreate the states x of the original full order system. However, it should be emphasized that the circulant input/output behavior of the system has been maintained though the internal states have not.

3.4.5 Modal Method Applied to Circulant Systems

The hybrid approach resulted in n_b decoupled input/output systems whose internal states are the modal states of the fully coupled system. It should therefore be possible to create the decoupled systems from a purely modal model of the full system, without having to do the circulant transformation of the mass and stiffness matrices of the full system.

The hybrid approach transformed Equation 3.68 twice to yield

$$\Psi^T T^T M T \Psi \ddot{\eta} + \Psi^T T^T C_{\mathrm{D}} T \Psi \dot{\eta} + \Psi^T T^T K T \Psi \eta = \Psi^T T^T F T T^T u = \Psi^T T^T F u, \tag{3.112}$$

where Ψ is the block diagonal matrix composed of the eigenvectors from the subproblems in the hybrid approach Φ_i, and η is the vector composed of the η_is of the subproblems stacked below one another.

Comparing Equation 3.112 with Equation 3.81, it is clear that the combination of these two transformations is simply the eigenvector matrix of the full order problem

$$\Phi = T\Psi, \tag{3.113}$$

albeit with the very specific ordering of the eigenvectors and eigenvalues discussed in the previous section.

Thus a purely modal approach to system modelling can begin with the A, B, C and D matrices in Equations 3.90, 3.91, 3.92 and 3.94. It is now necessary only to

perform the circulant transformation on the inputs and outputs of the system

$$\overline{u} = T^T_{\frac{n_u}{N}} u \tag{3.114}$$

$$\overline{y} = T^T_{\frac{n_y}{N}} y, \tag{3.115}$$

to decouple the B, C and D matrices into the appropriate blocks.

Note that it is not necessary to reorder the eigenvectors and eigenvalues before the input and output transformations are applied. Thus it is not necessary to know which eigenvectors correspond to which circulant block. Applying the input and output transformations to the matrices in Equations 3.91, 3.92 and 3.94, results in B, C and D matrices that are sparse. The necessary reordering of degrees of freedom to form block diagonal matrices B, C and D becomes obvious and results in subsystems that are identical to those derived via the hybrid approach, Equations 3.107-3.110.

3.4.6 Modelling Summary

The three approaches to modelling a circulant system listed in Sections 3.4.3, 3.4.4, and 3.4.5 are summarized in Figure 3-3. The figure shows three streams leading from a mass and stiffness matrix representation to a state space (A, B, C, D) representation. In the direct approach from Section 3.4.3, the leftmost stream, and in the hybrid approach from Section 3.4.4, the center stream, the circulant mass and stiffness matrices are transformed to produce decoupled mass and stiffness matrices, $\overline{M}$ and $\overline{K}$, as shown by the transformation T. These two approaches are then distinguished by a modal solution. The direct approach goes directly to decoupled state space A, B, C, and D matrices whereas the hybrid approach applies a modal solution to the decoupled mass and stiffness matrices. It then builds the state space system from the modal solution.

By contrast, the purely modal approach of Section 3.4.5, represented by the rightmost stream applies the decoupling transformation, T, only to the inputs and outputs of the system after a full modal solution has been obtained. The benefit of this approach is that it allows one to create a decoupled model directly from the modeshapes and frequencies output from a finite element package.

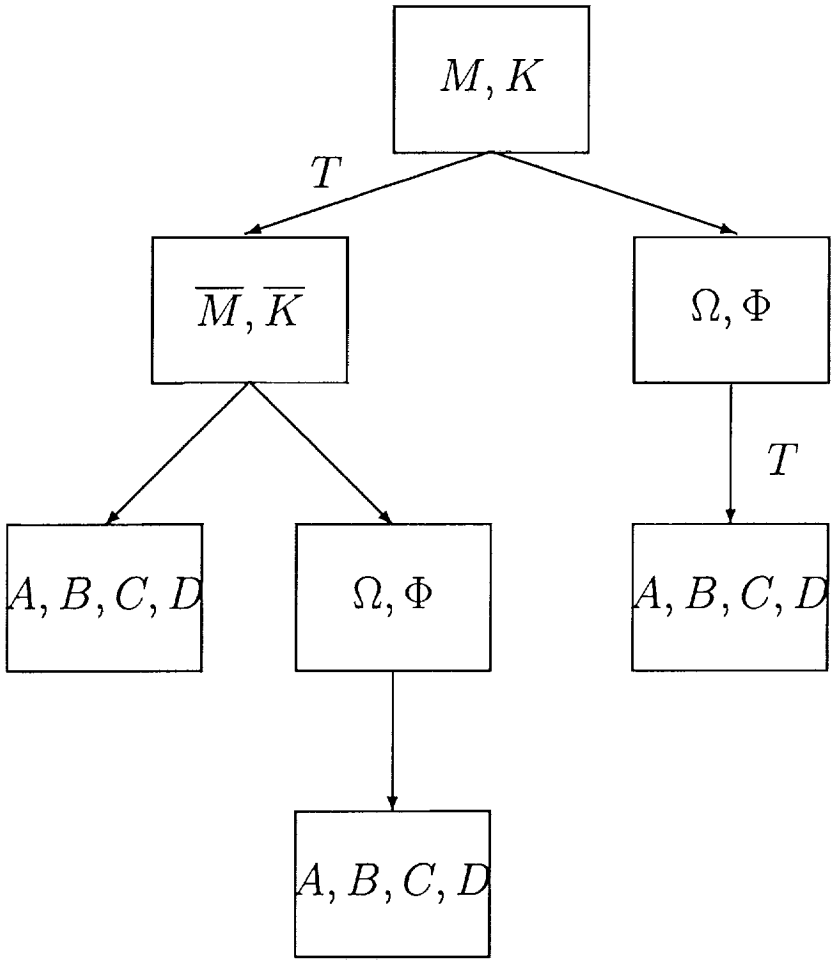

Figure 3-3: Summary of the modelling approaches for circulant systems.

Chapter 4

Modelling

This chapter discusses the modelling of the adaptive secondary mirror system for control design purposes. This modelling process consists mainly of two parts. The first is structural modelling, the second is atmospheric distortion modelling. In the preceding chapter, the standard state space form of the system model

$$\begin{aligned} \dot{x} &= Ax + B_w w + B_u u \\ z &= C_z x + D_{zw} w + D_{zu} u \\ y &= C_y x + D_{yw} w + D_{yu} u \,, \end{aligned} \tag{4.1}$$

was presented. In this form, the vector x contains the states of the system, w contains the disturbance inputs, u contains the control inputs, y contains measurement outputs for control, and z contains all the performance outputs of the system including both state and control effort terms in a control formulation.

For the control design model, the disturbance inputs w are inputs to a model of atmospheric distortion that is presented in Section 4.2. The control inputs u are a set of 270 voice coil actuators, and are discussed in Section 4.1.1. Measurement outputs y consist of 126 wavefront sensors and 270 gap sensors which measure the displacement of the deformable mirror. The performance outputs z are the optical pathlength difference (OPD) for starlight reflecting from various points on the secondary mirror of the MMT. All of these outputs are discussed in Section 4.1.2.

4.1 Structural Modelling

The deformable secondary mirror for the Multiple Mirror Telescope (MMT) [1] is an annular hyperboloidal shell which has an outer diameter of 642 mm, inner diameter of 60 mm, and is 2.25 mm thick. The mirror is constructed from Zerodur glass which has a near zero coefficient of thermal expansion. It is supported on the inner radius by a thin (0.3mm) annular aluminum flexure, with outer diameter 60mm and inner diameter 30 mm, which is itself clamped to a central shaft which is the only means of structural support for the mirror. The center shaft is connected to a 75 mm thick aluminum backplate which has a hyperboloidal surface that follows that of the mirror with a gap of 50 μm. The mirror is deformed by voice coil actuators for which the coil is located on the backplate and the permanent magnet is bonded to the non-reflecting concave surface of the mirror. This back surface of the mirror is also aluminized to provide a conducting surface which is used as part of a set of capacitive sensors to measure the gap distance. A schematic drawing of the deformable secondary mirror is shown in Figure 4-1. The reflecting surface of the mirror is convex since it is the secondary mirror, and faces down. The central shaft is shown as the cross-hatched area, and the clamping of the aluminum flexure can be seen close to the central axis. The backplate is shown with two actuators attached. Channels are cut in the backplate through which the actuator mechanisms are placed. None of this portion of the actuator contacts the mirror surface. Forces are applied to the magnet attached to the concave surface of the mirror.

The shape of the deformable secondary mirror satisfies the conic equation

$$r^2 - 2Rz + (1 + K)z^2 = 0 \tag{4.2}$$

where r is the radial distance of a point from the axis normal to the center of the mirror, z is the height above the origin, R is the radius of curvature of the surface at the origin, and K is the conic constant. Note that by convention, positive R defines a concave surface and negative R defines a convex surface. The conic constant K

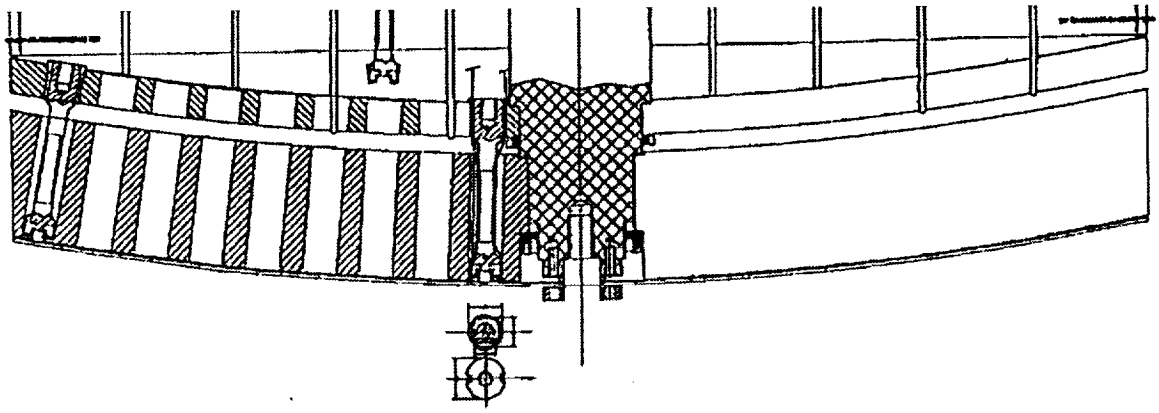

Figure 4-1: Schematic drawing of deformable mirror, backplate and support.

Table 4.1: Geometric properties of the deformable secondary mirror

Property	Value
Inner Diameter (Aluminum)	30 mm
Inner Diameter (Zerodur)	60 mm
Outer Diameter (Zerodur)	642 mm
Thickness	2.25 mm
Radius of Curvature (R)	-1783.496 mm
Conic Constant (K)	-1.406165

defines four different shapes

$$\begin{array}{ll} K = 0 & \text{spherical} \\ 0 > K > -1 & \text{ellipsoidal} \\ K = -1 & \text{paraboloidal} \\ K < -1 & \text{hyperboloidal} \end{array} \tag{4.3}$$

The radius of curvature and conic constant are listed along with other geometric properties of the mirror in Table 4.1. The mirror shape is shown in oblique view in Figure 4-2 without the backplane. With the given values of R and K, the height of the edge of the mirror is 25.4 mm greater than at the center. The degree of curvature that this represents can be seen clearly in Figure 4-1 recalling that the diameter of the mirror is more than half a meter.

A finite element model (FEM) of the hyperbolic adaptive secondary mirror was made in MSC/NASTRAN™. The model contains 984 CQUAD4 and 192 CTRIA3

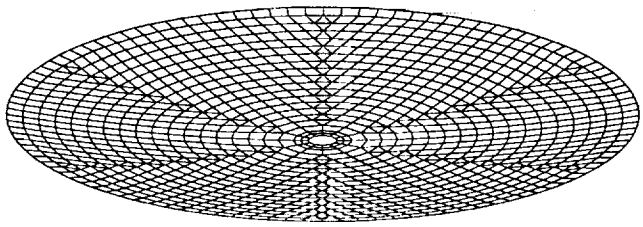

Figure 4-2: Oblique view of deformable secondary mirror.

Table 4.2: Material properties for components of the secondary mirror

Material	Young's Modulus (N/m^2)	Poisson's Ratio	Density (kg/m^3)
Zerodur	70×10^9	0.22	2100
Aluminum	75×10^9	0.30	2770

isoparametric elements for modelling the glass, and 24 CQUAD4 isoparametric elements to model the aluminum flexure. The backplate is not modelled. The inner diameter of the flexure is constrained in all directions to represent the clamped boundary conditions that exist. In addition, concentrated masses and inertias were placed at each actuator location to account for the mass and inertia of the 1.5 g - 6.35 mm cubic permanent magnets attached to the glass at these locations. The model has a total of 6984 degrees of freedom. Table 4.2 lists the properties of the materials that were used to model the glass and aluminum components of the model.

Figure 4-3 shows the layout of gridpoints and elements in the model. The inner two rings of elements represent the aluminum flexure while the remaining elements compose the Zerodur glass deformable mirror surface. The large number of gridpoints is dictated by the geometry of the actuators and sensors. There are 126 optical wavefront sensors which measure the distortion of incoming light. These are oriented in six annular rings of different radii and cover the full surface of the mirror. There are

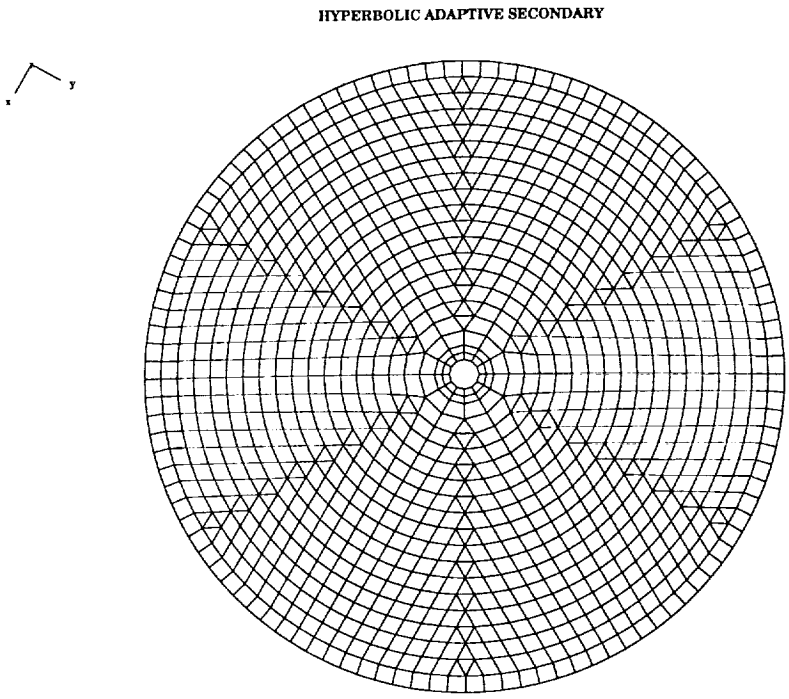

Figure 4-3: Top view of Finite Element Model (FEM) grid point and element locations.

270 actuators with collocated gap sensors positioned in 9 rings. For commensurability, 18 rings of elements (19 rings of nodes) are required in the glass. The layout of these actuators and sensors, to be discussed subsequently, requires an increasing number of grid points in each ring. Thus, the number of grid points in each ring is not commensurate, and a regular grid point spacing is not possible. The triangular elements allow the increase in number of grid points as the radius of the annulus increases resulting in the element layout shown in Figure 4-3.

The modal structure of the model is characterized by three groups of modes; radial modes, circumferential modes, and higher frequency modes that are both radial and circumferential. These mode types are identified by the number of node lines in the radial and circumferential directions. Figure 4-4 compares the [2-θ] modeshape (31.3 Hz) for the mirror with the undeformed mirror. Circumferentially following the outer edge of the mirror, there are two peaks and two valleys in the mode shape. Between each of these are node lines on which no displacement of the mirror oc-

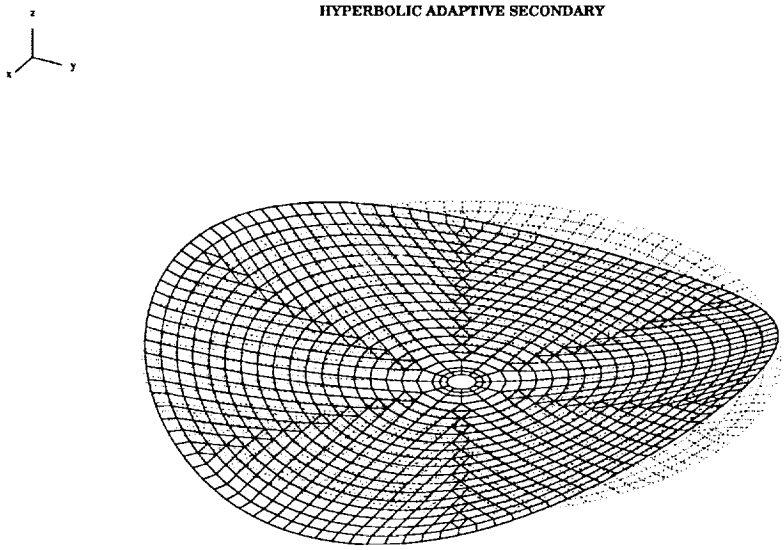

Figure 4-4: Mode shape for [2-θ] mode (31.3 Hz).

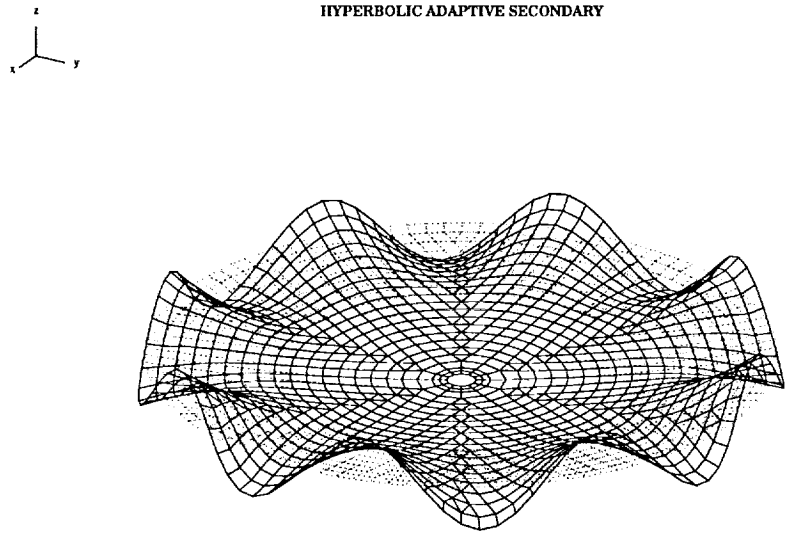

Figure 4-5: Mode shape for [8-θ] mode (458.3 Hz).

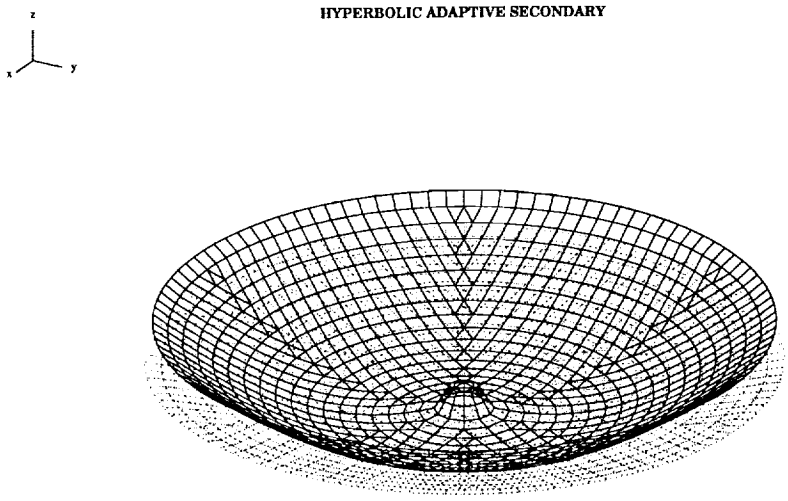

Figure 4-6: Mode shape for first mirror radial mode [1-r] (460.2 Hz). Note that there is a second node line which involves the annular flexure.

curs. Similarly, Figure 4-5 shows the [8-θ] mode (458.3 Hz) which distinctly shows 8 peaks and valleys circumferentially. All circumferential modes appear in pairs. The modeshapes for these two circumferential modes are identical only rotated by $\pi/2N$ radians, with N being the number of circumferential peaks. The mode shapes are not unique since it is only a relative difference of $\pi/2N$ radians that distinguishes the modes. Both of these modes must be included in any dynamic model of the structure.

Purely radial modeshapes vary only as a function of radial distance from the center of the mirror. These modeshapes are unique, not appearing in pairs as do the circumferential modes. Figure 4-6 shows the deformed shape of the first radial [1-r] modeshape (460.2 Hz). This is in fact the second radial mode since there are two node lines, however one of these is at the root of the flexure. This is the first radial mode that has significant bending in the glass, and the radial modes are numbered as such. Because of the hyperbolic shape of the mirror, a considerable amount of shell stiffening has been added. For a flat plate with equivalent dimensions, the first radial mode occurs at 40 Hz rather than 460 Hz. As a result, most of the structural modes in the frequency range that is important to the control are circumferential modes, and the modal density in this frequency range is slightly lower than it would be for a

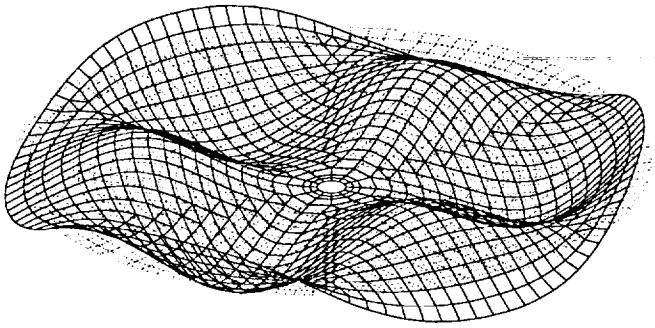

Figure 4-7: Mode shape for [3-θ, 1-r] mode (533.9 Hz).

flat mirror.

At frequencies above the first radial mode, the third type of mode shape starts to occur. These are modes that have both radial and circumferential node lines. Figure 4-7 shows an example of these with the [3-θ,1-r] mode (533.9 Hz). Because these modes have a circumferential component, they again occur in repeated pairs with non-unique eigenvectors.

The first 55 natural frequencies of the FEM, up to a frequency of 1 kHz, are listed in Table 4.3. The table includes the characterization of modes into radial, circumferential, and circumferential-radial modes; the number of circumferential and radial node lines; the uniqueness of modeshapes through listing of the number of repeated modes; and finally a categorization into one of four groups (0, 1, 2 ,3) representing to which circulant block each mode belongs.

Note that the tilt, piston, and torsion modes are singled out in the table. These are all pseudo-rigid body modes. Were the flexure not present, and the mirror unconstrained, these would be rigid body modes. Because the flexure has very low transverse stiffness, most of the strain energy of these modes occurs in the flexure. The remaining two translational rigid body modes are highly stiffened by the in-plane stiffness of the mirror and flexure. These modes have a frequency greater than 1 kHz.

Table 4.3: Natural frequencies of the deformable mirror up to 1 kHz.

Freq. (Hz)	Node Lines (θ,r)	Type	Number	Group (j)
7.0	(1,0)	Circumferential (Tilt)	2	1
31.3	(2,0)	Circumferential	2	2
32.2	(0,0)	Radial (Piston)	1	0
72.5	(3,0)	Circumferential	2	3
89.7	(0,0)	Torsion	1	0
126.6	(4,0)	Circumferential	2	2
192.3	(5,0)	Circumferential	2	1
269.1	(6,0)	Circumferential	2	0
358.0	(7,0)	Circumferential	2	1
458.3	(8,0)	Circumferential	2	2
460.2	(0,1)	Radial	1	0
464.8	(1,1)	Circumferential-Radial	2	1
481.7	(2,1)	Circumferential-Radial	2	2
520.4	(0,2)	Radial	1	0
533.9	(3,1)	Circumferential-Radial	2	3
554.7	(1,2)	Circumferential-Radial	2	1
570.1	(9,0)	Circumferential	2	3
599.1	(4,1)	Circumferential-Radial	2	2
628.6	(2,2)	Circumferential-Radial	2	2
686.4	(5,1)	Circumferential-Radial	2	1
686.7	(0,3)	Radial	1	0
695.7	(10,0)	Circumferential	2	2
749.4	(3,2)	Circumferential-Radial	2	3
775.2	(1,3)	Circumferential-Radial	2	1
795.2	(6,1)	Circumferential-Radial	2	0
833.4	(11,0)	Circumferential	2	1
881.2	(4,2)	Circumferential-Radial	2	2
924.8	(2,3)	Circumferential-Radial	2	2
926.6	(7,1)	Circumferential-Radial	2	1
983.4	(12,0)	Circumferential	2	0

Note that the torsion mode is neither radial nor circumferential in character as there are no node lines.

Both of the methods described in Section 3.4 were used to develop state space models of the mirror dynamics from the FEM results. When using the modal method of Section 3.4.5, an important factor in modelling is determining to which circulant group, *i.e.*, what spatial frequency, each of the modes belongs. This is quite straight-

forward and can be achieved by looking at the modeshapes. The spatial frequency is directly related to the number of circumferential node lines. As will be described in subsequent sections, this system has actuator and sensor layouts that result in a circulant system of order six ($N = 6$). Thus for a complex-valued representation of the system, the modes can be arranged into six groups (0-5). All modes in group i satisfy

$$i = \theta \mathrm{mod} N \tag{4.4}$$

where θ is the number of circumferential node lines in the mode shape. Since groups i and $N-i$ are combined in the real-valued representation, four groups (j), result when $N = 6$. The first group ($j = 0$) contains those modes for with $i = 0$. In the second ($j = 1$) group, $i = 1, 5$; in the third ($j = 2$), $i = 2, 4$; and in the fourth ($j = 3$), $i = 3$. Table 4.3 shows to which group each of the modes belongs. This division results in the decoupling of system models that was presented in Section 3.4.5.

This mode shape identification was relatively easy for the modes in the model up to 1 kHz which, fortunately, is the range of interest for this model. For modes at higher frequency ranges it was not always as easy to determine the number of circumferential node lines. However, while this step makes identification of the groups easy, it is not strictly necessary. Simply multiplying the modeshape matrix for the selected actuators by the transformation T from Equation 3.22 of the appropriate dimensions results in a decoupling of the mode shape matrix which then makes it easy to arrange the modes into the correct groups.

To complete the dynamic modelling of the mirror, several static runs were made to calculate the static correction terms shows in Section 3.4.2. Finally, modal damping of 1% in the structure was assumed. This damping level is considered high for glass, but there is additional damping provided by the constrained motion of air in the 50 micron gap between the glass surface and the reference surface behind the glass, and damping added by the voice coil actuators. Until measured values for the mirror are available, this value will be used.

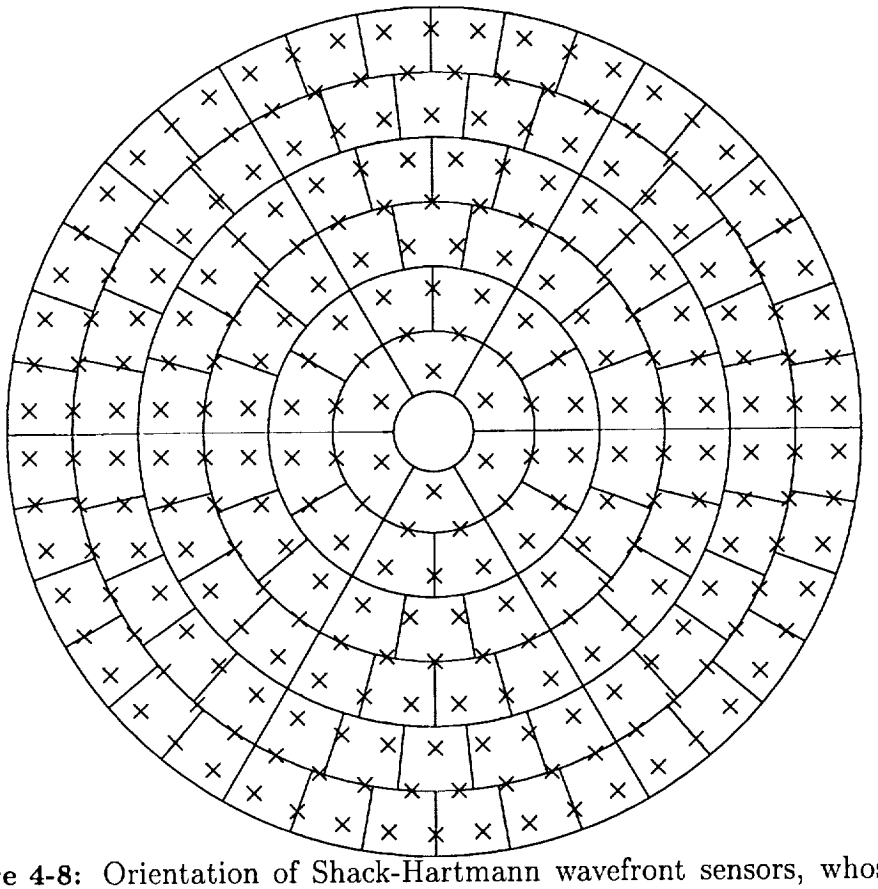

Figure 4-8: Orientation of Shack-Hartmann wavefront sensors, whose subapertures are shown by regions enclosed by the solid lines, and orientation of collocated voice coil actuators and capacitive displacement sensors (x) on the deformable mirror.

4.1.1 Actuators

The mirror is deformed through forces applied by voice coil actuators arranged in 9 rings of 6, 12, 18, 24, 30, 36, 42, 48, and 54 actuators shown in Figure 4-8. This arrangement has six identical sectors which enables the circulant transformations of Chapter 3 to be performed. The forces applied at each of these locations are normal to the surface. The FEM contains a grid point at each of the actuator locations, so finding the modal influence of an actuator is simply a matter of transforming the modeshapes from the Cartesian coordinates of the FEM to the directions aligned with the actuators.

The shape of the mirror was determined from Equation 4.2. The normal direction

is simply the direction of the gradient. Rewriting Equation 4.2 in terms of Cartesian coordinates yields,

$$f(x,y,z) = x^2 + y^2 - 2Rz + (1+K)z^2 = 0. \tag{4.5}$$

From this the gradient can be calculated,

$$\nabla f = \frac{1}{\sqrt{4(x^2+y^2) + ((1+K)z - 2R)^2}} \begin{bmatrix} 2x \\ 2y \\ (1+K)z - 2R \end{bmatrix}. \tag{4.6}$$

The modeshape in the normal direction for the j^{th} actuator and i^{th} mode (${}_j\phi_{i_N}$) is

$${}_j\phi_{i_N} = {}_j\phi_i^T \nabla f, \tag{4.7}$$

where ${}_j\phi_i = \begin{bmatrix} {}^x_j\phi_i & {}^y_j\phi_i & {}^z_j\phi_i \end{bmatrix}^T$ is the modeshape of an actuator location j for the i^{th} mode of the system in Cartesian coordinates x, y, and z.

4.1.2 Sensors

Two different types of feedback sensors exist in the MMT system. The first is a set of capacitive displacement sensors. These sensors measure the capacitance of the air gap between the mirror and the backplate. The capacitance is proportional to the distance between the mirror and the backplate. Thus, these provide a measure of the displacement of the mirror relative to the backplate in the direction normal to the surface at each location and are thus collinear with the actuator directions. There are 270 of these sensors each collocated with one of the voice coil actuators. Thus, the mode shapes for these sensors are identical to those of the actuators in the previous section.

The performance of this system will be evaluated at 546 locations across the surface of the mirror. At each of these the wavefront error, *i.e.,* the difference between the displacement of the mirror and the wavefront displacement, which is presented in the following section, is calculated. To incorporate the structural component of this error, the displacement of the mirror, a set of performance pseudo-sensors that measures displacement is required. The term pseudo-sensor is used because these sensors

do not actually exist, but are modelled to provide the model with a performance both to optimize in control design and to evaluate in terms of performance. These sensors are modelled in the same way as the capacitive displacement feedback sensors, the only difference being that the locations on the mirror are different. Figure 4-8 shows the orientation of feedback sensors relative to the wavefront sensors which cover the full area of the mirror. These sensors are collocated with the voice coil actuators. Figure 4-9 shows the orientation of performance locations relative to the wavefront sensors. More performance locations than wavefront sensors are used in order to evaluate the wavefront error between sensors. This allows for calculation of the 'waffle' effect which results in greater residual pathlength error between sensed and actuated locations on the mirror. Note that the performance locations and wavefront sensors purposely divide the mirror surface into six identical sectors. This partition also enables the circulant transformations of Chapter 3 to be made.

The second type of feedback sensor is a set of 126 Shack-Hartmann wavefront sensors arranged in 6 rings consisting of 6, 12, 18, 24, 30, and 36 wavefront sensors, shown in Figs. 4-8 and 4-9. These wavefront sensors measure the slope in two directions of the wavefront error defined earlier as the difference between the wavefront displacement and the mirror displacement. The Shack-Hartmann sensor [12] focuses the incoming light of a portion of the mirror termed the subaperture on the center of a quad cell array of a CCD. The slope of the wavefront error is proportional to the centroid of the intensity in the quad cell. Note that this provides a measure of the difference between the mirror shape and the distorted wavefront that is spatially averaged over the area of the subaperture and temporally averaged over the integration time of the CCD. These two effects, averaging in both time and space must both be accounted for in a model of the sensor.

First, time averaging will be considered. Consider a signal $r(t)$. The average value of this signal over the time interval $t_0 - T < t < t_0$ indexed with the final time is given by

$$\overline{r}(t_0) = \frac{1}{T}\int_{t_0-T}^{t_0} r(\tau)\mathrm{d}\tau. \tag{4.8}$$

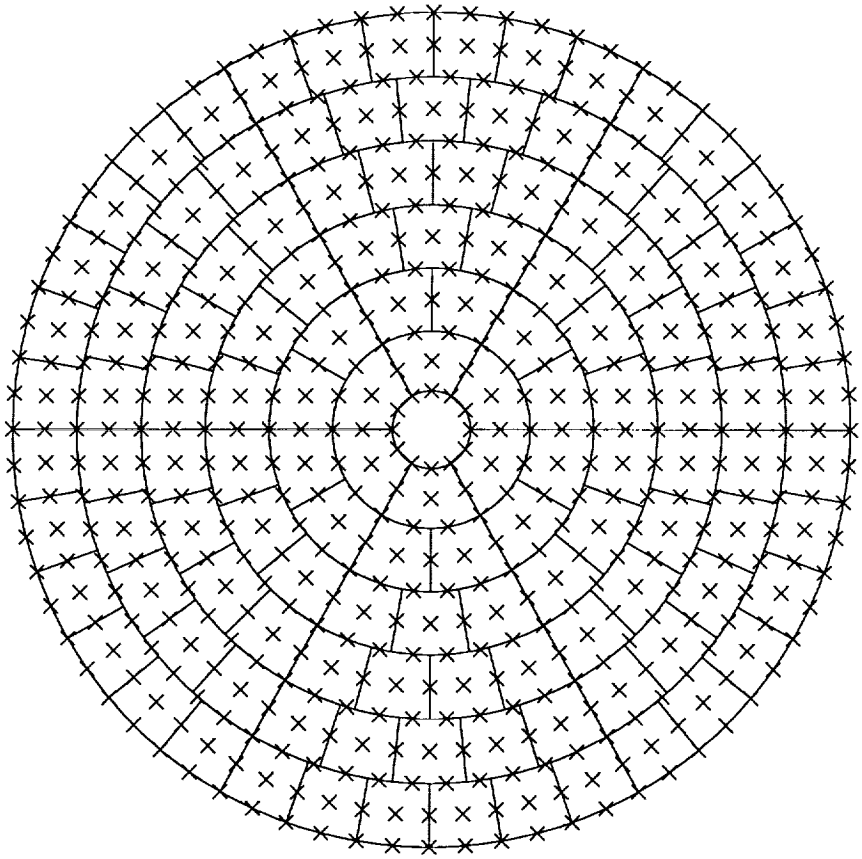

Figure 4-9: Orientation of Shack-Hartmann wavefront sensors and performance locations (x) on the deformable mirror.

This is equivalent to a convolution of $r(t)$ with the averaging operator $h(t)$

$$\overline{r}(t) = \int_{-\infty}^{\infty} h(t-\tau)r(\tau)\mathrm{d}\tau, \tag{4.9}$$

where

$$h(t) = \begin{cases} 0 & t < 0, t > T \\ \frac{1}{T} & 0 \leq t \leq T \end{cases} \tag{4.10}$$

Taking Laplace transforms of both sides converts the convolution to multiplication.

$$\overline{r}(s) = h(s)r(s), \tag{4.11}$$

so that there is a direct relation between the frequency domain representation of the signal r and its average value over the previous time interval T, $\overline{r}$.

The Laplace transform, $h(s)$, can be derived by looking at the impulse response $h(t)$ plotted in Figure 4-10. This impulse response is simply a scaled version of a unit

step $u_0(t)$ followed after an interval T by a negative step.

$$h(t) = \frac{1}{T}(u_0(t) - u_0(t-T)) \tag{4.12}$$

where

$$u_0(t) = \begin{cases} 0 & t < 0 \\ 1 & 0 \leq t \end{cases}. \tag{4.13}$$

Calculating the Laplace transform gives

$$\begin{aligned} h(s) &= \mathcal{L}\{h(t)\} && (4.14) \\ &= \frac{1}{T}\int_0^\infty [u(t) - u(t-T)]e^{-sT}dt && (4.15) \\ &= \frac{1 - e^{-sT}}{sT}. && (4.16) \end{aligned}$$

This is the same as the response of a zero-order hold [27] except for a scaling of $\frac{1}{T}$. Just like the zero-order hold, the effect is to introduce a time delay of length $\frac{T}{2}$, and to filter the magnitude of the signal by $|\ \mathrm{sinc}(\frac{sT}{2})\ |$. The frequency response of h

$$h(\jmath\omega) = e^{-\frac{\jmath\omega T}{2}}\mathrm{sinc}(\frac{\omega T}{2}) \tag{4.17}$$

is shown in Figure 4-11. The magnitude effect is fairly small up to the frequency $\omega T = \pi$. If T for the averaging operator is equal to the sample rate for the system, *i.e.,* a full sample period is integrated, $\omega T = \pi$ is the Nyquist frequency for the system. In such cases, the change in magnitude is negligible over the frequency range of interest in the problem, and the time delay can be added to the system through a Padé approximation [28] as would normally be done for a zero-order hold itself. If the averaging is calculated over larger time periods, the magnitude effects can be significant as has been shown in an example by Smith [29].

Spatial averaging is considerably more complicated particularly when the structure is more than one dimensional. A considerable amount of work has been done on 1-D structures [30, 31] to determine shapes over which to average signals to obtain certain system properties. The shape of the wavefront sensors, however, is already determined. The objective in this work is to get an accurate representation of the response of the system measured by the wavefront sensors.

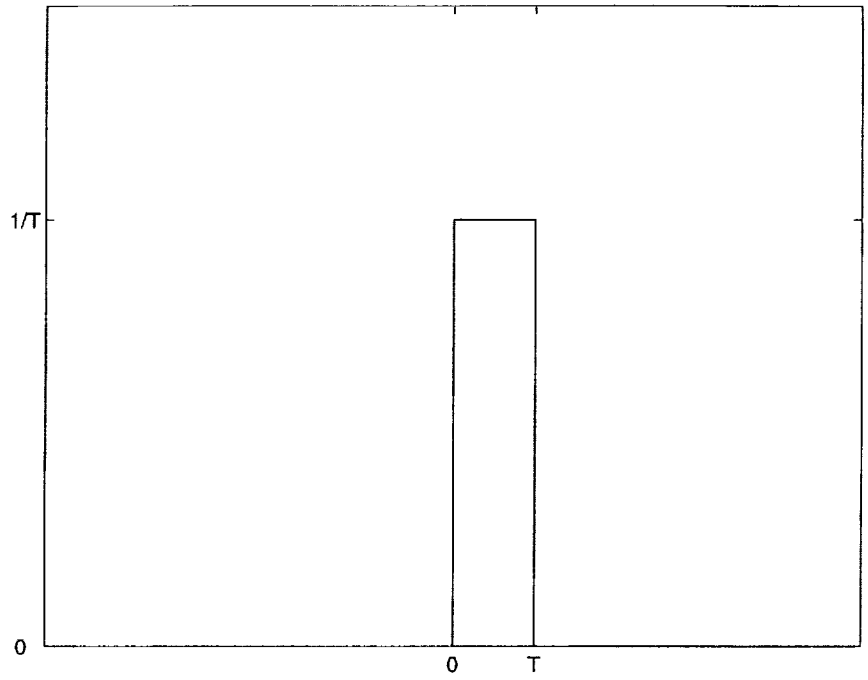

Figure 4-10: Impulse response $h(t)$ of the averaging operator.

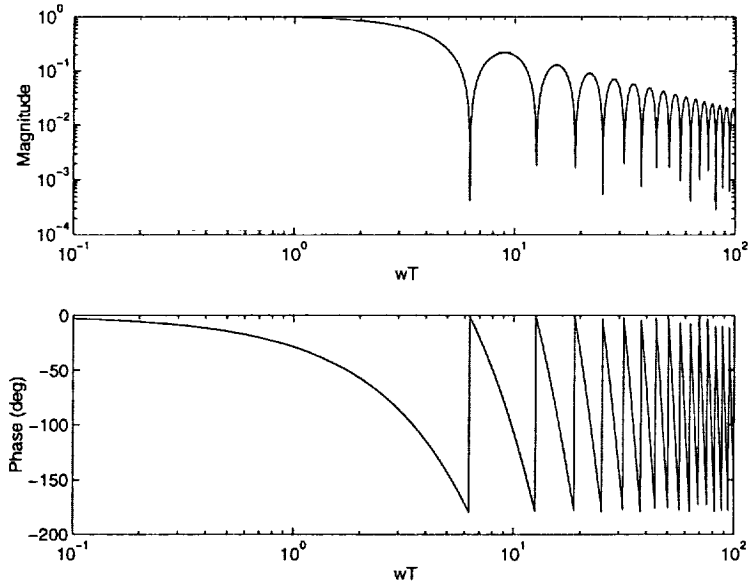

Figure 4-11: Frequency response, $h(j\omega)$, magnitude plot shows little magnitude change up to 'Nyquist' frequency $\omega T = \pi$. Phase plot shows significant phase loss.

The wavefront sensor measures average slope in two directions across the area of the subaperture. On a modal basis, this means that the modeshapes for the two slope measurements provided by the j^{th} wavefront sensor (${}^{x}_{j}\phi_{\text{WFS}}$ and ${}^{y}_{j}\phi_{\text{WFS}}$) are given by

$$ {}^{x}_{j}\phi_{\text{WFS}} = \frac{1}{A_{S_j}} \int\int_{S_j} \frac{\partial \phi_{\text{N}}(x,y)}{\partial x} \mathrm{d}x\mathrm{d}y \tag{4.18} $$

$$ {}^{y}_{j}\phi_{\text{WFS}} = \frac{1}{A_{S_j}} \int\int_{S_j} \frac{\partial \phi_{\text{N}}(x,y)}{\partial y} \mathrm{d}x\mathrm{d}y \tag{4.19} $$

where S_j is the j^{th} subaperture for the wavefront sensor, A_{S_j} is the numerical value for the area of the j^{th} subaperture and $\int\int_S$ indicates the double integral over the subaperture surface, S.

However, the disturbance model that will be shown in the following section produces a displacement not a slope model of the wavefront of the incoming light. The important factor to both measure and control is the displacement of the mirror relative to the incoming wavefront. Thus a conversion from slope to displacement is necessary.

This is conveniently provided by Green's Theorem [32]. Green's theorem states that for a vector function

$$ F(x,y) = P(x,y)\hat{i} + Q(x,y)\hat{j} \tag{4.20} $$

where $\hat{i}$ and $\hat{j}$ are orthogonal unit vectors, and P and Q are scalar functions of the spatial variables x and y,

$$ \oint_C F(r) \cdot \mathrm{d}r = \int\int_S \left[\frac{\partial Q}{\partial x} - \frac{\partial P}{\partial y} \right] \mathrm{d}x\mathrm{d}y \tag{4.21} $$

where $r = x\hat{i} + y\hat{i}$, $\oint_C$ indicates the integral around the closed curve C and $\int\int_S$ indicates the double integral over the area S which is enclosed by C.

With $Q = \phi_{\text{N}}(x,y)$ and $P = 0$ Equation 4.21 gives

$$ \frac{1}{A_S} \oint_C \phi_{\text{N}}(x,y)\hat{i} \cdot \mathrm{d}r = \frac{1}{A_S} \int\int_S \frac{\partial \phi_{\text{N}}(x,y)}{\partial x} \mathrm{d}x\mathrm{d}y. \tag{4.22} $$

With $Q = 0$ and $P = -\phi_{\text{N}}(x,y)$,

$$ \frac{1}{A_S} \oint_C \phi_{\text{N}}(x,y)\hat{j} \cdot \mathrm{d}r = \frac{1}{A_S} \int\int_S \frac{\partial \phi_{\text{N}}(x,y)}{\partial y} \mathrm{d}x\mathrm{d}y. \tag{4.23} $$

Thus

$$ {}^{x}_{j}\phi_{\text{WFS}} = \frac{1}{A_{S_j}} \oint_{C_j} \phi_{\text{N}}(x,y)\hat{j} \cdot \mathrm{d}r \tag{4.24} $$

$$ {}^{y}_{j}\phi_{\text{WFS}} = \frac{1}{A_{S_j}} \oint_{C_j} \phi_{\text{N}}(x,y)\hat{j} \cdot \mathrm{d}r, \tag{4.25} $$

and the modeshape for the wavefront sensor measurements is now described in terms of displacement modeshapes not slopes.

We are now dealing with displacement mode shapes and one integral has been removed from the problem. It is still necessary to perform the line integral around the boundary of the subaperture. This requires evaluation of the displacement modeshapes at points other than those in the finite element model, so interpolation is required. The CQUAD4 and CTRIA3 elements are isoparametric elements [33]. Isoparametric elements use a bilinear interpolation [24] as a shape function. Thus a bilinear interpolation has been used to calculate the line integral.

The procedure for bilinear interpolation is fairly simple. A quadrilateral defined by four corner nodes is shown in Figure 4-12. The properties at a point interior to the quadrilateral can be expressed as a linear combination of the properties at the corner nodes.

$$ P = \sum_{i=1}^{4} h_i P_i \tag{4.26} $$

where P is the desired property, P_i is the value of that property evaluated at Node i, and the weighting functions h_i are

$$ h_1 = \frac{1}{4}(1+r)(1+s) \tag{4.27} $$

$$ h_2 = \frac{1}{4}(1-r)(1+s) \tag{4.28} $$

$$ h_3 = \frac{1}{4}(1-r)(1-s) \tag{4.29} $$

$$ h_4 = \frac{1}{4}(1+r)(1-s) \tag{4.30} $$

with r and s as the 'natural coordinates' [24] of the quadrilateral.

The natural coordinates, r and s, are calculated from the geometry. The two

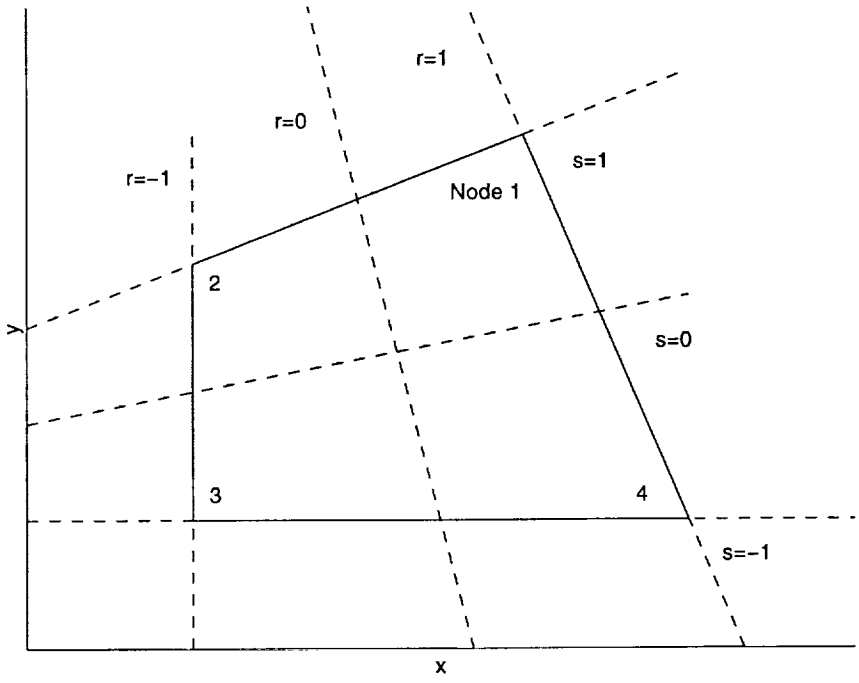

Figure 4-12: Four node quadrilateral with natural coordinate system r, s.

equations that describe the location of the desired point in the quadrilateral

$$x = \sum_{i=1}^{4} h_i x_i \tag{4.31}$$

$$y = \sum_{i=1}^{4} h_i y_i \tag{4.32}$$

can be solved to obtain the two unknown natural coordinates. These are simultaneous quadratic, not linear, equations. But if the desired point is in the interior of the element, there is a unique solution for r and s. A triangular element is a degenerate quadrilateral in which Node 4 and Node 1 are equal. The same procedure can be used to determine r and s.

From this interpolation, we now have an expression for the normal eigenvector, $\phi_N(x, y)$, anywhere on the mirror in terms of ${}_j\phi_N$, the normal eigenvectors evaluated at the performance locations shown in Figure 4-9. The integration in Equations 4.24 and 4.25 can be performed. This integration results in a matrix equation where the eigenvectors of all the wavefront sensor measurements (Φ_{WFS}) are a linear combination

of the normal eigenvectors

$$\Phi_{\text{WFS}} = W\Phi_{\text{N}} \tag{4.33}$$

where W is the transformation matrix that transforms displacements at the performance locations to wavefront sensor measurements, and Φ_{N} is the matrix of eigenvectors for the performance locations.

Thus the method for modelling the performance pseudo-sensors, the capacitive feedback sensors, and the wavefront sensors has been shown. This completes the structural modelling of the system. The modelling of the actuator inputs, and feedback sensor and performance outputs has been shown. What remains is to describe the modelling of the disturbance. The disturbance model for this system does not have a structural component. The disturbance enters the system entirely at the output and is reflected in the wavefront sensor measurements. The following section will describe the modelling of the atmosphere

4.2 Atmospheric Model

Small variations in temperature cause turbulent motion in the atmosphere. These temperature differences also change the index of refraction of the atmosphere. The accumulation of these changes in index of refraction over the path that starlight travels from the top of the atmosphere to the aperture of the telescope results in a distorted wavefront. The objective in controlling the deformable mirror is to minimize the shape difference between the distorted wavefront and the deformable mirror so that light entering the detector of the telescope is undistorted. A model of the distortion effects of the atmosphere on the distorted wavefront is the disturbance model for this system. These effects are correlated both spatially and temporally across the area of the telescope aperture.

4.2.1 Spatial Correlation

To generate the disturbance model, a von Karman spectrum [12, 34] with outer scale length $L_0 = 100$ m and coherence length $r_0 = 0.9$ m has been used. The outer scale

length is the assumed maximum size of turbulent eddies in the atmosphere. The coherence length is roughly the size of aperture above which uncorrected atmospheric distortion limits performance [12]. In this case, a larger aperture gains no better resolution because of the limits of atmospheric distortion. These match parameters used by Lloyd-Hart and McGuire [4] for the site of the MMT.

The von Karman spectrum has a phase spectrum of

$$S(\kappa) = 0.033 C_n^2 \left(\kappa^2 + \frac{4\pi^2}{L_0^2}\right)^{-\frac{11}{6}} \tag{4.34}$$

where κ is the wavenumber of the phase across the aperture, and C_n^2 is the refractive index structure constant which is a measure of the strength of atmospheric turbulence, and is a function of r_0. This spectrum gives an idea of the correlation of the distortion at different points across the aperture of the telescope. The spectrum is flat for low wavenumbers (long wavelength distortions) and rolls off at -11/3 for high wavenumbers (short wavelength distortions). The wavelength at the effective break frequency corresponds to the outer scale length, L_0.

To develop a state space model of this disturbance that can be used in control design and analysis, the covariance of samples of the atmosphere must be known. A relationship for the phase covariance of two simultaneously sampled points on the wavefront derived from the phase spectrum in Equation 4.34 is given by Roggemann *et al.* [34]

$$\mathbb{E}[\psi(x_1)\psi(x_2)] = R(\rho) = \frac{0.033\,(2\pi)^4}{\Gamma\left(\frac{11}{6}\right)} \left(\frac{0.185}{r_0}\right)^{\frac{5}{3}} \left(\frac{L_0\rho}{4\pi}\right)^{\frac{5}{6}} K_{\frac{5}{6}}(2\pi\rho/L_0) \tag{4.35}$$

where $\mathbb{E}$ denotes the expectation operator, x_1 and x_2 are vectors describing the position in the telescope aperture of two points, $\psi(x)$ denotes the phase of the wavefront at x, $K_{\frac{5}{6}}(\cdot)$ is the modified Bessel function of the second kind of order 5/6, Γ is the gamma function, and $\rho = \mid x_1 - x_2 \mid$.

The atmospheric distortion is a 2-D spatial continuum, as are the structural dynamics. For the system disturbance model, the atmospheric continuum is discretized at 546 locations across the aperture of the telescope which has a diameter of 6.5m (approximately 10 times the size of the adaptive secondary mirror). The corresponding

locations on the secondary mirror that focus light propagating normal to the aperture at the focus of the system are shown in Figure 4-9. Each of these points is treated as the location of both a disturbance input (w) and a performance output (z), as well as contributing to the wavefront sensor measurement as discussed in the previous section. The system performance is measured by the wavefront error: the accumulated error of the atmospheric distortion across the aperture minus the displacement of the mirror. For wavefront sensor measurements, a bilinear interpolation between disturbance input locations is used as it was for the mode shapes of the system.

Applying Equation 4.35 for all combinations of the 546 disturbance locations nets the 546×546 covariance matrix R. Because the disturbance locations are arranged in six identical sectors as shown in Figure 4-9, R is a block circulant matrix. Thus the disturbance and performance as well as the structural dynamics for the system are circulant. This covariance matrix describes the relationship between the phase of the wavefront at the various locations, measured at the same time. But the temporal frequency spectrum of this disturbance is not white.

4.2.2 Temporal Correlation

In addition to this spatial correlation in the phase, there is also temporal correlation. In the absence of winds, spontaneous changes to the turbulent eddies that produce the wavefront distortion would result in slowly changing distortion patterns, so-called 'boiling' of the atmosphere [35]. However, atmospheric winds carry these eddies across the aperture of the telescope. Under the 'frozen flow' hypothesis [12, 34, 36], the change in turbulent eddies, 'boiling', is negligible for the duration of time in which the eddies are blown across the telescope aperture by winds. The 'frozen flow' hypothesis thus assumes that the eddies remain unchanged. The temporal correlation of a point (x) is given by

$$\mathbb{E}[\psi(x(t_1))\psi(x(t_2))] = \mathbb{E}[\psi(x(t_1))\psi(x_2(t_1))] \tag{4.36}$$

where $x_2 = x_1 - v(t_2 - t_1)$, and v is the velocity of the wind. Thus the temporal correlation is determined from the spatial correlation. The temporal correlation of the

distortion at a given point is equal to the spatial correlation of the distortion between the given point and the points from which the wind has blown the turbulence. The resulting power spectrum for a single point with atmospheric distortion passing above it is flat at low frequencies and rolls off as $\omega^{-8/3}$ at high frequencies [12, 36]. Note that Equation 4.36 assumes a single atmospheric layer in which the turbulence propagates at a constant velocity v. More complex models can be derived which use multiple layers each with its own strength of turbulence and its own wind velocity [34, 4].

Accurately representing $\omega^{-8/3}$ as a rational transfer function requires using a large number of poles and zeros. This translates to having a large number of states in the state space representation. This is highly undesirable because this number of states must be repeated for each disturbance location.

Instead, a low order approximation is made for representing this in state space. A system with a single pole is used having a power spectrum that is flat at low frequency and rolls off as ω^{-2}. The resulting system has a shallower roll off than the actual atmosphere, and thus has more energy at high frequency than with the true spectrum. To compensate for this, the pole location was set so that the RMS output of this filter is equivalent to the correct RMS for the $\omega^{-8/3}$ spectrum of the atmosphere. The temporal structure function, $D(t)$, of this disturbance at a given location

$$D(t) = \mathbb{E}[(\psi(x(t_0)) - \psi(x(t_0 + t)))^2] \tag{4.37}$$

$$= 2\,(R(0) - R(t)) \tag{4.38}$$

is shown in Figure 4-13. This structure function was compared with the structure function generated from a multi-layer atmosphere model that appears in Ref. [4] to determine if the single pole approximation is appropriate. For large time, the magnitude is the same, indicating that the overall RMS disturbance signal is correct. For short times, the slopes of the structure functions are different owing to the single pole approximation. However, the error is not large.

The true atmospheric disturbance, assuming the frozen flow hypothesis and a multi-layer atmosphere, is nonlinear because the phase at time t_1 at location x_i is

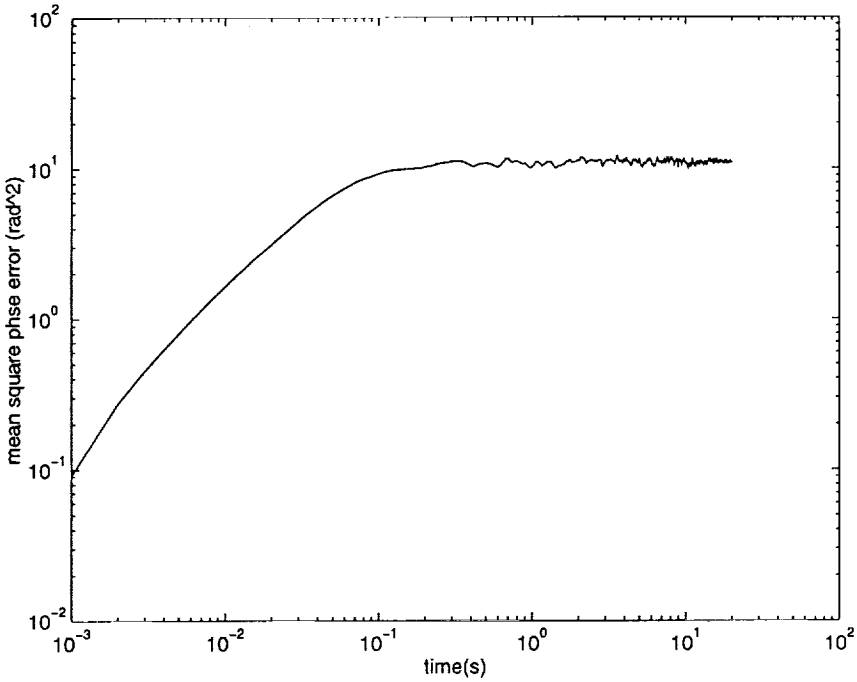

Figure 4-13: Temporal structure function $D(t)$ for one pole approximation to the true atmosphere.

directly correlated with the phase at time t_2 and x_j for all i and j. However, the model used here is effectively a linearized model of the true disturbance. It exhibits the correct spatial correlation from x_i to x_j at any particular time t, and a one pole approximation to the correct temporal correlation at x for time t_i to t_j but neglects the remaining correlation.

The next step in the disturbance model generation is to neglect the effect of 'piston'. The optics are insensitive to a phase error that is constant across the aperture. Therefore, the piston component of the disturbance, which constitutes the vast majority of the phase, is removed,

$$\Psi(x) = \psi(x) - \frac{1}{A_S}\int_S \psi(x)\mathrm{d}x \tag{4.39}$$

where the integral is over the region S, the aperture of the telescope, with area equal to A_S. Because the phase $\psi(x)$ has been discretized, the integral is actually a weighted summation over the 546 disturbance locations. The weights, or local areas, used in the summation are calculated using a rectangular rule integration. The disturbance

locations are found in 19 rings. The area associated with each annulus, which lies between concentric and consecutive rings, was assigned to the points on the ring at the outer radius of the annulus, and divided by the number of points on that ring. Other integral approximations could be used, however this was chosen to maintain radial symmetry in the disturbance. The subsequent phase disturbance $\Psi(x)$ is converted to an optical pathlength disturbance by scaling the phase by the wavelength of light, $\lambda = 2.2$ microns.

Finally, the disturbance model was placed in state space as follows. The symmetric spatial covariance matrix R was factored through a singular value decomposition to get its symmetric square root B_w,

$$R = U\Sigma V^H = U\Sigma U^H = U\Sigma^{\frac{1}{2}}U^H U\Sigma^{\frac{1}{2}}U^H = B_w B_w^T, \tag{4.40}$$

where U and V are identical unitary matrices, and Σ is the diagonal matrix of the singular values of R. B_w acts as the input matrix to the dynamic system

$$\dot{x}_w = A_w x_w + B_w w \tag{4.41}$$

$$y_w = C_w x_w + D_w w, \tag{4.42}$$

where $x_w \in \mathbb{R}^{546}$ is the disturbance state vector in which each state represents the disturbance phase at a location on the mirror, $C_w = \lambda(I - W)$, $D_w = 0$, $A_w = -\omega_0 I$, $\omega_0 = 16.6667$ rad/sec is the frequency of the single pole, and W is the matrix whose rows are identically the weights used to calculate the piston component of the disturbance. With this system driven by 546 uncorrelated unit intensity white noise processes contained in the vector w, y_w is the optical path difference (OPD) between undistorted and distorted wavefronts.

The RMS open loop optical path difference is given by the square root of the diagonal elements of the output covariance matrix R_w,

$$R_w = C_w X C_w^T \tag{4.43}$$

where X is the solution of the Lyapunov equation

$$A_w X + X A_w^T + B_w B_w^T = 0. \tag{4.44}$$

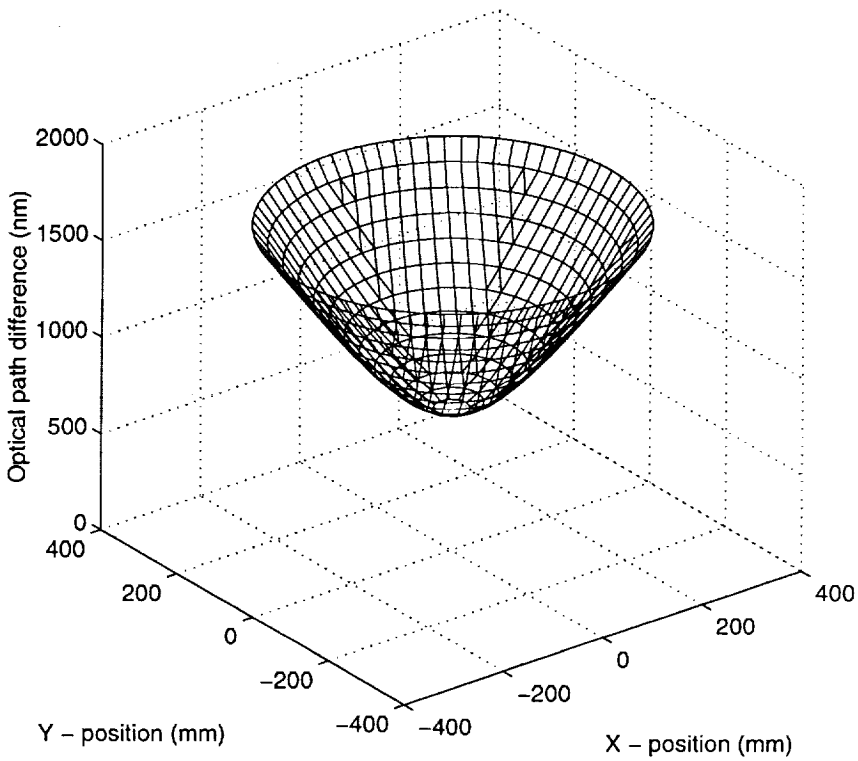

Figure 4-14: RMS optical path difference from disturbance model plotted as a function of position on the mirror.

The results are plotted in Figure 4-14. Note that the result is counterintuitive. One might expect that the OPD would be constant across the surface of the mirror, given that the atmosphere should have no preference of location on the mirror. This is true if the disturbance is not referenced to the surface itself. However, because piston is removed from the disturbance, the average across the surface of the mirror is subtracted, and the disturbance is referenced to the surface. Because the covariance of the phase between points on the surface decreases super-linearly ($\sim (\delta x)^{-5/3}$ for $x \ll L_0$), the center of the mirror has greater correlation with the average across the mirror than do the edges. Thus the center has a reduced disturbance when the average is subtracted.

Let us look at a modal basis for the disturbance. The atmospheric disturbance can be subdivided into an orthogonal basis of modes called Zernike modes [37]. The first Zernike mode is piston which has been removed from the disturbance. The second

and third Zernike modes, tip and tilt, satisfy

$$Z_{\text{tip}} = r\cos\theta \tag{4.45}$$

$$Z_{\text{tilt}} = r\sin\theta \tag{4.46}$$

where r and θ are polar coordinates of a location in the aperture. Subsequent Zernike modes have higher order radial polynomials and higher frequency circumferential values (2θ, 3θ, *etc.*). Noll [37] determined the contribution of each of these modes to the RMS OPD, and found that the majority is found in the tip and tilt modes. Higher order Zernike modes contribute a decreasing amount to the overall OPD RMS. Figure 4-14 shows this in that the RMS at the edges is much greater than the OPD RMS at the center. If tip and tilt were the only contributing modes, the OPD RMS would appear to be a cone, with zero OPD at the vertex. However, the higher order Zernike modes do contribute to the optical path difference, and thus the center is not zero.

The disturbance system was simulated with a vector of white noise inputs for a period of ten seconds to produce sample disturbance wavefronts. Four of these are plotted in Figs. 4-15–4-18. These wavefronts correspond to times at 10 msec intervals starting 9.8 seconds after the beginning of the simulation to allow the effects of initial conditions to die out. First, note that the wavefront distortion clearly exhibits spatial correlation. Uncorrelated distortion would appear much more jagged than any of these sample wavefronts. Because the spatial correlation of the distortion rolls off as $\kappa^{-\frac{11}{3}}$, low spatial frequency components are much more significantly represented than high frequency components. The general shape of the figures is bowl-shaped, with the depth of the bowl changing at each sample time. The fact that the shapes in each of the four figures are closely related, demonstrates the temporal correlation of the distortion. The wavefront distortion at each time instant is not independent, the atmospheric distortion can be seen to change slowly from the deep bowl shape of Figure 4-15 to the tilted, almost planar wavefront of Figure 4-18. Higher order Zernike modes are much more difficult to track from one figure to the next, but it

can be seen from Figure 4-18 that these do contribute significantly in addition to the dominant tilt.

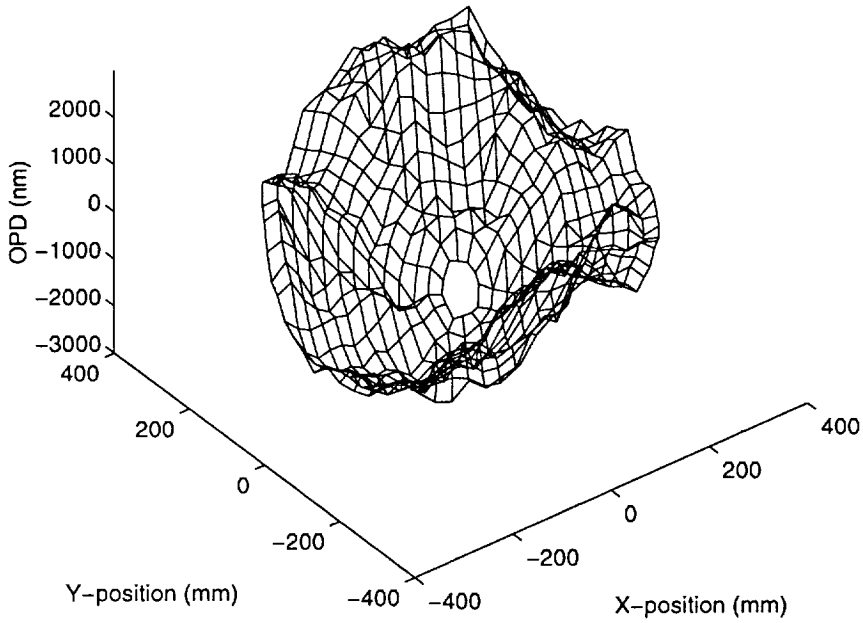

Figure 4-15: Simulated distorted wavefront t=9.80 s.

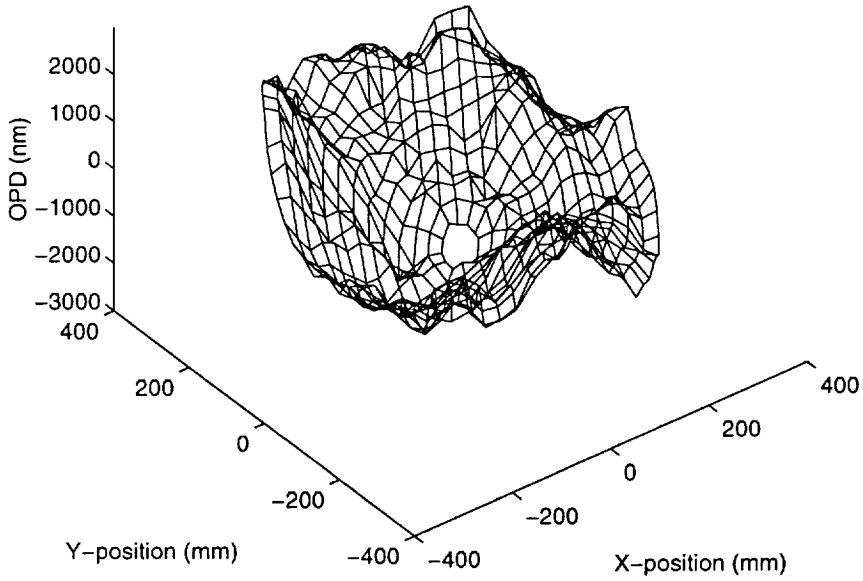

Figure 4-16: Simulated distorted wavefront t=9.81 s.

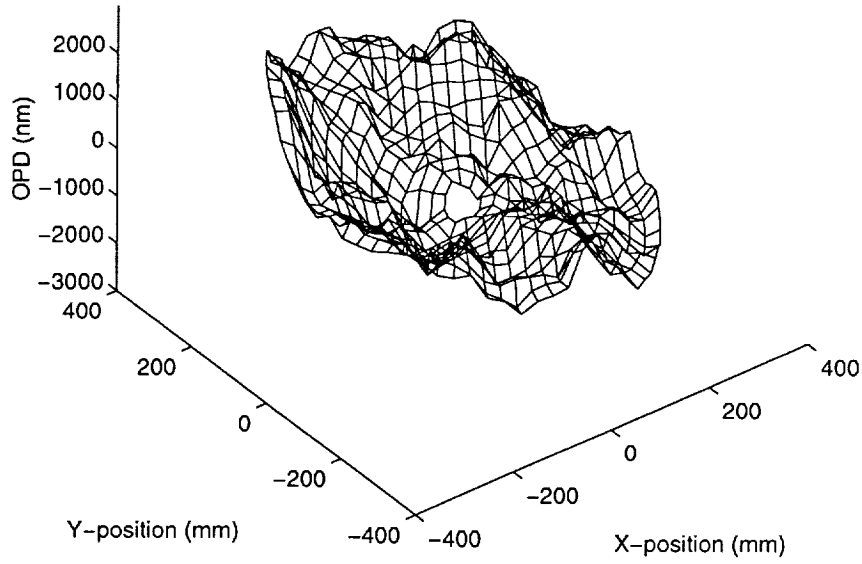

Figure 4-17: Simulated distorted wavefront t=9.82 s.

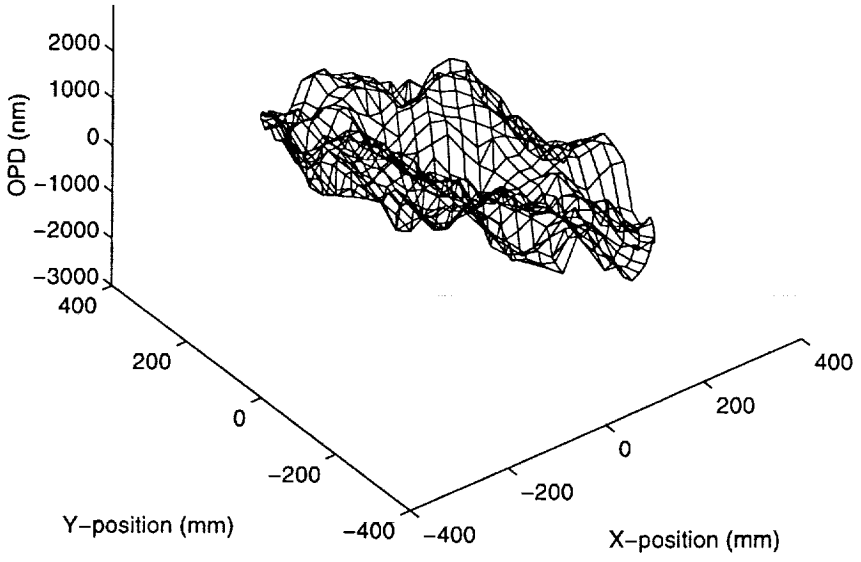

Figure 4-18: Simulated distorted wavefront t=9.83 s.

Chapter 5

Control Systems for Flexible Adaptive Optics

In this chapter, the processes developed in the previous three chapters are combined to produce a new control approach for force-actuated, thin facesheet adaptive optics. The chapter begins with a discussion of a number of different multivariable control approaches that could be used to design control systems for the deformable mirror. This discussion culminates in the presentation of a global control approach that is the dynamic reconstructor presented in Chapter 2.

A small sample problem is presented and the global control approach is compared to the approach used by Biasi and Gallieni [10] which was discussed in the introduction to this thesis. Following the comparison, stability robustness issues of the global control approach are discussed.

Finally, the full-scale problem is simulated and the results are presented. The simulation represents proof of concept for the global control approach, and shows the capabilities of this control methodology.

5.1 Force-Actuated Adaptive Optics

The primary difference between a high-impedance position-actuated system and a low-impedance force-actuated system is the presence of structural dynamic modes at

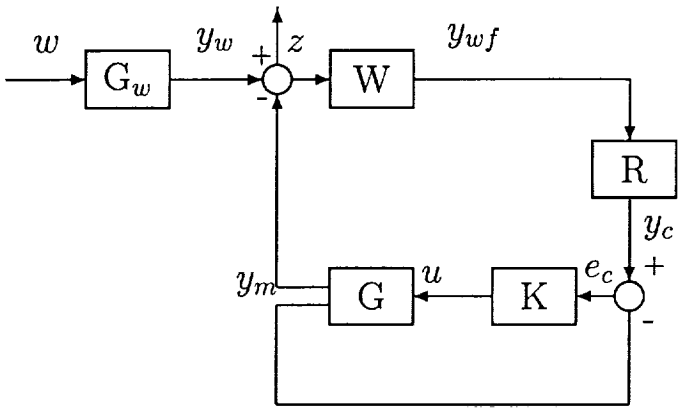

Figure 5-1: Block diagram for hierarchic control approach.

a much lower frequency. Thus control approaches for force-actuated adaptive optics should take the structural dynamics into account. Several different multivariable control approaches can be used to properly account for the structural dynamics. All of these rely on the structural modelling of Chapter 4.

The first three approaches use a hierarchic control approach similar to that used by Biasi and Gallieni which was discussed in the first chapter. This approach is shown schematically in Figure 5-1. An inner control loop is used, operated at a higher sample rate than the outer loop and at a high bandwidth so that the dynamics do not interact with the outer loop control. This inner loop feeds back gap sensor measurements to the actuators as in the Biasi and Gallieni approach. Then an outer loop contains a reconstructor with integral control. All three of these techniques take a different approach to designing the inner loop.

The first approach is to design a high bandwidth LQ servo [38] controller. This is essentially a multivariable PID controller in which the PID gains are designed using a Linear Quadratic Regulator (LQR) [20]. The LQR gains permit, in fact require, feedback from all gap sensors to all actuators. This non-collocated feedback, coupled with allowing collocated channels to be different, allows the closed loop singular values to be balanced thus enabling good tracking performance on all commanded

shapes, *i.e.*, input "directions." This control approach requires some modifications to the control design model so that the states of the system are the displacements at the actuator locations. This can be obtained through Guyan reduction [39, 40]. The dynamic reduction of the system down to the degrees of freedom at the actuator locations is an approximation, but for a large number of actuators should be a good approximation. This approach ignores actuator and sensor dynamics such as measurement delays. However, since LQR provides some guaranteed gain and phase margins [41, 42], the effect of these delays on stability can be ascertained.

The second approach is not to restrict oneself to full state feedback as the LQR controller requires. Thus one could design a high bandwidth servo controller using LQG [20] or $\mathcal{H}_\infty$ [43, 44, 45] based control techniques. These controllers would be designed similar to the LQR controller except that all the states of the system need not be available for feedback. Guyan reduction would not be necessary for these techniques, and a modal model of the system as shown in Section 3.4.2 could be used. This would allow the incorporation of sensor and actuator dynamics which could not be added in the LQR controller. Presumably a more accurate model of the sensor and actuator dynamics, in particular the delays associated with the actuation, would make for a better controller than LQR would provide. The penalty associated with this type of control is the larger number of states that would result from incorporating sensor and actuator dynamics. This would substantially increase the computation required to run the controller in real time. However, using a modal model of the system enables a large number of very high frequency modes to be truncated from the model of the system. It further would allow a more accurate model of the dynamics within the bandwidth since no Guyan reduction need be performed.

A third approach is to use Independent Modal Space Control (IMSC) [46, 47, 48]. In this approach, sensors and actuators would be combined into groups which are modally orthogonal. Each group would control only a single mode with some high frequency spillover before which each controller would have to roll-off. The large number of actuators and sensors means that a large number of modes can be controlled independently. Controlling enough modes and stiffening these modes so that

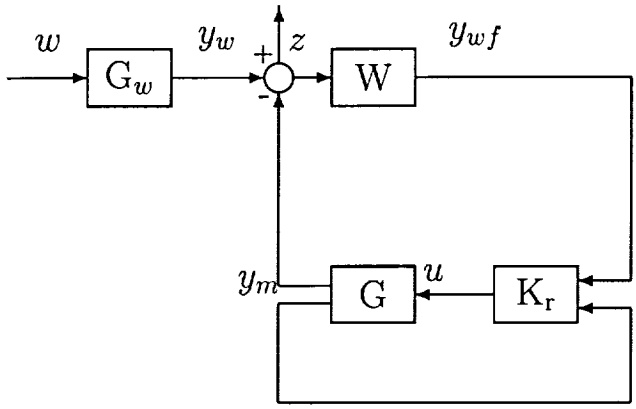

Figure 5-2: Block diagram for Global architecture control approach.

they are pushed outside of the bandwidth required for the outer loop would result in a quasi-static response of the mirror in this bandwidth. The resulting influence functions of the actuators could be measured and lumped into the existing reconstructor. This type of control would still require a very large amount of real time computation. Though the controllers are independent, they couple many actuators and sensors. Feedback from a large number of sensors to a large number of actuators is still required, and this implies that the computational burden will be high.

All three of these approaches use the hierarchic topology of Figure 5-1. The drawback of all of these is that in order to design the outer loop independently, the dynamic effects of the inner loop must be negligible in the bandwidth of interest for the integral control. The bandwidth of interest includes not only the frequency range over which the atmosphere must be tracked, but also a suitable range of frequency to roll-off the control. These requirements force the bandwidth and the sample rate of the inner loop to be quite high. Higher bandwidth implies that more dynamic modes are important, and a more accurate model is necessary. Higher sample rate implies that a large amount of computation is required in order to implement these controllers. Because all of these require feedback of all sensors to all actuators, and use a sample rate ten times higher than the outer loop, the costs are exorbitant.

A final approach, and the main approach of this thesis, uses a global architecture which operates at a single sample rate, and allows feedback of both wavefront sensors and gap sensors to the actuators. This feedback architecture is shown in Figure 5-2.

The global architecture combines the actions of both the inner and outer loop. It simultaneously processes information from the wavefront sensor and the gap sensors and feeds this back through the force actuators. The primary benefit is that because both loops are designed simultaneously, there is no need for the inner loop bandwidth to be considerably higher than the outer loop. Thus the global approach will use less control and need a less accurate model. The model must be designed with full knowledge of the interaction between the actuators and both groups of sensors, and thus there is no unmodelled interaction to destabilize the system as in the hierarchic architecture. This architecture can use any of the modern control techniques. However, in this thesis, LQG-based control is used. The disturbance model defined in the previous chapter is based on filtering a white noise input, and the performance measures of importance are RMS wavefront errors, thus the problem falls naturally into an $\mathcal{H}_2$ control framework.

5.2 Sample Problem

The problem of controlling a system with nearly 300 inputs and more that 500 outputs is immense. In order to test that the principles involved in performing dynamic reconstruction are of benefit, a smaller problem was first considered. This sample problem is representative of the control of the full mirror, but is considerably smaller in size. The sample problem is representative of the full order problem in two key ways. First, the system is circulant. Exploiting circulance is not a necessary step for a small problem, since it would not be difficult to solve the problem without circulance. However, as a test of exploiting circulance, it is a necessary step. Secondly, in order to have a problem for which the influence functions of the actuator are dynamic, and thus testing that the principal of using a dynamic reconstructor works, the dynamics of the low order problem must be representative of the full order problem.

In accordance with these directives, the sample problem consists of controlling an annular mirror with the same dimensions as the adaptive secondary so that the structural dynamics are in the correct frequency range. However, to simplify the modelling of the structure, the hyperbolic shape is ignored. A flat mirror is considered. The sample problem lays out six actuators around the mirror so that the system is circulant of order $N = 6$, just as the full scale problem.

5.2.1 Model development

For simplicity in the sample problem, the mirror is modeled as a flat plate. Otherwise, the dimensions of the mirror are the same as the full problem: outer diameter, 642 mm; inner diameter 60 mm. A finite element model consisting of 36 MSC/NASTRAN™ CQUAD4 elements is considered to represent the true dynamics of the system for the sample problem. Figure 5-3 shows a layout of the finite element nodes and elements for this model. The inner ring of nodes is constrained horizontally, but is elastically supported vertically to allow the piston, tip and tilt modes to approximate those of the large model discussed earlier. The bandwidth of this model is limited to about 1.5 kHz due to the small number of elements. However, it should suffice to evaluate the control techniques even if the dynamics are not correct at high frequency.

To drastically reduce the input and output dimensions, a set of only six actuators is used. The six actuators, and collocated sensors, are located at grid points 25, 27, 29, 31, 33, and 35. These grid points are equally spaced around the next to outer radius of the plate. In addition, grid points 25 through 36, *i.e.,* all the grid points in this ring of nodes, are considered performance outputs. The six non-actuated grid points in this ring, 26, 28, 30, 32, 34, and 36 are used to evaluate performance at locations at which actuators are not located.

The modelling of the wavefront sensors is simplified from that of Section 4.1.2. Rather than measure slope of the wavefront error, the wavefront sensor is assumed to measure the wavefront error itself at these twelve gridpoints. Thus for the hierarchic control architecture, the reconstruction matrix R is simply the identity matrix.

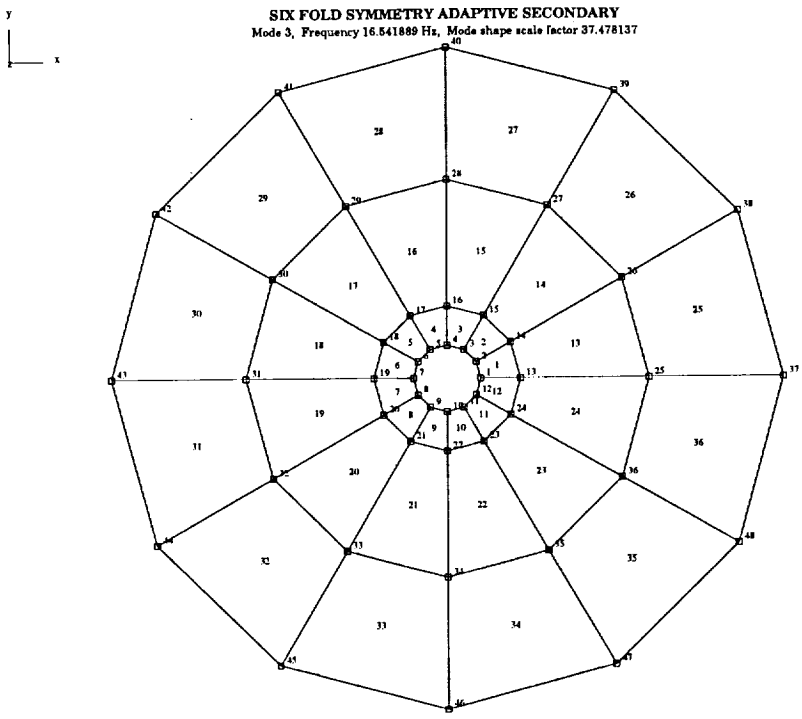

Figure 5-3: Arrangement of grid points for the Finite Element Model of the flat mirror sample problem.

The atmospheric model used in the sample problem is essentially the same as that described in Section 4.2. However, rather than being evaluated at 546 locations across the mirror aperture as in the full model, the atmosphere is measured at only 12 locations. These are the locations of gridpoints 25 through 36 in Figure 5-3. The correct spatial correlation in the wavefront at these locations is obtained from Equation 4.35. Temporal correlation between successive wavefronts is obtained again in the same manner as in Section 4.2.

5.2.2 Hierarchic PID control Approach

One objective of investigating the sample problem is to compare the multivariable control and dynamic reconstruction approach to the hierarchic PID control approach of Biasi and Gallieni [10] described in Section 1.2.3. Before doing so, it is useful to look first at the potential problems that lie in using the PID control approach. The

inner loop PID control consists of identical collocated PID controllers designed on a SISO basis. At high frequency the derivative feedback is rolled off so that the control remains proper. However, there is no general roll-off of the control at high frequency to make it strictly proper. Thus, this PID control relies on the natural rolloff of the system dynamics.

Four distinct problems may be encountered using this type of control which can act to limit the performance of the system when controlled using this hierarchic approach. The first problem is based on the fact that the PID controller does not roll off at high frequency. The PID inner control loop essentially relies on having little or no phase loss in the system so that the bandwidth can be extended. In fact, bandwidth will be limited because of phase lag associated with time delay, anti-aliasing filters, and imperfect collocation. The second problem arises from designing the SISO PID controller independent of closing other control loops. The dynamics of the mirror are such that these control loops are all highly coupled so that separately designed PID loops may unstably interact. The third problem results from using the same SISO controller on every loop. While the SISO controller was designed to provide good tracking to input commands, the multivariable tracking of the system may be poor because of a large spread in the singular values of the system. Finally, having to reduce the controller gain to solve these three problems may result in an inner loop controller that now interacts with the outer loop integral control. The bandwidth of the outer loop may have to be reduced to stabilize the system. This would result in a significant decrease in performance.

Let us now look at each of these four problems in a bit finer detail. The first problem is one of phase loss in the system. Figure 5-4 shows three transfer functions for the full order model of the hyperbolic mirror, *i.e.,* not the sample problem. These transfer functions show the significant effects of time delays and non-collocation on the phase of the system. In the figure, the dotted line is the transfer function for a collocated actuator and gap sensor in the second largest ring of actuators in Figure 4-8. Overlaying this line in magnitude, but not phase, is the same transfer function with a half time step delay for a sample and hold process, and a full time step delay for

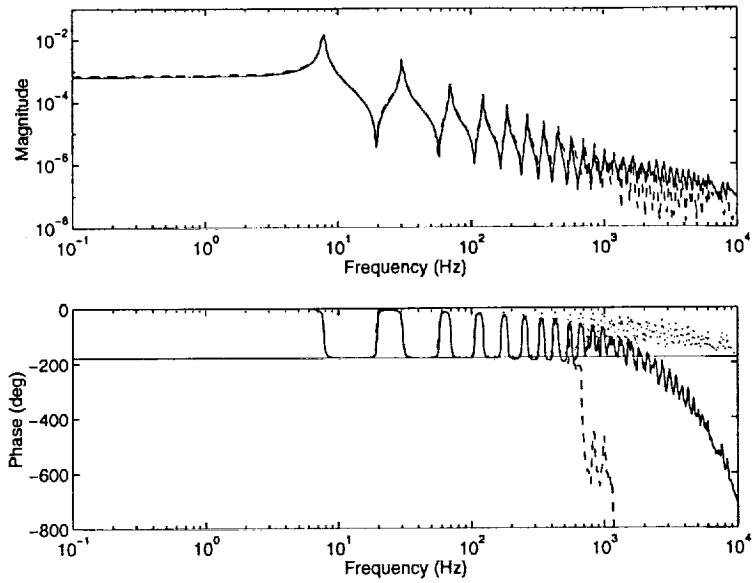

Figure 5-4: Transfer function magnitude and phase for an actuator and sensors near outer edge of mirror; ideal collocated transfer function (dotted), collocated transfer function with computer time delay (solid), and non-collocated transfer function from the same actuator to a sensor adjacent but nearer the edge of the mirror (dashed).

computation. The sample rate is 10 kHz. The dashed line is a non-collocated transfer function from the same actuator to an adjacent sensor in the outermost ring of sensors in Figure 4-8. The solid line shows clearly that significant phase loss occurs by 1-2 kHz, so that expecting a bandwidth of control wider than this is unreasonable. Next, the non-collocated transfer function has nearly the same magnitude as the collocated transfer function, but because of missed zeros in the alternating pole-zero pattern, the phase drops precipitously at around 700 Hz. This indicates two things. First, the non-collocated and collocated transfer functions are very highly coupled since their magnitudes are comparable. Second, small amounts of non-collocation, in this case only about 30 mm can have a calamitous effect on the phase. Now, 30 mm is a very large error in collocation. Such large errors will not exist in the system. However, at some frequency, which can be very difficult to gauge *a priori*, non-collocation effects such as this will occur. The rapid loss of phase that is associated with this will further limit the bandwidth of the SISO controllers.

These transfer functions from the full-order hyperbolic model of the mirror were used because near collocation was much more readily available for demonstration than on the low order sample problem. Returning to the sample problem, we look to design SISO controllers around the collocated actuators and sensors. The Bode magnitude and phase of the loop transfer function of a candidate controller are shown in Figure 5-5. At low frequency, the integral gain is limited by the presence of modes in the 6-30 Hz range. Higher integral gain would cause the phase margin at the first crossover (10 Hz) to be reduced. In the 100-1000 Hz range, rate feedback from the derivative gain keeps the magnitude of the loop transfer function high, and the system does not roll off quickly. Note that above 1 kHz there is a sparseness of modes due to the coarseness of the Finite Element Model. Comparison of this loop transfer function with the transfer function in Figure 5-4 shows that a much higher density of modes exist above 1 kHz for the true system. At any rate, the gain of the control in the 100-1000 Hz range is dominated by two things. The desire for good phase margin at crossover, and the need to roll-off with sufficient phase margin. The phase margin of this controller was optimized for a frequency of 100 Hz since this is the frequency at which many gain peaks are crossing unity. Higher overall gain is not possible because of the phase loss above 1 kHz. The loop must be rolled off by this frequency.

This SISO PID control yields a sensitivity, $(I + GK)^{-1}$, and complementary sensitivity transfer function, $GK(I + GK)^{-1}$, that are shown in Figures 5-6 and 5-7. The complementary sensitivity transfer function shows that up to about 8 Hz the system is tracking well. This is a very small range of frequencies for good tracking response. However, it was difficult to extend this bandwidth because of the difficulty in raising the integral gain because of the presence of the low frequency modes. The complementary sensitivity also shows that significant control authority is exerted at frequencies up to 1 kHz because of the slow rolloff of the system frequency response. The sensitivity transfer function indicates similar information. The residual tracking error is small for frequencies at which the sensitivity transfer function is small.

When this SISO compensator is copied and implemented at each of the six collocated sensor-actuator pairs, the results are even worse. The singular values of the

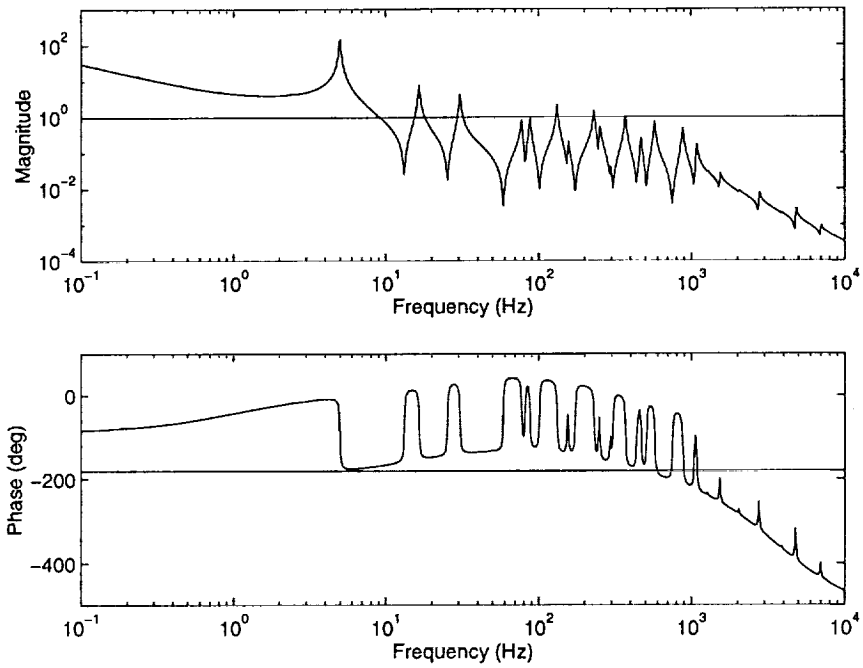

Figure 5-5: Bode plot of the SISO inner control loop. Magnitude and phase of the loop transfer function GK are shown.

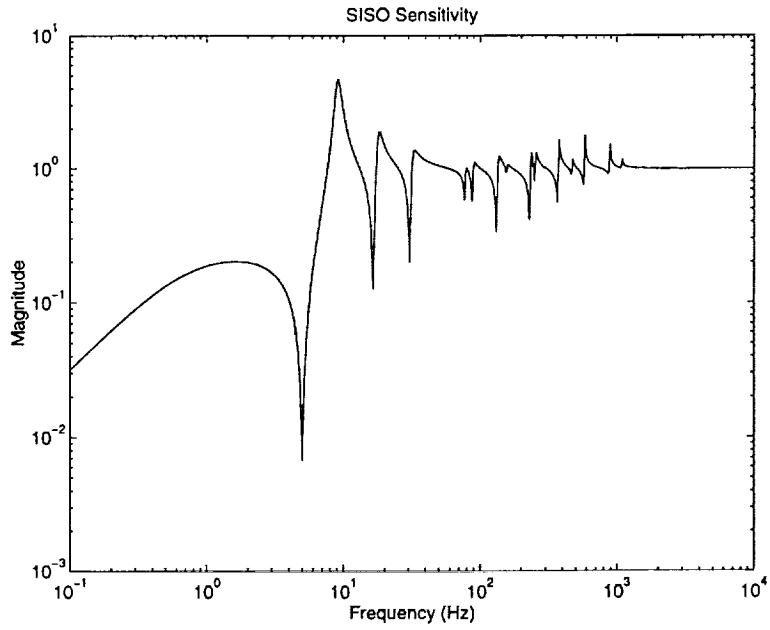

Figure 5-6: Sensitivity transfer function for the SISO PID controller.

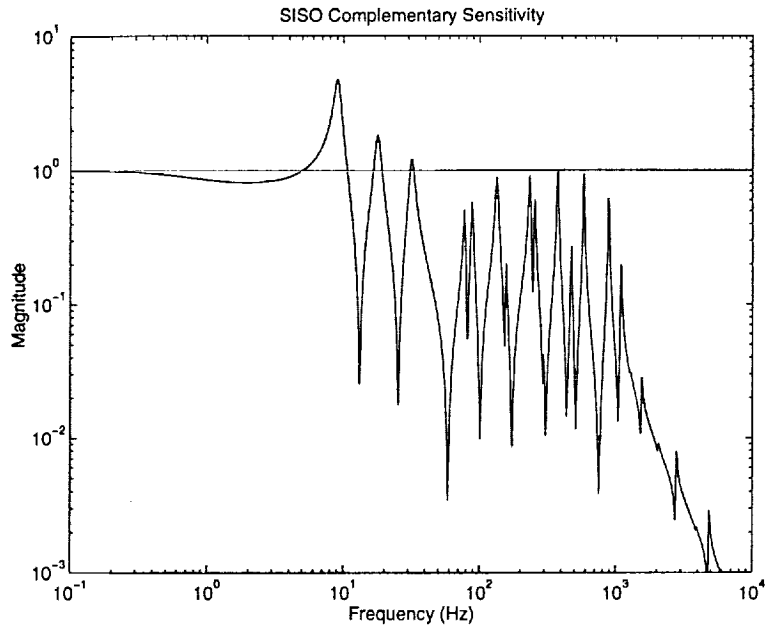

Figure 5-7: Complementary sensitivity transfer function for the SISO PID controller.

MIMO sensitivity and complementary sensitivity transfer function matrices are shown in Figures 5-8 and 5-9 respectively. First note that while there are six singular values for each of these transfer functions, two pairs are identical due to the symmetry of the problem, so that only four distinct singular values are evident in the figures. Near 1 kHz there are several sharp spikes in the sensitivity transfer function. This indicates that the system is close to instability [49]. In fact, the PID gains have already been reduced because higher gains caused instability. This indicates the second problem. Because of the high degree of coupling between actuators and sensors, independently designed SISO compensators do not perform as well when implemented simultaneously. The third problem is indicated by the variation in the singular values of the transfer functions. The SISO controller resulted in good tracking up to about 8 Hz. From the MIMO Complementary Sensitivity it can be seen that even nearly two decades below this at 0.1 Hz, the minimum singular value is only 0.5. This indicates that there are directions, or shapes of the mirror, that cannot be tracked well. This is not a suitable control system.

Finally, supposing that this control did achieve good tracking, the fourth problem

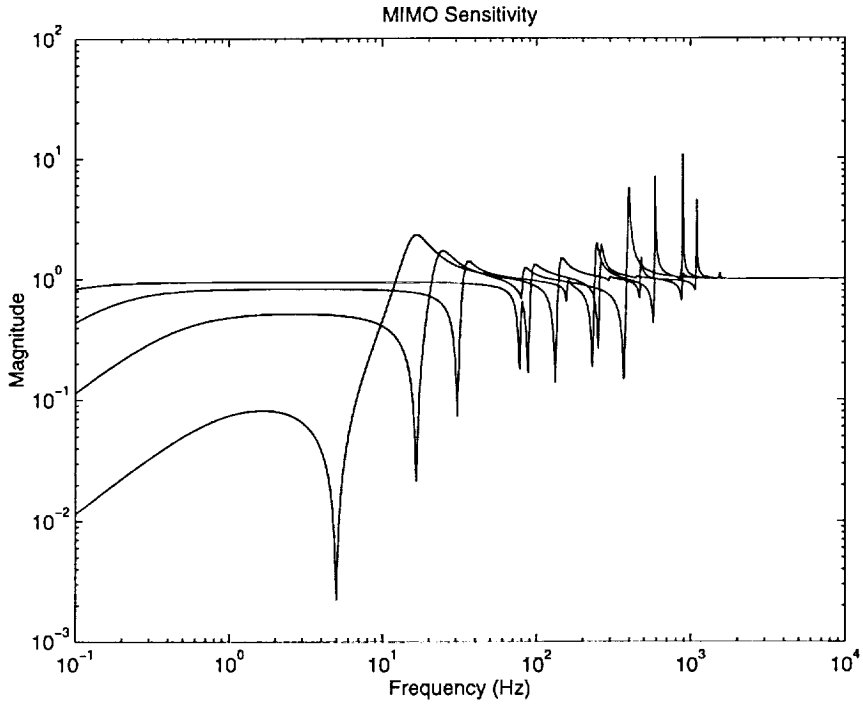

Figure 5-8: Singular values of the sensitivity transfer function matrix for the MIMO PID controller.

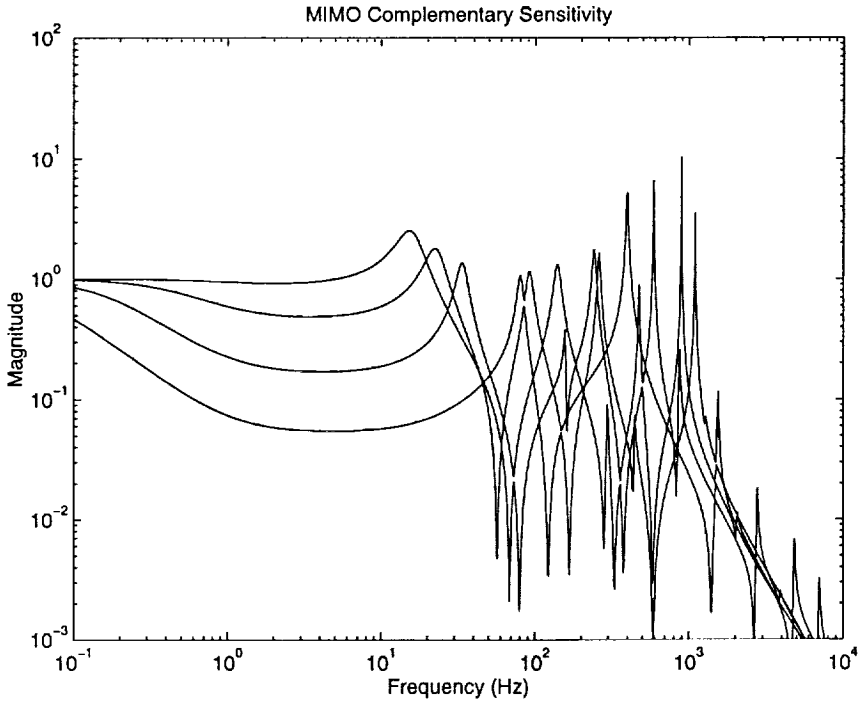

Figure 5-9: Singular values of the complementary sensitivity transfer function matrix for the MIMO PID controller.

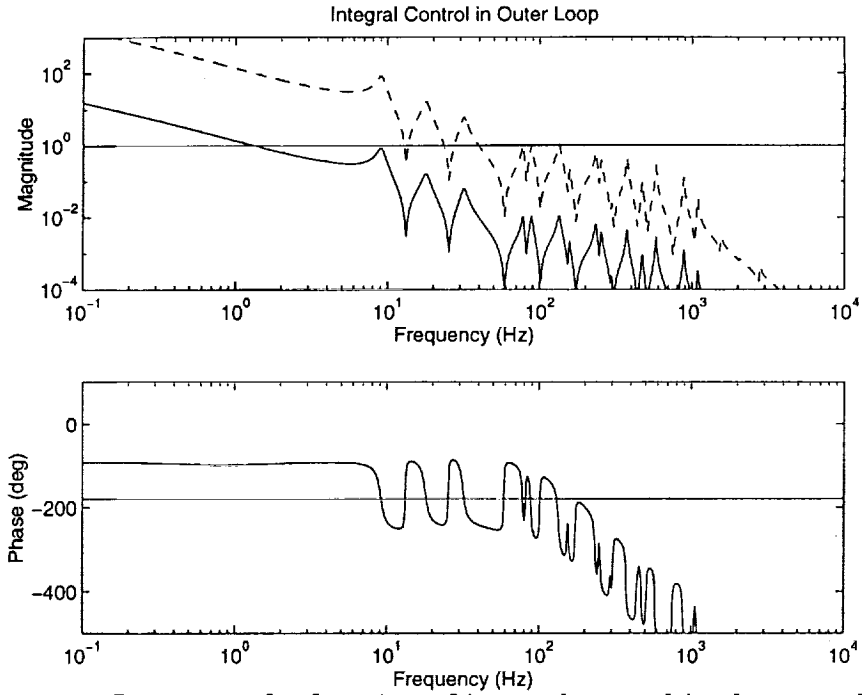

Figure 5-10: Loop transfer function of integral control in the outer loop with the inner loop closed. Dashed line represents gain that would be used for quasi-static system. Solid line gives the gain that is used to stabilize.

can arise: interaction between the inner and outer control loops. Figure 5-10 shows a SISO loop transfer function for the outer loop of the system with the inner loop closed. The dashed line in the figure is the loop transfer function for the integral gain that would be used if the system were quasi-static. With the phase frequently crossing the $-180°$ line with the loop gain greater than one, it is not surprising that the outer is unstable at this gain. The gain must be reduced by factor of nearly 60 to stabilize this loop. Lower gain means lower bandwidth. Lower bandwidth means lower performance.

Each of these four problems arise because there is insufficient modelling information in the control design model. The SISO PID controllers designed individually do not take into account more than one or two modes of the system. Implementing identical SISO PID controllers ignores the coupling between non-collocated actuators and sensors. It also causes an imbalance in the singular values of the closed loop system resulting in poor multivariable tracking. Finally, ignoring the coupling between the

inner and outer loops results in low bandwidth control designs which will perform poorly.

5.2.3 Comparison of Dynamic Reconstruction and Hierarchic PID Control Approach

In this section, the dynamic reconstruction approach is compared to that of the hierarchic PID control approach. The comparison is made on the basis of the following criteria: performance, robustness/margins, bandwidth/power usage, and complexity of implementation. The implementation costs are better investigated on the full-scale problem because of the strong influence of the number of actuators and sensors on the complexity of the implementation. The implementation comparison is therefore left until Section 5.3.

To place realistic limitations on each of the control techniques, the time delay associated with real-time implementation has been added to both models. For the hierarchic approach this is 1.5 times the sample period of 0.1 msec (one sample period for computation, one half period to approximate the zero order hold process of sampling the signal) for the gap sensors and 2 times the sample period of 1 ms for the wavefront sensors. In this case sample periods are accounted for by adding one full cycle for computational delay, one half cycle for the zero order hold process, and a further half cycle delay to represent the temporal average that the wavefront sensor measures. For the dynamic reconstruction approach, the gap sensors have time delay of 1.5 sample periods and the wavefront sensors have time delay of 2 sample periods. For this approach the sample period for both sensors is 1 ms since these loops are operated simultaneously.

Performance for these two different control architectures is measured as the residual RMS optical pathlength difference at twelve points on the mirror: grid points 25 through 36 in Figure 5-3. The performance is evaluated by solving for the Lyapunov equation associated with the closed loop covariance of the system. Robustness is compared on the basis of gain and phase margins for the system. Multivariable

gain and phase margins are obtained for these systems from the Sensitivity transfer function of the system in closed loop. From this transfer function it is possible to get conservative (sometimes very conservative) values for gain and phase margin of the system [50]. Multivariable gain and phase margin can be calculated for this system based on the magnitude of the maximum singular value of the Sensitivity transfer function $(I + GK)^{-1}$. With

$$\alpha = \frac{1}{\overline{\sigma}((I + GK)^{-1})} \tag{5.1}$$

the phase margin for the system, independently and simultaneously in every channel is given by

$$PM = \pm 2 \sin^{-1} \frac{\alpha}{2}, \tag{5.2}$$

and the gain margin is given by

$$GM = \frac{1}{1 \pm \alpha}. \tag{5.3}$$

The power usage of a controller is important also, because the temperature of the mirror must be tightly controlled to prevent additional phase error caused by heating of the air around the mirror. The overall power usage is calculated as the RMS of the actuator signals. For electromagnetic actuators with short time constants, the actuator command is proportional to the voltage applied to, or the current passed through, the actuators. The voltage and current are then proportional to the square root of the power usage. Therefore a measure of the power usage in terms of the actuator commands (forces) is sufficient to measure the power consumption of the actuators.

The measure of performance is the residual RMS optical pathlength difference (OPD) between the mirror and the incoming wavefront. Figure 5-11 shows the RMS optical path difference in nanometers for light with a 2.2 micron wavelength at the twelve performance locations located circumferentially around the mirror. In open loop, the figure shows that the OPD is approximately 1180 nm RMS at each of the twelve performance locations. The atmospheric disturbance shows no preferential direction, and the OPD is constant at a given radius of the mirror. The hierarchic

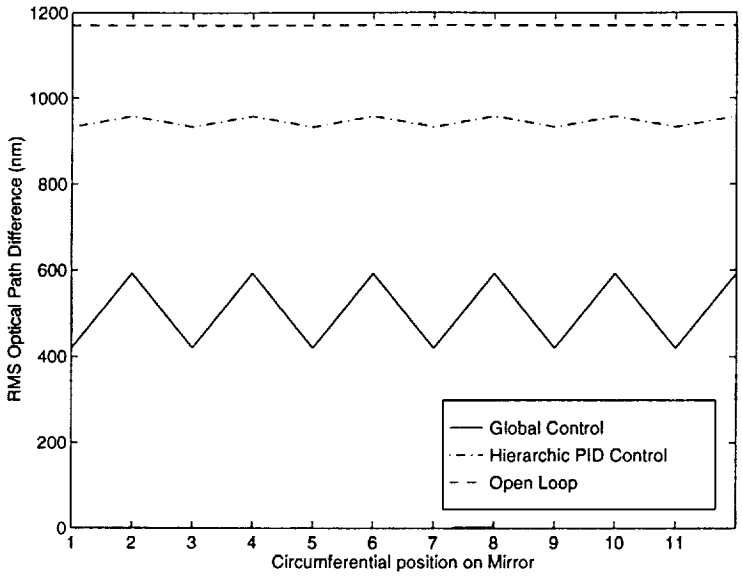

Figure 5-11: Open and closed loop optical pathlength difference for the hierarchic PID controller and for the global controller.

PID control design results in a closed loop residual RMS OPD of approximately 920 nm at the actuator and sensor locations, and a slightly higher 950 nm at the intermediate performance locations. The performance was limited primarily because the bandwidth of the outer loop integral control algorithm was limited to about 8 Hz by the presence of flexible modes still in the bandwidth. The problem was discussed in the previous section, and shown in Figure 5-10.

The controller designed using the global control approach performs better than this PID controller. It achieves an RMS OPD of about 420 nm at the actuator locations and about 600 nm at the performance locations between the actuators. Note that the high residual error between actuators occurs because of the small number of actuators in this sample problem. The wavefront at the intermediate locations on the mirror is sufficiently decorrelated with the wavefront at the actuator locations that a difference of almost 200 nm occurs between these locations.

Performance is only one metric of comparison. Sensitivity of the design to phase lag and modelling errors is another. The maximum singular value of the Sensitivity transfer function, $(I + GK)^{-1}$, is shown in Figure 5-12 for the global controller, and

in Figure 5-13 for the PID controller. The peak of the Sensitivity transfer function for the dynamic reconstructor, global controller, is approximately 2.1, so that $\alpha \approx .48$ yielding a phase margin of $\pm 28°$ and gain margin of $0.67 - 1.9$. These are fairly good classical gain and phase margins, though perturbations in lightly damped dynamics can result in very large gain and phase changes so that one must be careful in using the concept of these margins with lightly damped structures. By comparison, the margins on the hierarchic control are not nearly as good. The peak of the Sensitivity transfer function for the compensator formed by both the inner and outer loop closed simultaneously (Figure 5-13) is almost 10. The resulting gain and phase margins are very low: phase margin of $\pm 6°$ and gain margin of $0.91 - 1.11$. Admittedly, these margins are much lower than is necessary to achieve the level of performance that is obtained by this PID controller. The performance of the PID controller is limited by the interaction of the inner and outer control loops. This interaction manifests itself as the peak in the sensitivity transfer function at about 16 Hz. Because this interaction limits the performance, the bandwidth of the inner loop is unnecessarily high. A lower bandwidth inner loop, with the same gain at low frequency, would give similar performance, but would not exhibit the high sensitivities that result above 300 Hz. However, the bandwidth for these controllers was not altered in this way because the intended control approach for the hierarchic PID control is to have a wide bandwidth inner loop around which the integral outer loop is closed. This is what has been done.

In terms of bandwidth and power usage, the global controller again outperforms the hierarchic PID controller. The PID control has a bandwidth of 1200 Hz where the global controller bandwidth is only 166 Hz, measured by the last drop below -3 dB of the Complementary Sensitivity transfer function. The PID controller is required to have much higher bandwidth in an attempt to remove the flexible dynamics from the bandwidth of the outer integral control loop. This wider bandwidth results in control signals of 19.7 mN RMS from the PID controller while the global control uses only 14.1 mN RMS.

The bottom line is that the multivariable control approach to this problem gets

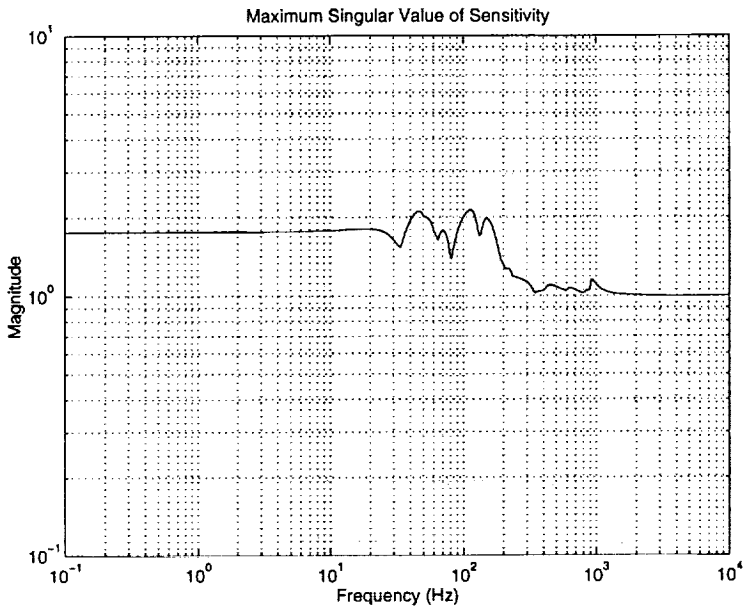

Figure 5-12: Maximum singular value of the Sensitivity transfer function for the Global controller.

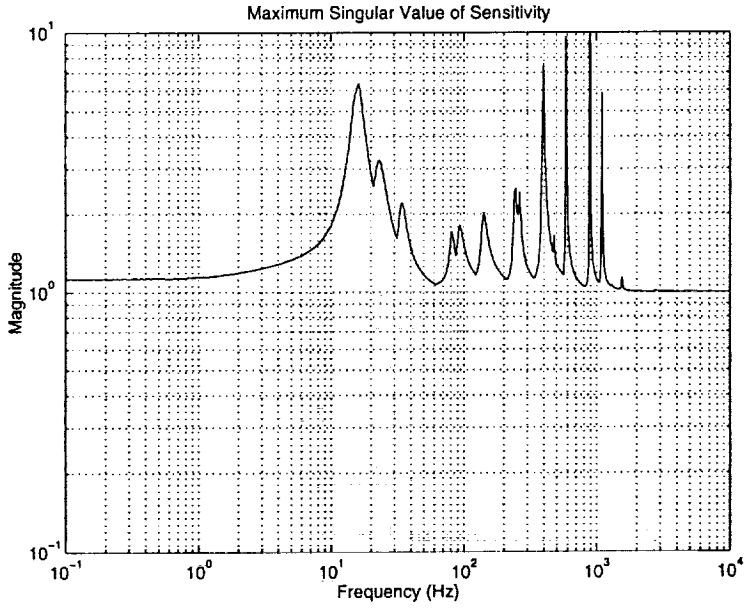

Figure 5-13: Maximum singular value of the Sensitivity transfer function for the PID controller.

better performance with lower bandwidth, lower power usage, and greater robustness than the hierarchic PID control scheme that is currently planned for use. There is a price to be paid, however. Because of the large number of actuators and sensors in the full control problem, real-time computation is more expensive. This will be shown in Section 5.3.1 when the full-scale problem with 270 actuators, 270 gap sensors and 252 wavefront sensor measurements is considered. Before proceeding to the full-scale problem, a further look at the issues of robustness for the global control is necessary.

5.2.4 Robustness

In order to handle the very large number of sensors and actuators in the full-scale control problem, this thesis has relied on the symmetry of the mirror to enable the dynamics and control of the mirror to decouple into essentially four smaller problems. The question arises: what are the effects of asymmetry on the system?

Clearly, if the system does not fully exhibit circulant symmetry then it will not fully decouple. The effects of asymmetry can be characterized in two ways; its effect on the eigenvalues, and its effect on the eigenvectors of the system.

In modelling the structural dynamics of the mirror, it was possible to first build a modal model of the structure, and then transform the inputs (B) and outputs (C) with the circulant transformation T. The transformation of the B and C (and D) matrices resulted in a decoupling of the dynamics of the system into groups of modes. These modes were characterized by their Fourier number. The number of circumferential nodes in the mode shape was related to the "frequency" of the transformed mode. Many forms of asymmetry will result in changes in the eigenvalues of a structure. Irregular mass distribution, variations in the stiffness of material, and variations in thickness of the mirror will all cause perturbations that will alter the eigenvalues of the system. However, regardless of whether a model is circulant, it can be placed in modal form so long as the eigenvector matrix is full rank. In this modal form, the circulant transformation can still be applied to the B and C matrices of the system, and the amount of decoupling can be observed. The remaining coupling is due to the

asymmetry of the system, and thus the amount of decoupling is primarily affected by the eigenvectors, not the eigenvalues.

Uncertainty and variability in modal frequencies is a characteristic of structural control that has received considerable attention [51, 52, 53, 54, 55, 56, 57, 58] because it is the dominant form of uncertainty. The control techniques that have been used to provide robustness to frequency uncertainty include Classical control techniques [59, 60], robustified LQG-based techniques [61, 62, 51, 63], Maximum Entropy [64, 65, 63, 52, 57, 58], Multiple Model control [66, 67, 51, 63, 52], Popov Control Synthesis [53], $\mathcal{H}_\infty$ control [54, 52], μ synthesis [55, 52], and real-μ synthesis [56]. Because the systems decouple in modal groups, frequency uncertainty, so long as it is treated as independent uncertainties for each mode, can be addressed after the circulant transformation is applied and the system is decoupled. At that point, any of these control techniques can be applied to the circulant decoupled systems.

The more difficult problem is dealing with asymmetry that results in coupling of the eigenvectors after the circulant transformation. It would be very difficult to analyze, or synthesize control for such a system using techniques that employ parameter robustness. The sheer number of parameters, all of the mode shapes for all of the modes, makes this infeasible. Instead one would hope to use the small gain theorem [68] to bound errors between the nominal and perturbed plants.

Two examples were created to demonstrate the effect of asymmetry on the circulant transformation. The first considers eigenvector asymmetry only, the second considers asymmetry that causes both eigenvector coupling and eigenvalue changes.

The first example uses the existing finite element model for the sample problem. The actuator locations are considered to be uncertain to within a tolerance of 0.6 mm from the nominal location. The locations were randomly perturbed within a 0.6 mm square from their nominal location. The perturbed modeshapes were obtained through bilinear interpolation from the original eigenvectors. The results are mixed. Figure 5-14 shows the four distinct transfer functions that make up the nominal system. Overplotted with those are the same transfer functions for the perturbed system. The transfer functions are indistinguishable. This indicates that the pertur-

bation is very small and should be benign. To corroborate this, Figure 5-15 shows nine transfer functions of these two systems after the circulant transformation is applied. For the nominal system (solid line), the transformation diagonalizes the transfer function matrix. However, for the perturbed system (dashed line) it can be seen that this portion of the transfer function matrix is diagonally dominant, but not diagonal. The diagonal terms are indistinguishable from the nominal system. But the off-diagonal transfer functions are not zero. The perturbed system is not circulant and therefore not diagonalized by the transformation. However, it can be seen that the magnitudes of the off-diagonal terms are small, more than two orders of magnitude less than the diagonal. This seems to indicate that the perturbation is negligible.

The off-diagonal elements appear small for this perturbation. However if we try to use the small gain theorem [68] to bound a measure such as the multiplicative error caused by the perturbation, we are out of luck. The multiplicative error reflected at the input of the plant for this system is given by

$$e(s) = G(s)^{-1}\tilde{G}(s) - I, \tag{5.4}$$

where $G(s)$ is the nominal transfer function of the system and $\tilde{G}(s)$ is the actual transfer function. By the small gain theorem, a closed loop system is guaranteed to be stable if

$$\overline{\sigma}(C(s)) < \frac{1}{\overline{\sigma}(e(s))} \tag{5.5}$$

where $C(s) = K(s)G(s)(I + K(s)G(s))^{-1}$ is the complementary sensitivity transfer function. Figure 5-16 shows the singular values of the multiplicative error of the perturbed system. At several of the resonances the magnitude of the singular values is very large, despite the small perturbations. Figure 5-17 shows the small gain test from Equation 5.5 applied to the system. The inverse of the maximum singular value of the multiplicative error, e(s), is clearly less than the maximum singular value of C(s) at several of the resonances indicating that stability cannot be guaranteed with this test. The magnitude of the maximum singular value of the multiplicative error indicates that the complementary sensitivity would have to be less than 0.1 at the first resonance in order to guarantee stability via the small gain test. This implies that

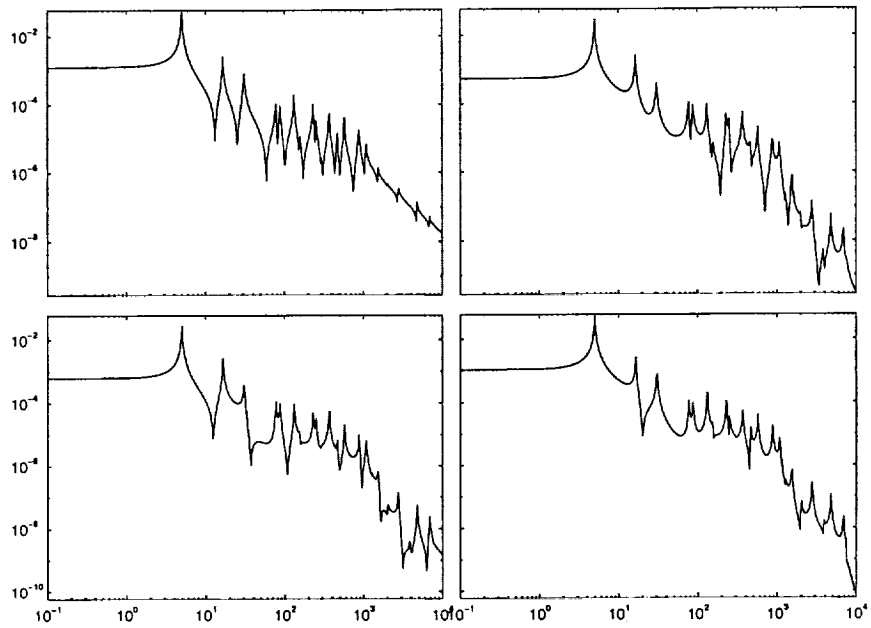

Figure 5-14: The four distinct transfer function of the nominal system (–) with the transfer function of the perturbed system (- -).

to use this test would severely limit the performance attainable by any controllers. An important point to note is that the multiplicative error is independent of the form of the controller. The error is not caused by the fact that a circulant controller has been used, we are simply more aware of the fact that we have relied upon the circulant nature of the system to design the controller. The multiplicative error is the same regardless of the type of controller. Therefore, any controller no matter what technique was used in control design would be faced with the same restrictions by this test. Clearly, this is an overly conservative test.

Finally, for a definitive test, the perturbed system was simulated with the controller designed for the nominal system. As can be expected from the very small differences in the system, the perturbed system is stable and obtains only marginally worse performance than the nominal system as shown in Figure 5-18. This figure shows the RMS optical path difference for the nominal and perturbed system, as well as for the system in open loop.

As an example of asymmetry causing eigenvalue changes, a finite element model

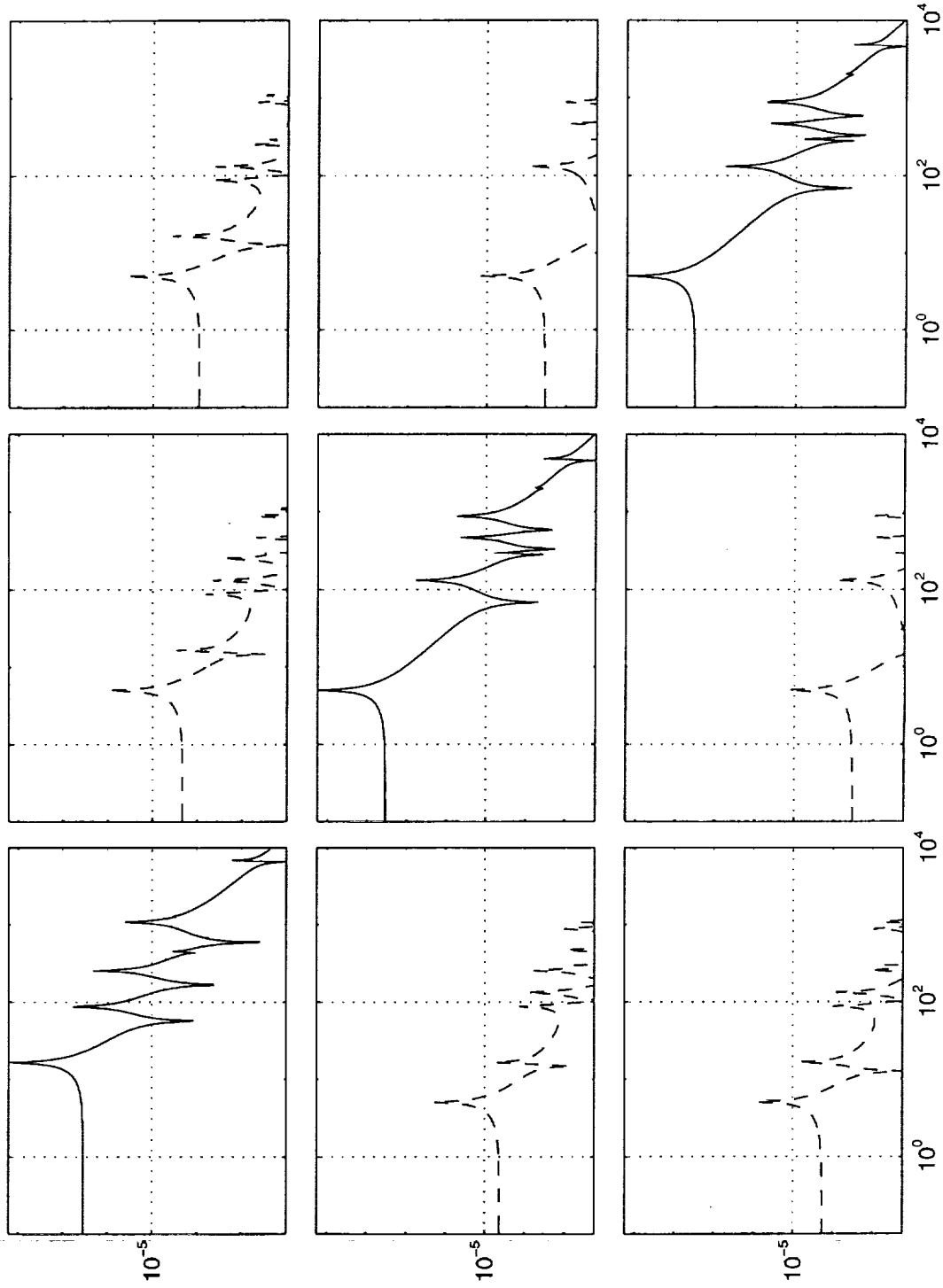

Figure 5-15: Transfer functions of the nominal (–) and perturbed (- -) systems after circulant transformation.

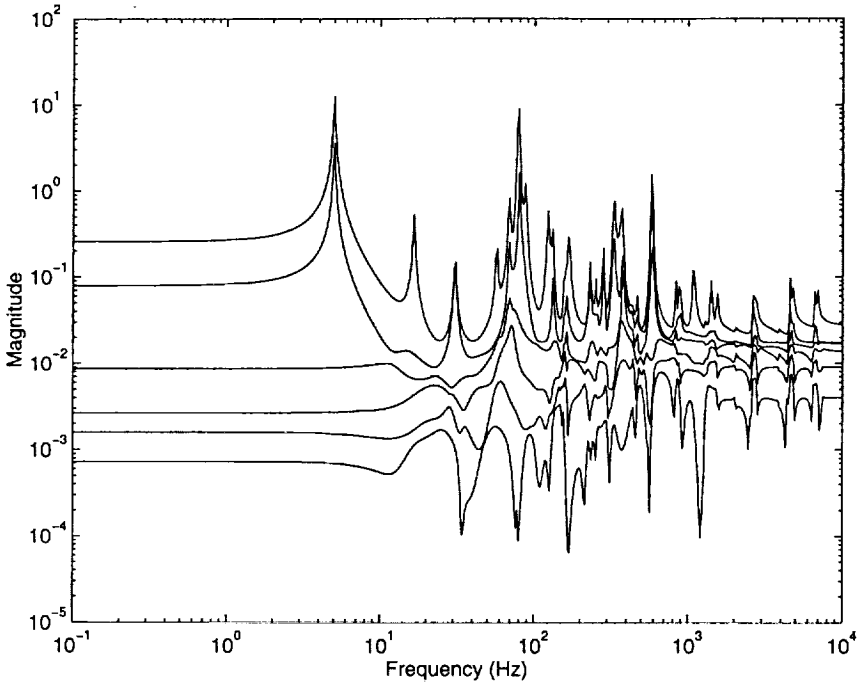

Figure 5-16: Singular values of the multiplicative error e(s) for the perturbed system.

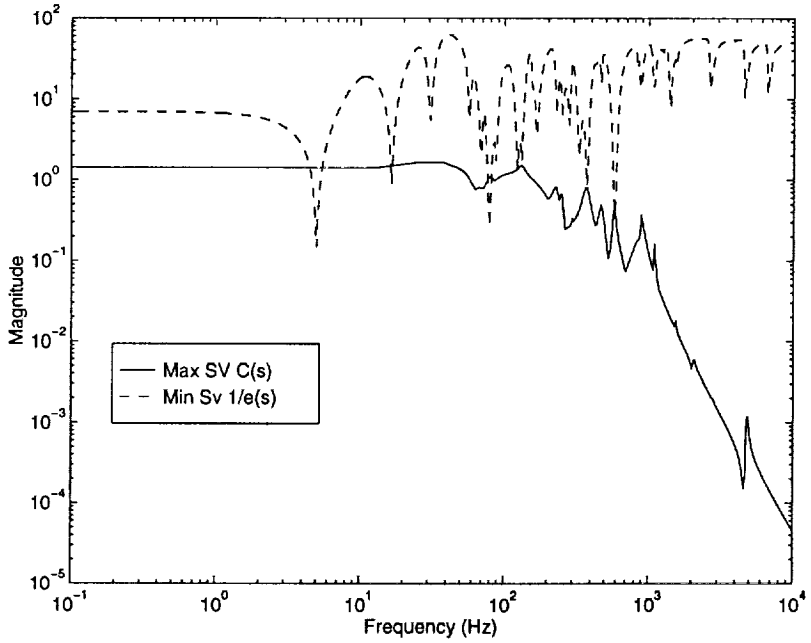

Figure 5-17: Small gain theorem test. For stability $\overline{\sigma}(C(s)) < \frac{1}{\overline{\sigma}(e(s))}$.

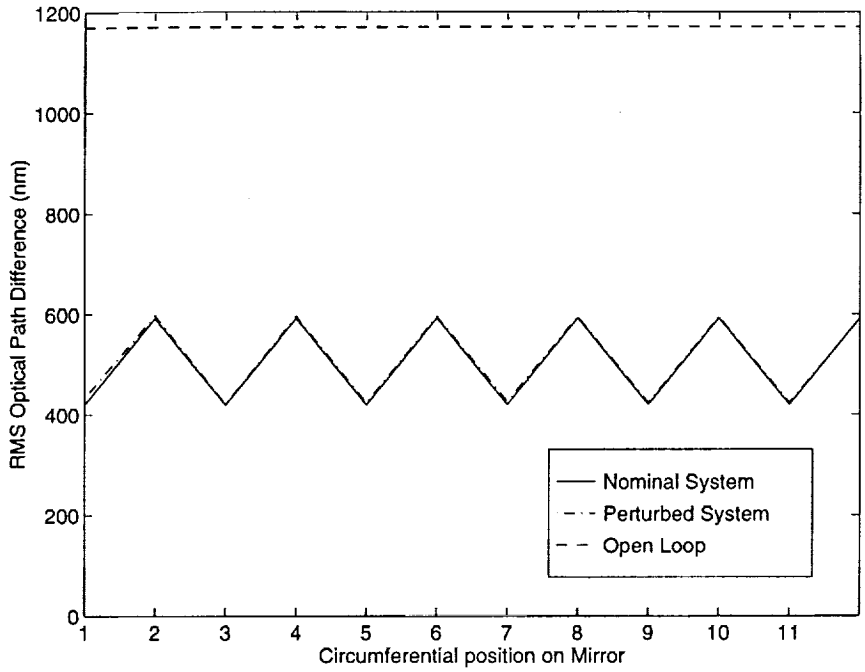

Figure 5-18: Open and closed loop optical pathlength difference for the nominal system and the perturbed system with the multivariable controller.

of the sample problem was created in which the thickness of each of the 36 CQUAD4 elements of the mirror, nominally 2.0 mm, was given a randomly selected thickness with a Gaussian distribution with 3σ of 0.1 mm with a mean value of 2.0 mm. The results of the frequency perturbations are shown in Table 5.1. For both the nominal model and the perturbed model, the first 29 modal frequencies are listed. It can be seen that with a thickness variation on the order of $\pm 5\%$ (3σ) the errors in frequency for the model are less than 1% for all but one of these 29 modes. This is a fairly benign effect.

Variation in the thickness across the mirror results in both eigenvalue and eigenvector perturbations. Not only are the eigenvalues different, but the system no longer fully decouples. For this perturbation, the results are very similar to that of the actuator location perturbation. At the resonances, the multiplicative error test is violated. Yet in simulation, the system was stable and performed nearly as well as the nominal system.

The multiplicative error test is clearly unworkable at the structural resonances. If

Table 5.1: Perturbed frequencies

Nominal Frequency (Hz)	Perturbed Frequency (Hz)	Frequency Difference (Hz)	Percent Difference (%)
5.00	4.97	-0.03	-0.69
5.00	5.00	0.00	0.01
16.54	16.53	-0.01	-0.08
30.60	30.64	0.03	0.11
30.60	30.74	0.14	0.44
77.35	77.79	0.44	0.57
77.35	77.81	0.46	0.60
87.75	87.85	0.10	0.11
131.92	131.96	0.04	0.03
131.92	132.59	0.66	0.50
156.10	157.05	0.95	0.61
156.10	157.60	1.50	0.96
230.03	230.91	0.88	0.38
230.03	231.72	1.69	0.73
251.67	251.96	0.29	0.12
294.80	295.88	1.07	0.36
294.80	297.99	3.19	1.08
368.99	371.50	2.51	0.68
368.99	371.67	2.67	0.72
441.42	443.39	1.96	0.44
465.92	466.47	0.55	0.12
465.92	469.20	3.28	0.70
574.31	577.97	3.66	0.64
574.31	578.61	4.30	0.75
861.43	862.87	1.44	0.17
861.43	865.91	4.48	0.52
878.88	883.30	4.43	0.50
878.88	885.48	6.60	0.75
1082.02	1088.63	6.62	0.61

we consider, however, that at the resonances uncertainty and variability of the system can be handled through parametric uncertainty, and use the multiplicative error as a guide away from resonances, a workable controller which achieves good performance, and is robust to realistic perturbations may result.

5.3 Full-Scale Problem

We now consider simulations on the full-scale problem. The models for this problem have been presented in Chapter 4. The system has 270 actuators, 270 gap sensors, and 252 wavefront measurements in the form of two slopes for each of 126 wavefront sensors. The atmospheric model for this system contains 546 disturbance inputs and 546 performance outputs. The dynamic model consists of 55 modes up to a frequency of 1 kHz and contains the static component of modes above 1 kHz.

Let us begin this section with a final comparison of the dynamic reconstructor approach (global control) versus the hierarchic control approach. The question that remains is the implementation costs associated with the two techniques. The discussion of implementation has been left until this section because the cost of implementation depends very heavily on the number of actuators, so that a fair comparison of implementation costs could not be obtained from the sample problem.

5.3.1 Implementation Comparison

It makes more sense to compare the implementation procedure for the control architectures at full scale because the number of computations required rise as the square of the number of actuators and sensors.

Any linear controller can be put in an A, B, C, D form for implementation as shown in the the following equation:

$$x_{k+1} = Ax_k + By_k \tag{5.6}$$

$$u_k = Cx_k + Dy_k. \tag{5.7}$$

In general, the A matrix can also be block diagonalized with 2x2 blocks. Thus the computations required in the A matrix multiplication, which are linear with the number of states, are negligible when a very large number of actuators and sensors are present. Thus it is mostly B, C, and D matrix multiplications that matter.

The number of computations required for each control architecture is shown in Table 5.2. For the global control architecture, the B, C, and D matrices are in general

Table 5.2: Summary of implementation costs

Control Type	Computations per 1kHz cycle
Hierarchic with collocated PID	68040 +1350(10)
Hierarchic with global PID	68040+65824(10)
Global without circulance	395020
Global with circulance	110014

fully populated. Thus every cycle would require 395020 computations. However, because the system is circulant, these can be made block diagonal. This sparseness results in about one quarter of the computation of the fully populated matrices, and only 110014 computations are required with no loss in performance.

For the hierarchic PID control approach, the outer loop computation requires only multiplication of the reconstructor R which is a 252×270 matrix requiring 68040 computations. The inner loop calculation is much smaller because of the restriction to collocated feedback. It requires only 1350 calculations per cycle, but is implemented at 10 kHz so there are 10 cycles per outer loop cycle. If global feedback of the inner loop is permitted (and assuming that this feedback is circulant) the number of computations in the inner loop is 65824. At 10 kHz this would require 726280 computations per 1 kHz cycle including the reconstructor computation.

Again the final result is that the global architecture requires about 35% more computation than the hierarchic loop: 110014 computations versus 81540.

5.3.2 Optimization of Implementation

Recalling from Section 3.3, it is possible to find an approximate optimum degree of circulance for the system in order to minimize the number of real-time computations that must take place. Equation 3.66 give the optimum degree of circulance as

$$N_{opt} = \sqrt{2\left(n_c + \frac{n_y n_u}{n_y + n_u}\right)}. \tag{5.8}$$

For our system, $n_u = 270$, $n_y = 270+252$, and n_c is equal to the number of states of the structural dynamics that are kept plus the number of states in the disturbance model. The number of states in the disturbance model is nominally 546. Approximately 25

modes of the system are important up to the Nyquist frequency of 500 Hz. This leads one to pick $n_c \approx 600$. Then substituting into Equation 3.66 yields $N_{opt} \approx 40$. This implies that much more computational savings could be gained by increasing the degree of circulance. This optimization is not quite accurate, however, because it ignores the fact that n_y and n_u must be multiples of N. But it does indicate that an increase in the degree of circulance would yield computational savings.

5.3.3 Results

Finally, having performed the comparison of the two control approaches on the sample problem, it remains to be shown that a solution can be obtained for the full scale problem. A circulant model of the system was obtained through the procedures shown in Chapter 4. The decoupled model consisted of four components. Two of these components have 45 actuators and 87 sensors, and the other two have 90 actuators and 174 sensors. Each of these four can be solved independently, in parallel if need be.

For each of the four problems, the control problem was set up independently and the two Riccati equations were solved using Matlab™ on a Sun Ultra1. Figure 5-19 shows the results of the widest bandwidth controller that seemed feasible. The open loop RMS optical pathlength difference ranges from about 800 nm at the center of the mirror, but is larger at the edges with a value of approximately 1700 nm. It can easily be seen from Figure 5-19 that the closed loop control has significantly reduced the pathlength difference. The closed loop RMS pathlength difference varies radially with peak performance not at the center of the mirror, but slightly further out. This can be seen more clearly in Figure 5-20 which shows just the closed loop OPD. From a maximum of about 520 nm to a minimum of 380 nm, there is a variation of approximately 140 nm OPD across the mirror. Overall, the performance improvement is 1200 nm at the mirror edges where the open loop OPD is the largest to 300 nm at the center of the mirror.

The bandwidth for this controller is approximately 150 Hz. With significant control being exerted on some modes up to 500 Hz as can be seen from the maximum

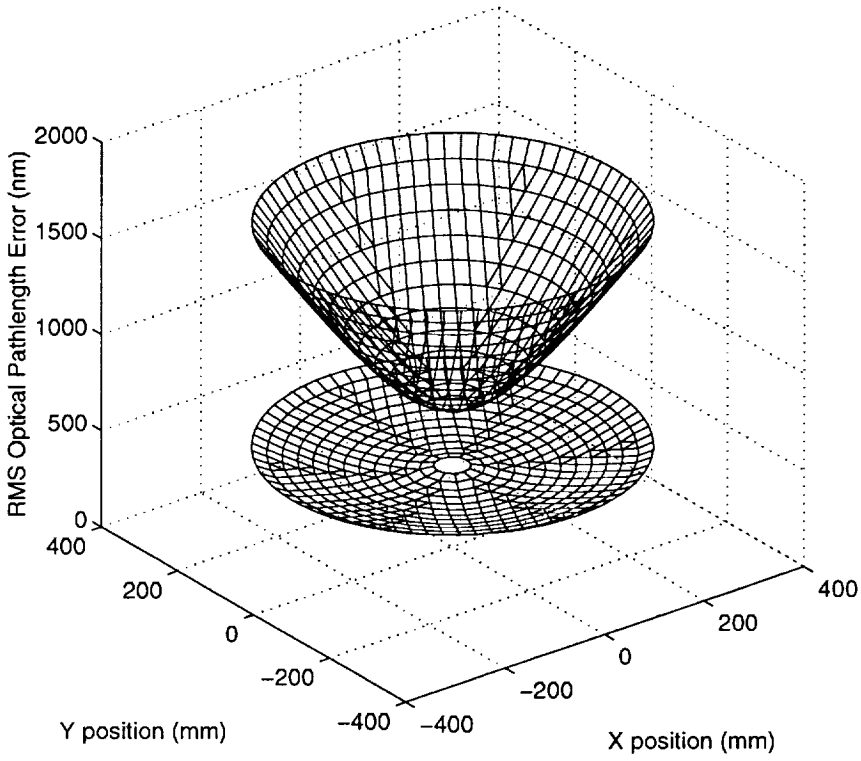

Figure 5-19: RMS OPD in open and closed loop.

singular values of the Complementary Sensitivity transfer function shown in Figure 5-21.

From Figure 5-20 it is also possible to detect the beginning of "waffle" in the output RMS. Looking along the edge of the mirror, "waffle" is observed to be a residual wavefront error that looks like a waffle. Rather than having a uniform output error across the surface, there are regions in the interior of each wavefront sensor subaperture that have higher residual error than on the edge. The cause of this waffle is that we have no measure of the wavefront in the interior of the wavefront sensors. Recall that the Shack-Hartmann sensor measures the average slope across the subaperture. This integral of average slope over the area of the subaperture was converted to a line integral of the wavefront phase on the boundary of the subaperture. Thus the only positions on the mirror for which information is obtained are on the boundary of subapertures.

Viewed in a slightly different manner, if the wavefront phase is fixed on the bound-

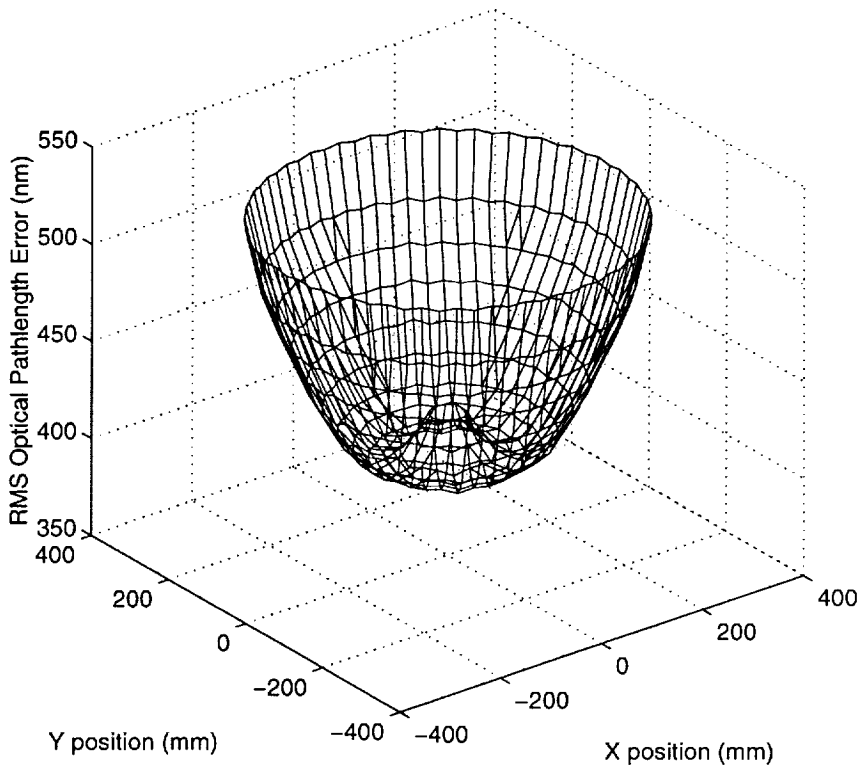

Figure 5-20: Closed loop OPD RMS as a function of position on the mirror.

ary of a subaperture, regardless of what is in the interior, the average slope is unaffected. Thus waffle is an unobservable mode of the atmosphere for which correction can be made only on the basis of a model of the correlation of the system, and not on the basis of measurements.

Finally, Figure 5-22 shows the maximum and minimum singular values of each circulant block of the sensitivity transfer function for this controller. From the low magnitude of the maximum singular value, we obtain a measure of the robustness of this compensator.

Multivariable gain and phase margin can be calculated for this system based on the magnitude of the maximum singular value of the Sensitivity. From Equations 5.2 and 5.3, the gain and phase margins are calculated from the inverse of the maximum singular value of the sensitivity transfer function,

$$\alpha = \frac{1}{\overline{\sigma}(S)}. \tag{5.9}$$

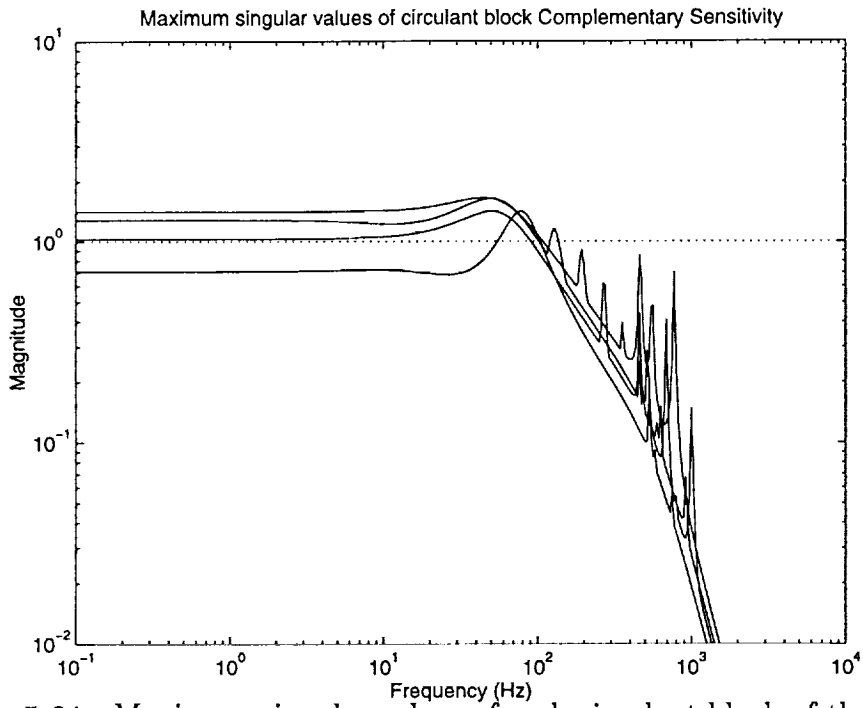

Figure 5-21: Maximum singular values of each circulant block of the complementary sensitivity transfer function for the full scale global controller.

The maximum singular value of the Sensitivity transfer function shown in Figure 5-22 is $\overline{\sigma}(S) = 1.56$ so that the gain margin is roughly from 0.61 to 2.8, and the phase margin is $\pm 37°$. These indicate that in classical terms, the compensator exhibits good stability margins.

This simulation of the full-scale system has shown, first of all, that the global control approach is feasible for a system of this size. It is not trivial to solve the control Riccati equations for a system as large as this, and the application of the circulant transformation has been beneficial in reducing the complexity of the computation. It has also been shown that the circulant transformation reduces the real-time computation required for implementing this controller by a factor of almost four over the standard implementation of a global controller. Finally, the Sensitivity transfer function singular values showed that the compensator designed using this approach yield good classical stability margins in gain and phase.

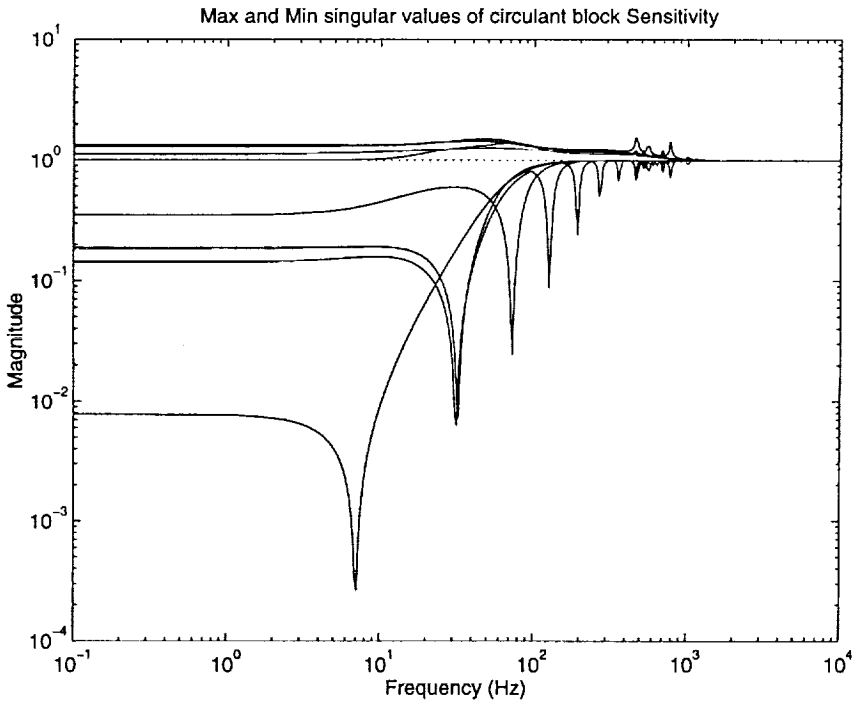

Figure 5-22: Maximum and minimum singular values of each circulant block of the sensitivity transfer function for the full scale global controller.

Chapter 6

Conclusions

6.1 Summary

Traditionally, adaptive optics systems use a small thin deformable mirror with piezoelectric or magnetostrictive actuators located at a tertiary or quaternary location in the optical train to compensate for atmospheric distortion. The Multiple Mirror Telescope (MMT) under development at the University of Arizona is taking a new approach to atmospheric compensation. To minimize emissivity effects for infrared astronomy the new approach seeks to place the deformable element at the secondary location in the optical train. Incoming light reflects from the primary mirror to the deformable secondary mirror, and is focussed on the science detector eliminating the need for additional bounces. A series of wavefront detectors provides a measure of the wavefront phase error which is corrected by the deformable secondary mirror.

This new approach has clear benefits in terms of the signal to noise ratio obtained when light is bounced from fewer emitting surfaces. However, it poses some technical challenges as well. Where deformable mirrors are usually small and actuated by stiff piezoelectric or magnetostrictive actuators, the proposed deformable mirror is necessarily large. The 6.5 m primary mirror for the MMT requires a 0.65 m secondary. Furthermore, the correction of global tilt at the secondary mirror requires relatively large displacements of the mirror. Electro-magnetic voice coil actuators are planned to provide the actuation necessary to deform the mirror. The combination of large mirror

size, and low stiffness force actuation result in a considerably more flexible mirror than usual. This extra flexibility results in a large number of flexible vibrational modes of the mirror within the bandwidth necessary to correct for atmospheric distortion across the large 6.5 m aperture.

Flexibility within the control bandwidth calls for a new approach to adaptive optics. In this thesis such an approach has been put forward. The traditional adaptive optics approach takes a set of wavefront slope measurements and reconstructs an estimated wavefront based on the statistics of an atmospheric model. Then the appropriate controls are applied to conjugate the wavefront by inverting the static influence matrix which accounts for the influence that each actuator has on the entire surface of the mirror. This process neglects the dynamic nature of the mirror, and is suitable only in the quasi-static frequency range of the mirror. Because the dynamic modes of the MMT adaptive secondary mirror are at much lower frequency than other deformable mirrors, the mirror is not quasi-static in the frequency range necessary to correct for the atmospheric distortion. Dynamic influence functions, the transfer function of an actuator to a position on the mirror, are required to conjugate the wavefront over a wider frequency range.

Dynamic influence functions are incorporated into a wavefront estimator utilizing a Kalman filter, which becomes in essence a Dynamic Reconstructor. The Kalman filter estimates not only the atmospheric states, but also the structural dynamic states of the mirror. Optimal control is then applied having an estimate of the atmospheric and structural states. In others words, a Linear Quadratic Gaussian (LQG) control problem results which requires accurate structural and disturbance models.

On the order of 300 actuators and sensors are used to improve the seeing of the mirror. The amount of real-time computation required to implement such a control system, and the magnitude of the models required to design such a control system make this a formidable control problem. Exploiting the circularly symmetric nature of the mirror, and a suitable model of atmospheric distortion, the control problem is divided into a number of smaller decoupled control problems. The control system is recognized as being circulant, and circulant matrix theory is applied to decouple the

control problem.

A method was then developed for creating dynamic models of circulant systems. For structural systems, characterized by mass and stiffness matrices, circular symmetry results in circulant mass and stiffness matrices. Circulant matrix theory can be applied to these to decouple the equations of motion of the structure. Recognizing that the decoupling provided by circulant matrices splits the dynamics of a structure into modal groups, a modal approach to placing a system in circulant form was developed. It was found to be unnecessary to apply circulant transformations to the mass and stiffness matrices. Rather, a modal solution from a finite element package could be obtained, and the mode shapes transformed to decouple the system dynamics into the same modal groups identified through circulant matrix theory.

With the dynamic systems decoupled, the optimal control problem to determine the dynamic reconstructor for the system decouples. Furthermore, because the dynamics are decoupled into modal groups, frequency uncertainty, common in structural systems, can be treated independently in each problem. The resulting controllers are themselves circulant, and the decoupled nature of the controller permits real-time computation savings when implementing the controller.

Finally, the process of dynamic reconstruction and multivariable control was compared to an alternative control approach. The alternative approach seeks as much commonality with the traditional approach as possible. The process of reconstruction is treated as though the mirror is quasi-static. A high bandwidth inner control loop is required to ensure that with this loop closed, the flexible mirror is in fact quasi-static. The dynamic reconstruction process was demonstrated to be superior to the alternative in that it achieves better performance with lower bandwidth, at the cost of about 30% more real-time computation for the full scale mirror.

6.2 Contributions

(i) A procedure was developed for incorporating the dynamic nature of force-actuated, thin facesheet deformable mirrors into the adaptive optics reconstruc-

tion process. The standard adaptive optics reconstruction process assumes that the deformable mirror can be treated as a quasi-static device. It incorporates the influence of the deformable mirror through a series of static influence functions. The new procedure combines dynamic influence functions with a linearized atmospheric distortion model in a multivariable control problem that can be interpreted as a dynamic reconstructor.

(ii) A procedure was developed for obtaining a decoupled model of a circulant structural system directly from a modal solution output from a finite element modelling package.

(iii) Using circulant matrix theory, the complexity for both calculation and implementation of control for circulant systems with unconstrained feedback paths has been reduced. Circulant matrix theory has been used to break up the large but circulant control problem into a number of smaller decoupled control problems. This decoupling of the control problems enables parallel computation of the optimal compensator, and allows parallel computation in real-time implementation of this compensator.

(iv) In Appendix A, preliminary design laws for thin facesheet adaptive optics conceptual design are presented. On the basis of dynamic parameters of both the deformable mirror and the atmospheric distortion, general guidelines on properties of the deformable mirror are given.

(v) A procedure for modelling temporally averaged sensors has been developed. The model results in modifications which are identical to those that occur when modelling a zero-order hold for sampled data systems. The time period over which the average is taken is equivalent to the sample period for the zero-order hold approximation. As such, the magnitude effects of the averaging affect the frequency range above the Nyquist frequency for the average, and are neglected. The model results in a time delay model for the averaging sensor that incorporates one-half average period delay as a sensor model.

6.3 Recommendations

(i) One drawback of using multivariable control is the "curse of dimensionality" [69]. With a very large number of actuators and sensors, the amount of real-time computation increases as the square of the number of actuators and sensors. Utilizing circulant matrix theory, the amount of real-time computation has been cut by a factor of about four for this problem. Restricting the feedback structure by a method such as that proposed by Mercadal [70] could result in large computational savings if the feedback could be restricted so that only a small number of sensors feeds back to any one actuator. Similarly the schemes proposed by Wall [22] and How and Hall [23] are possible.

(ii) As an extension to the previous recommendation, determining methods for calculating the "optimal" feedback structure would be very useful. Most approaches for restricting feedback are *ad hoc* and use principles such as nearest neighbor feedback. However, the circulant system transformations show that decoupling of the control problem can result from other feedback combinations. A rigorous method to trade-off computation for performance rather than picking the feedback architecture and making the best of a potentially poor architecture would be very useful.

(iii) Optimizing the degree of circulance N, for the system could result in reduced real-time computation requirements.

(iv) Real-time computation could be reduced if the degree of circulance of the system could be set to a power of two. In such cases, an FFT could be used to perform the transformation of input and output signals to the compensator. Transformation using an FFT is an $O(N \log N)$ process rather than the matrix transformation which is $O(N^2)$.

(v) A major drawback of the proposed dynamic reconstruction is the limitations of using a linearized atmospheric model. The atmospheric model could be extended to be nonlinear by utilizing an Extended Kalman Filter instead of

simply a Kalman filter in the atmospheric estimation. Developing an approach to enable an arbitrary reconstructor to be placed into the estimator would be very useful as it would allow other approaches to Reconstruction such as Neural Networks[5, 6, 4] to be utilized.

References

[1] Sandler, D. G., M. LLoyd-Hart, T. Martinez, P. Gray, R. Angel, T. Barrett, D. Bruns, and S. Stahl, "The 6.5m MMT Infrared Adaptive Optics System: Detailed Design and Progress Report," *Proc., Adaptive Optical Systems and Applications*, San Diego, CA, 1995, pp. 372–377. SPIE Vol. 2534.

[2] Shelton, C., Dec. 1996. Personal Communication.

[3] Huang, J., D. P. Looze, N. Denis, and D. A. Castañon, "Control Designs for an Adaptive Optics System," *Proc., IEEE Conf. on Dec. and Cont.*, New Orleans, LA, Dec. 1995, pp. 3753–3756.

[4] Lloyd-Hart, M. and P. McGuire, "Spatio-Temporal Prediction for Adaptive Optics Wavefront Reconstructors," in *Technical Digest Series- Optical Society of America 1995; VOL 23.*

[5] Angel, J. R. P., P. Wizinowich, M. Lloyd-Hart, and D. G. Sandler, "Adaptive Optics for Array Telescopes Using Neural-Network Techniques," *Nature*, 1990.

[6] Sandler, D. G., T. K. Barrett, D. A. Palmer, R. Q. Fugate, and W. J. Wild, "Use of a Neural Network to Control an Adaptive Optics System for an Astronomical Telescope," *Nature*, 1991.

[7] Gully, S. W., J. Huang, N. Denis, D. P. Looze, A. Wirth, A. J. Jankevics, and D. A. Castañon, "Experiments with Adaptive Nonlinear Control Systems for Atmospheric Correction," *Proc., SPIE Vol.2201 Adaptive Optics in Astronomy*, 1994, pp. 920—934.

[8] Ljung, L., "Asymptotic Behavior of the Extended Kalman Filter as a Parameter Estimator for Linear Systems," *IEEE Trans. on Automatic Control*, Vol. AC–24, No. 1, Feb. 1979, pp. 36–50.

[9] Ljung, L., *System Identification: Theory for the User*, Prentice–Hall, Inc., 1987.

[10] Biasi, R. and D. Gallieni, "Control Law Design for Electromagnetic Actuators at the Secondary Mirror," tech. rep., Dipartimento di Ingegneria Aerospaziale, Politecnico di Milano, 1995.

[11] Weinburg, L., *Network Analysis and Synthesis*, McGraw-Hill Book Company, Inc., New York, 1962.

[12] Tyson, R. K., *Principles of Adaptive Optics*, Academic Press, Inc., Boston, 1991.

[13] Sandler, D. G., L. Cuellar, M. Lefebvre, T. Barrett, R. Arnold, P. Johnson,

A. Tego, G. Smith, G. Taylor, and B. Spivey, "Shearing Interferometry for Laser-Guide-Star Atmospheric Correction at Large D/r_0," *Journal of the Optical Society of America, A*, Vol. 11, No. 7, February 1994, pp. 858–873.

[14] Fried, D. L., "Least-square Fitting a Wave-front Distortion Estimate to an Array of Phase-difference Measurements," *Journal of the Optical Society of America*, Vol. 67, No. 3, March 1977, pp. 370–375.

[15] Hudgin, R. H., "Wave-Front Reconstruction for Compensated Imaging," *Journal of the Optical Society of America*, Vol. 67, No. 3, March 1977, pp. 375–378.

[16] Southwell, W. H., "Wave-Front Estimation from Wave-Front Slope Measurements," *Journal of the Optical Society of America*, Vol. 70, No. 8, August 1980, pp. 998–1006.

[17] Hudgin, R. H., "Optimal Wave-Front Estimation," *Journal of the Optical Society of America*, Vol. 67, No. 3, March 1977, pp. 378–382.

[18] Hudgin, R. H., "Wave-Front Compensation Error Due to Finite Corrector-Element Size," *Journal of the Optical Society of America*, Vol. 67, No. 3, March 1977, pp. 393–395.

[19] Wallner, E. P., "Optimal Wave-front Correction Using Slope Measurements," *Journal of the Optical Society of America*, Vol. 73, No. 12, December 1983, pp. 1771–1776.

[20] Kwakernaak, H. and R. Sivan, *Linear Optimal Control Systems*, Wiley-Interscience, New York, 1972.

[21] Davis, P. J., *Circulant Matrices*, John Wiley and Sons, New York, 1979.

[22] Wall, Jr., J. E., *Control and Estimation for Large-Scale Systems Having Spatial Symmetry*, Ph.D. thesis, M.I.T., Cambridge, MA, Aug. 1978.

[23] How, J. P., *Local Control Design Methodologies for a Hierarchic Control Architecture*, Master's thesis, Department of Aeronautics and Astronautics, M.I.T., Cambridge, MA, Jan. 1990.

[24] Bathe, K.-J., *Finite Element Procedures in Engineering Analysis*, Prentice-Hall, Inc, Englewood Cliffs, NJ, 1982.

[25] Meirovitch, L., *Elements of Vibrational Analysis*, McGraw-Hill, Inc., New York, NY, 1986.

[26] Mills-Curran, W., "Calculation of Eigenvector Derivatives for Structures with Repeated Eigenvalues," *AIAA Journal*, Vol. 26, No. 7, July 1988, pp. 867–871.

[27] Franklin, G. F., J. D. Powell, and M. L. Workman, *Digital Control of Dynamic Systems, 2nd Edition*, Addison-Wesley Publishing Conpany, Inc., New York, 1990.

[28] Houpis, C. H. and G. B. Lamont, *Digital Control Systems - theory, hardware, software*, McGraw-Hill, New York, 1985.

[29] Smith, R. S. and P. Blixt, "The Stability Analysis of Sampled–Data Systems

with Averaging Samplers and Time Delays," *Proc.*, IFAC 13^{th} World Congress, San Francisco, CA, July 1996, pp. I203–208.

[30] Collins, S. A., D. W. Miller, and A. H. Von Flotow, "Distributed Sensors as Spatial Filters in Active Structural Control," *Journal of Sound and Vibration*, Vol. 173, No. 4, 1994, pp. 471–501.

[31] Andersson, M. S.-E., *Spatially Filtering Strain Sensors for Structural Shape Estimation fo Intelligent Structures*, Master's thesis, Massachusetts Institute of Technology, 1993.

[32] Salas, S. L., E. Hille, and J. T. Anderson, *Calculus: One and Several Variables, with Analytic Geometry*, John Wiley and Sons, Toronto, 1986.

[33] in *MSC/NASTRAN Quick Reference Guide - Version 68*, MacNeal-Schwendler Corporation, 1994.

[34] Roggemann, M. C., B. M. Welsh, D. Montera, and T. A. Rhoadarmer, "Method for Simulating Atmospheric Turbulence Phase Effects for Multiple Time Slices and Anisoplanatic Conditions," *Applied Optics*, Vol. 34, No. 20, 10 July 1995, pp. 4037–4051.

[35] Lloyd-Hart, M., 1996. Personal Communication.

[36] Greenwood, D. P., "Bandwidth Specification for Adaptive Optics Systems," *Journal of the Optical Society of America*, Vol. 67, No. 3, Mar. 1977, pp. 390–393.

[37] Noll, R. J., "Zernike Polynomials and Atmospheric turbulence," *Journal of the Optical Society of America*, Vol. 66, No. 3, Mar. 1976, pp. 207–211.

[38] Athans, M. and G. Stein, "Lecture notes for 6.232, Multivariable Control Systems," tech. rep., M.I.T., 1984.

[39] Guyan, R. J., "Reduction of Mass and Stiffness Matrices," *AIAA Journal*, Vol. 2, No. 1, Feb. 1965, p. 380.

[40] Meirovitch, L., *Computational Methods in Structural Dynamics*, Sijthoff and Noordhoff, Rockville, MA, 1980.

[41] Lehtomaki, N., *Practical Robustness Measures in Multivariable Control System Analysis*, Ph.D. thesis, MIT, May 1981.

[42] Safonov, M. G. and M. Athans, "Gain and Phase Margin for Multiloop LQG Regulators," *IEEE Trans. on Automatic Control*, Vol. AC–22, No. 2, Apr. 1977, pp. 173–179.

[43] Francis, B. A., *A Course in $\mathcal{H}_\infty$ Control Theory*, Springer-Verlag, 1987.

[44] Doyle, J. C., K. Glover, P. P. Khargonekar, and B. A. Francis, "State-Space Solutions to Standard $\mathcal{H}_2$ and $\mathcal{H}_\infty$ Control Problems," *IEEE Trans. on Automatic Control*, Vol. AC–34, No. 8, Aug. 1989, pp. 831–847.

[45] Maciejowski, J. M., *Multivariable Feedback Design*, Addison-Wesley, Wokingham, England, 1989.

[46] Meirovitch, L., H. Baruh, and H. Öz, "A Comparison of Control Techniques for

Large Flexible Systems," *AIAA J. of Guid., Cont., and Dyn.*, Vol. 6, No. 4, Aug. 1983, pp. 302–310.

[47] Öz, H. and L. Meirovitch, "Stochastic Independent Modal-Space Control of Distributed-Parameter Systems," *Journal of Optimization Theory and Applications*, Vol. 40, No. 1, May 1983, pp. 121–154.

[48] Meirovitch, L. and J. K. Bennighof, "Modal Control of Traveling Waves in Flexible Structures," *Journal of Sound and Vibration*, Vol. 111, No. 1, 1986, pp. 131–144.

[49] Campbell, M. E., S. C. O. Grocott, J. P. How, D. W. Miller, and E. F. Crawley, "Verification Procedure for On-orbit Controllers for the MIT Middeck Active Control Experiment," *Proc., American Cont. Conf.*, Seattle, WA, June 1995, pp. 3600–3605.

[50] Lehtomaki, N. A., N. R. Sandell, Jr, and M. Athans, "Robustness Results in Linear-Quadratic Gaussian Based Multivariable Control Designs," *IEEE Trans. on Automatic Control*, Vol. AC–26, No. 1, Feb. 1981, pp. 75–92.

[51] Miller, D. W., E. F. Crawley, J. P. How, K. Liu, M. E. Campbell, S. C. O. Grocott, R. M. Glaese, and T. D. Tuttle, "The Middeck Active Control Experiment (MACE) : Summary Report," Tech. Rep. SERC #7-96, Space Engineering Research Center, Massachusetts Institute of Technology, June 1996.

[52] Grocott, S. C. O., *Comparison of Control Techniques for Robust Performance on Uncertain Structural Systems*, Master's thesis, Massachusetts Institute of Technology, 1994. MIT SERC report # 2-94.

[53] How, J. P., *Robust Control Design with Real Parameter Uncertainty using Absolute Stability Theory*, Ph.D. thesis, Department of Aeronautics and Astronautics, M.I.T., Cambridge, MA, Jan. 1993.

[54] Smith, R. S., C.-C. Chu, and J. L. Fanson, "The Design of $\mathcal{H}_\infty$ Controllers for an Experimental Non-collocated Flexible Structure Problem," *IEEE Trans. on Control Systems Technology*, Vol. 2, No. 2, 1994, pp. 101–109.

[55] Balas, G. J. and J. C. Doyle, "Robustness and Performance Trade-Offs in control design for Flexible Structures," *IEEE Trans. on Control Systems Technology*, Vol. 2, No. 4, Dec. 1994, pp. 352–361.

[56] Balas, G. J. and P. M. Young, "Control Design for Variations in Structural Natural Ferquencies," *AIAA J. of Guid., Cont., and Dyn.*, Vol. 18, No. 2, Mar. 1995, pp. 325–332.

[57] Collins Jr., E. G., J. A. King, and D. J. P. an D. C. Hyland, "High Performance, Accelerometer–Based Control of the Mini–MAST Structure," *AIAA J. of Guid., Cont., and Dyn.*, Vol. 15, No. 4, July 1992, pp. 885–892.

[58] Collins Jr., E. G., L. D. Davis, and S. Richter, "A Homotopy Algorithm for Maximum Entropy Design," *Proc., American Cont. Conf.*, San Francisco, CA, 1993, pp. 1010–1014.

[59] Campbell, M. E., *Neo-Classical Control of Structures*, Master's thesis, Department of Aeronautics and Astronautics, M.I.T., Cambridge, MA, Feb. 1993.

[60] Wie, B., L. Horta, and J. Sulla, "Active Structural Control Design and Experiment for the Mini–Mast," *Proc., American Cont. Conf.*, San Diego, CA, May 1990, pp. 1428–1434.

[61] Okada, K. and R. E. Skelton, "Sensitivity Controller for Uncertain Systems," *AIAA J. of Guid., Cont., and Dyn.*, Vol. 13, No. 2, 1990, pp. 321–329.

[62] Tahk, M. and J. L. Speyer, "Parameter Robust Linear-Quadratic-Gaussian Design Synthesis with Flexible Structure Control Applications," *AIAA J. of Guid., Cont., and Dyn.*, Vol. 12, No. 4, Aug. 1989, pp. 460–468.

[63] Grocott, S. C. O., J. P. How, and D. W. Miller, "An Experimental Comparison of Robust $\mathcal{H}_2$ Control Techniques for Uncertain Structural Systems," *AIAA J. of Guid., Cont., and Dyn.*, Vol. 20, No. 3, May 1997.

[64] Hyland, D. C., "Maximum Entropy Stochastic Approach to Controller Design for Uncertain Structural Systems," *Proc., American Cont. Conf.*, Arlington, VA, June 1982, pp. 680–688.

[65] Bernstein, D. S. and W. M. Haddad, "LQG Control with an $\mathcal{H}_\infty$ Performance Bound: A Riccati Equation Approach," *IEEE Trans. on Automatic Control*, Vol. AC–34, No. 3, Mar. 1989, pp. 293–305.

[66] Ashkenazi, A. and A. E. Bryson Jr., "Control Logic for Parameter Insensitivity and Disturbance Attenuation," *AIAA J. of Guid., Cont., and Dyn.*, Vol. 5, No. 4, July 1982, pp. 383–388.

[67] MacMartin, D. G., S. R. Hall, and D. S. Bernstein, "Fixed Order Multi-Model Estimation and Control," *Proc., American Cont. Conf.*, Boston, MA, June 1991, pp. 2113–2118.

[68] Zhou, K., J. C. Doyle, and K. Glover, *Robust and Optimal Control*, Prentice-Hall, Inc., 1996.

[69] Kirk, D. E., *Optimal Control Theory: An Introduction*, Prentice-Hall Inc., Englewood Cliffs, NJ, 1970.

[70] Mercadal, M., *$\mathcal{H}_2$, Fixed Architecture, Control Design for Large Scale Systems*, Ph.D. thesis, Department of Aeronautics and Astronautics, M.I.T., Cambridge, MA, June 1990.

Appendix A

Wavenumber - Frequency Relationships

For both the dynamics of the deformable mirror, and the dynamics of atmospheric turbulence, there is a relationship between the temporal frequency (ω) and the spatial wavenumber (κ) and its associated wavelength.

For the mirror, which is modelled as a plate, the structural dispersion relationship is quadratic.

$$\omega = \kappa^2 \sqrt{\frac{Et^2}{12\rho(1-\nu^2)}}, \tag{A.1}$$

where E is the modulus of elasticity, t is the thickness of the mirror, ρ is the density of the material, and ν is Poisson's ratio for the mirror material.

It was seen in Chapter 4 that atmospheric distortion is often modelled using the 'frozen flow' hypothesis. This hypothesis states that over the relevant period of time, changes in the turbulent eddies in the atmosphere are negligible relative to the translation of the turbulent eddies traveling across the aperture of a telescope. In this case, the atmospheric distortion is fundamentally non-dispersive. No matter what wavenumber (wavelength) of distortion the atmospheric distortion has, the shape of the distortion remains unchanged as it travels. Therefore the relationship between frequency and wavenumber for the atmospheric distortion is simply

$$\omega = v_w \kappa \tag{A.2}$$

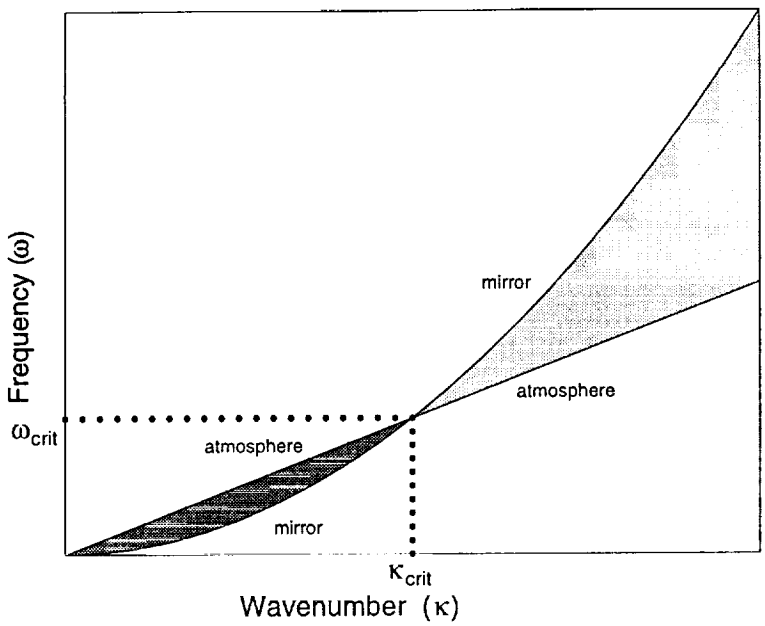

Figure A-1: Wavenumber-frequency relationship for mirror structure and atmospheric distortion.

where v_w is the velocity of the wind.

At different temporal frequencies, the structure and atmosphere support different wavelengths of motion. Figure A-1 shows the two wavenumber-frequency relationships plotted as a function of wavenumber. At low temporal frequency, atmospheric distortion has a longer wavelength than is naturally supported by the mirror. Thus the control must fight the inertia of the mirror in order to follow the correct shape. At high temporal frequency, atmospheric distortion wavelengths are shorter than those supported by the mirror. Here the control must fight stiffness. At ω_{crit}, the control fights only the damping.

The density of actuators determines in which region the control lies. For systems in which the number of actuators places the system in the region above ω_{crit}, more Zernike modes of the distortion are important than structural dynamic modes. This means that the system is one that requires actuators to follow the Zernike modes, not necessarily to control the structural dynamics. Below ω_{crit}, the structural dynamics dominate. Modes of the system may result with wavelengths less than inter-actuator spacing. Clearly, the desirable region is the stiffness dominated region in which the

actuators are required for Zernike mode tracking. Otherwise, the flexibility will result in significant dynamic wavefront error which cannot be tracked.

The critical wavenumber can be determined by equating Equations A.1 and A.2. Then

$$\kappa_{crit} = v_w \sqrt{\frac{12\rho(1-\nu^2)}{Et^2}}. \tag{A.3}$$

For the MMT adaptive secondary mirror, $v_w = 15$ m/s, $E = 70 \times 10^9$ N/m^2, $t = 0.00225$ m, $\rho = 2100$ kg/m^3, and $\nu = 0.22$. This yields $\kappa_{crit} = 3.90$ m^{-1}. For this system the inter-actuator spacing is roughly 0.03 m which gives the system an actuator based wavenumber of 15 m^{-1} (assuming two actuators per wavelength), well above the critical wavenumber. Thus this system is characterized as stiffness dominated. Equation A.3 provides guidelines by which the properties of the mirror can be tailored to make sure that the dynamics are in the correct region.